3-31-2017

Tunable, Room Temperature THz Emitters Based on Nonlinear Photonics

Raju Sinha
Florida International University, rsinh001@fiu.edu

FLORIDA INTERNATIONAL UNIVERSITY

Miami, Florida

TUNABLE, ROOM TEMPERATURE THZ EMITTERS BASED ON

NONLINEAR PHOTONICS

A dissertation submitted in partial fulfillment of

the requirements for the degree of

DOCTOR OF PHILOSOPHY

in

ELECTRICAL ENGINEERING

by

Raju Sinha

2017

To: Interim Dean Ranu Jung
    College of Engineering and Computing

This dissertation, written by Raju Sinha, and entitled Tunable, Room Temperature THz Emitters Based on Nonlinear Photonics, having been approved in respect to style and intellectual content, is referred to you for judgment.

We have read this dissertation and recommend that it be approved.

_____
Sakhrat Khizroev

_____
Irene Calizo

_____
Jessica Ramella-Roman

_____
Nezih Pala, Major Professor

Date of Defense: March 31, 2017

The dissertation of Raju Sinha is approved.

_____
Interim Dean Ranu Jung
College of Engineering and Computing

_____
Andrés G. Gil
Vice President for Research and Economic Development
and Dean of the University Graduate School

Florida International University, 2017

ii

DEDICATION

I dedicate this dissertation to my loving parents, brother and sister-in-law. Without their

love, support, and patience, it would have been impossible to complete this research.

ACKNOWLEDGMENTS

ABSTRACT OF THE DISSERTATION

TUNABLE, ROOM TEMPERATURE THZ EMITTERS BASED ON NONLINEAR

PHOTONICS

by

Raju Sinha

Florida International University, 2017

Miami, Florida

Professor Nezih Pala, Major Professor

The Terahertz (10^{12} Hz) region of the electromagnetic spectrum covers the frequency range from roughly 300 GHz to 10 THz, which is in between the microwave and infrared regimes. The increasing interest in the development of ultra-compact, tunable room temperature Terahertz (THz) emitters with wide-range tunability has stimulated in-depth studies of different mechanisms of THz generation in the past decade due to its various potential applications such as biomedical diagnosis, security screening, chemical identification, life sciences and very high speed wireless communication. Despite the tremendous research and development efforts, all the available state-of-the-art THz emitters suffer from either being large, complex and costly, or operating at low temperatures, lacking tunability, having a very short spectral range and a low output power. Hence, the major objective of this research was to develop simple, inexpensive, compact, room temperature THz sources with wide-range tunability.

We investigated THz radiation in a hybrid optical and THz micro-ring resonators system. For the first time, we were able to satisfy the DFG phase matching condition for

the above-mentioned THz range in one single device geometry by employing a modal phase matching technique and using two separately designed resonators capable of oscillating at input optical waves and generated THz waves. In chapter 6, we proposed a novel plasmonic antenna geometry – the dimer rod-tapered antenna (DRTA), where we created a hot-spot in the nanogap between the dimer arms with a very large intensity enhancement of 4.1×10^5 at optical resonant wavelength. Then, we investigated DFG operation in the antenna geometry by incorporating a nonlinear nanodot in the hot-spot of the antenna and achieved continuously tunable enhanced THz radiation across 0.5-10 THz range. In chapter 8, we designed a multi-metallic resonators providing an ultrasharp toroidal response at THz frequency, then fabricated and experimentally demonstrated an efficient polarization dependent plasmonic toroid switch operating at THz frequency.

In summary, we have successfully designed, analytically and numerically investigated novel THz emitters with the advantages of wide range tunability, compactness, room temperature operation, fast modulation and the possibility for monolithic integration, which are the most sought after properties in the new generation THz sources.

TABLE OF CONTENTS

LIST OF FIGURES

LIST OF ACRONYMS & ABBREVIATIONS

THz	Terahertz
DFG	Difference frequency generation
NLO	Nonlinear optical material
SHG	Second harmonic generation
SFG	Sum frequency generation
AlN	Aluminum nitride
CMOS	Complementary metal-oxide-semiconductor
2D	Two dimensional
3D	Three dimensional
XRD	X-ray diffraction
DI	De-ionized
TE	Transverse electric
TM	Transverse magnetic
RIE	Reactive ion etching
DRIE	Deep reactive ion etching
SiO_2	Silicon dioxide
CW	Continuous wave
GHz	Gigahertz
HEMT	High electron mobility transistor
BWO	Backward wave oscillator
MSM	Metal-semiconductor-metal
$LiNbO_3$	Lithium Niobate
$KNbO_3$	Potassium Niobate
KTP	Potassium titanyl phosphate

MgO	Magnesium oxide
QCL	Quantum cascade laser
OR	Optical rectification
FSR	Free spectral range
FWHM	Full width half maximum
PECVD	Plasma-enhanced chemical vapor deposition
HR	High resistivity
EBL	Electron beam lithography
PML	Perfectly matched layer
FDTD	Finite difference time domain
FEM	Finite element method
$BaTiO_3$	Barium titanate
TMAH	Tetramethylammonium hydroxide
ICP	Inductively coupled plasma

CHAPTER 1

Introduction

1.1   Motivation

The Terahertz (10^{12} Hz) region of the electromagnetic spectrum covers the frequency range from roughly 300 GHz to 10 THz, which is in between the microwave and infrared regimes. Due to its unique properties, potential applications of terahertz (THz) technology in security screening, chemical identifications, biomedical diagnostics, life sciences, sensing, quality control of semiconductor devices, space research and tactical imaging are becoming a reality [1-7]. THz radiation can penetrate non-metallic materials such as paper, plastic, fabric and leather, which makes it useful for security monitoring applications. This property also allows us to detect sketches underlying paintings, track hidden defects inside a material and to see murals hidden underneath coats of plaster in historic buildings without affecting the artifacts. Unlike the x-ray and ultraviolet spectrum, THz radiation does not pose any ionization hazard to biological tissues, which makes it attractive for biological and medical applications. Since energy of the THz frequencies coincide with the energy levels of molecular rotations and vibrations of DNA, proteins and even chemical explosives, THz spectrum provides characteristic unique fingerprints, which allows us to differentiate between biological tissues and identify different explosives as well. In addition, the THz spectrum can be utilized to indicate tissue conditions by checking hydration level. One significant impediment in realizing these applications is the cost and complexity associated with THz sources. Hence, developing a room temperature THz emitter with wide-range tunability, compactness and simple alignment is inevitable.

The increasing interest in the development of novel THz sources has stimulated in-depth studies of microscopic mechanisms of THz field generation in conventional semiconductors, electro-optic materials, and an extensive search for new materials and devices to be employed in THz generation and detection. Table 1.1 summarizes the state-of-the-art THz emitters for different spectral ranges of operation, THz output powers, physical sizes, operating temperatures and tunability. Although the free electron laser covers moderate tuning range with high output power, it is not only too expensive and bulky but also complex to be employed. Again, solid-state electronic laser like gun diode provides moderate output power but comes with poor tuning range. Comparatively, quantum cascade laser (QCL) is compact and provides mW level output power with moderate tuning range but operates below room temperature. Although recently room temperature QCL is demonstrated, higher power with wide tuning range employing that approach has yet to be demonstrated [8]. Despite the tremendous research and development efforts, all the available state-of-the-art THz emitters suffer from either being large, complex and costly, or operating at low temperatures, lacking tunability, having a very short spectral range and a low output power. Hence, developing a simple, tunable, compact THz source operating at room temperature is still a challenging task.

Among all the major approaches of designing the THz emitters, the use of optical methods has been the most popular technique for generating the THz radiation. They include photoconductive antenna, optical parametric oscillation, optical rectification and difference frequency generation (DFG) [9-12]. However, optical to THz conversion through the DFG process using second order nonlinear material ($\chi^{(2)}$) suffers from low

conversion efficiencies due to the Manly-Rowe quantum limit [13-15]. So far, THz wave generation through DFG phenomenon is designed and realized mostly in nonlinear bulk materials, which provide very low output power [16]. In order to achieve efficient and enhanced THz generation, DFG is employed recently in different potential resonant structures e.g. rib waveguide, dielectric strip embedded within metallic slot waveguide, photonic crystal waveguide, waveguides with nonlinear polymer cladding, triply resonant photonic resonators, silicon slot embedded ridge waveguide [17-20]. However, none of the THz emitters has tunability over the whole 0.5-10 THz range of interest, rather they are designed to achieve efficient generation either at a single THz frequency or across a short spectral range due to the difficulty of satisfying DFG phase matching condition for the large wavelength range of 600-30 μm (0.5-10 THz) in one single device geometry.

Table 1.1 | State-of-the-art THz Emitters. Different state-of-the-art THz emitters are summarized in terms of spectral range, power, size, working temperature and tunability option.

THz Emitters	Range (THz)	Power (W)	Size	Temp.	Tunability
Free Electron Lasers	0.12-4.75	5k-15k	Bulky	R.T.	Tunable
Backward Wave Oscillator	0.3-1.3	1m-50m	Table Top	R.T.	Tunable
Quantum Cascade Laser [21-24]	1.2-5	0.1m-100m	Small	< 169 K	Tunable
Quantum Cascade Laser [8, 25]	1-4.6	5μ- 32μ	Small	R.T.	Tunable
Gas Laser	0.9-3	1m- 30m	Table Top	R.T.	Discrete lines
Resonant Tunneling Diodes	0.1-1	0.1μ-100μ	Medium	R.T.	Not tunable
Gunn Diode Devices	0.01-0.2	0.1m-1	Medium	R.T.	Tunable

In this dissertation, we have proposed a novel approach employing the DFG process in order to achieve efficient and enhanced THz generation in the 0.5-10 THz range with

tunability resolution of 0.05 THz in one single device geometry [26, 27]. The proposed approach makes use of an optical microring resonator with a high value of second order nonlinearity ($\chi^{(2)}$) in order to facilitate the DFG via nonlinear mixing with the choice of two appropriate input infrared optical waves. Enhanced THz generation is ensured by designing the optical resonator in such a way that both the input optical waves get resonated inside the ring. Efficient coupling of infrared waves from bus to the nonlinear resonator is ensured by satisfying the critical coupling condition. Moreover, the challenge of satisfying DFG phase matching condition across the THz range in one single device geometry has been overcome by employing the modal phase matching technique with the design of another microring resonator solely dedicated to sustain the generated THz waves. High resistivity (HR) Si is chosen to guide THz radiation due to its transparency in much of the THz range and high refractive index, which facilitates to concentrate THz waves in much smaller sizes than that of ordinary optical fibers.

In comparison to microring resonators, microdisk resonators with the same dimensions provide higher quality factors with smaller radiation losses due to the absence of inner cylindrical boundaries. In other words, the supported modes exhibit stronger confinement by featuring weaker penetration to the surrounding air and being closer to the resonator center. Moreover, the surface roughness scattering losses are also reduced due to the absence of inner cylindrical boundary. Therefore, we have proposed another THz emitter with the same spectral range and tunability resolution using individual microdisk resonators for both the input optical waves and generated THz waves [28, 29]. Both the THz emitters are investigated in detail with analytical model and numerical simulation

results. They are Silicon on Insulator (SoI) technology compatible enabling the monolithic integration with Si CMOS electronics including plasmonic THz detectors.

Plasmonic nanostructures have the unique ability to strongly localize and enhance electromagnetic fields in nanoscale volumes by enabling resonant coupling of electromagnetic waves to the oscillations of a metal's conduction band electrons, which is commonly known as surface plasmons [30-37]. These excitations provide strong confinement of electromagnetic energy far beyond the diffraction limit [38-44]. It is possible to enhance inherently weak nonlinear DFG process by employing the extremely large localized electric fields produced by surface plasmons [39]. In this dissertation, we have further proposed, designed and investigated in detail Au-AlN-SiO$_2$ core shell nanostructures, AlN nanodot coupled with plasmonic nanogap antenna and AlN thin film coupled plasmonic grating resonators to achieve plasmonic resonance enhanced DFG across 0.5-10 THz range with continuous tunability. Then we proposed a novel plasmonic antenna type geometry – the dimer rod-tapered antenna (DRTA) with a huge field intensity enhancement in the nanogap between the dimer arms and exploited the hot-spot for tunable DFG THz generation across the desired interest. We further explored another potential plasmonic nanostructure consisting of nonlinear film coupled Aluminum grating resonators to achieve enhanced DFG THz radiation with continuous tunability across the 0.5-10 THz range. The beauty of these proposed plasmonic device structures lies in the fact that the small dimensions of the nanostructures with respect to the spatial extents of the input optical waves and the output THz waves, makes the required DFG phase matching conditions irrelevant [45, 46]. We believe, the proposed THz emitters in this dissertation,

will open new avenues to demonstrate efficient, promising, inexpensive and on-chip integrated THz structures for all-optical and optoelectronic devices.

In addition, we have designed and fabricated a multi-metallic plasmonic micro-structure and experimentally demonstrated a polarization angle dependent THz switch. We expect that the strong and ultra-sharp toroidal resonance of the studied plasmonic structure will make it a reliable platform for various applications including THz spectroscopy, biochemical sensing, medical and security imaging.

1.2   Aim and Scope of this Dissertation

The major objective of this dissertation is to develop tunable, compact, room temperature, efficient and enhanced THz emitters across the whole 0.5-10 THz range. Chapter 2 provides a literature review of different THz generation approaches and the theory of nonlinear optics including difference frequency generation (DFG) phenomenon in nonlinear media.

Chapter 3 describes a novel approach employing the DFG process in micro-ring resonators in order to achieve efficient and enhanced THz generation in the 0.5-10 THz range with tunability resolution of 0.05 THz. The proposed emitter was analytically and numerically investigated with detailed design steps for phase matching condition. Chapter 4 describes another potential THz emitter based on micro-disk resonators with detail analytical and numerical simulations. Spherical nonlinear plasmonic core-shell structures were investigated in detail for tunable DFG THz generation across the same range in chapter 5. Chapter 6 proposes a novel plasmonic antenna geometry, the dimer rod-tapered antenna (DRTA) and describes tunable DFG THz radiation by incorporating nonlinear

nanodot in the hot-spot between the dimer arms of the antenna. Chapter 7 provides another potential plasmonic structure with nonlinear optical material (NLO) film layer coupled Al based grating resonators with numerical simulations for tunable DFG in the above-mentioned THz range. Chapter 8 details experimental demonstration of a polarization angle dependent switch operation at THz frequency in a micro-fabricated multi-metallic structure showing extremely sharp toroidal resonance.

In chapter 9, we summarize the contribution of this dissertation and propose lab-on-a-chip THz spectrometer for point-of-care bio-sensing applications.

1.3   References

1. Tonouchi, M. (2007). Cutting-edge terahertz technology. Nature photonics, 1(2), 97-105.

2. Chen, H. T., Padilla, W. J., Zide, J. M., Gossard, A. C., Taylor, A. J., & Averitt, R. D. (2006). Active terahertz metamaterial devices. Nature, 444(7119), 597-600.

3. Mueller, E. R. (2006). Terahertz Radiation Sources for Imaging and Sensing Applications-New techniques are being used to generate emissions at terahertz frequencies. Photonics Spectra, 40(11), 60-69.

4. Hoheisel, M. (2006). Review of medical imaging with emphasis on X-ray detectors. Nuclear Instruments and Methods in Physics Research Section A: Accelerators, Spectrometers, Detectors and Associated Equipment, 563(1), 215-224.

5. Woolard, D. L., Brown, R., Pepper, M., & Kemp, M. (2005). Terahertz frequency sensing and imaging: A time of reckoning future applications?. Proceedings of the IEEE, 93(10), 1722-1743.

6. Quema, A. V., Goto, M., Sakai, M., Ouenzerfi, R. E., Takahashi, H., Murakami, H., Ono, S., Sarukura, N., & Janairo, G. (2004). Onset detection of solid-state phase transition in estrogen-like chemical via terahertz transmission spectroscopy. Applied physics letters, 85(17), 3914-3916.

7. Linden, K. J., Neal, W. R., Waldman, J., Gatesman, A. J., & Danylov, A. (December, 2005). Terahertz laser based standoff imaging system. In Applied Imagery and Pattern Recognition Workshop, 2005. Proceedings. 34th (pp. 8-pp). IEEE.

8. Lu, Q. Y., Bandyopadhyay, N., Slivken, S., Bai, Y., & Razeghi, M. (2013). Room temperature terahertz quantum cascade laser sources with 215 µW output power through epilayer-down mounting. Applied physics letters, 103(1), 011101.

9. Park, S. G., Weiner, A. M., Melloch, M. R., Sider, C. W., Sider, J. L., & Taylor, A. J. (1999). High-power narrow-band terahertz generation using large-aperture photoconductors. IEEE journal of quantum electronics, 35(8), 1257-1268.

10. Kawase, K., Hatanaka, T., Takahashi, H., Nakamura, K., Taniuchi, T., & Ito, H. (2000). Tunable terahertz-wave generation from DAST crystal by dual signal-wave parametric oscillation of periodically poled lithium niobate. Optics Letters, 25(23), 1714-1716.

11. Ahn, J., Efimov, A. V., Averitt, R. D., & Taylor, A. J. (2003). Terahertz waveform synthesis via optical rectification of shaped ultrafast laser pulses. Optics Express, 11(20), 2486-2496.

12. Sasaki, Y., Yuri, A., Kawase, K., & Ito, H. (2002). Terahertz-wave surface-emitted difference frequency generation in slant-stripe-type periodically poled $LiNbO_3$ crystal. Applied Physics Letters, 81(18), 3323-3325.

13. Lee, Y. S. (2009). Principles of terahertz science and technology (Vol. 170). Springer Science & Business Media.

14. Suhara, T., & Fujimura, M. (2013). Waveguide nonlinear-optic devices (Vol. 11). Springer Science & Business Media.

15. Waldmueller, I., Wanke, M. C., & Chow, W. W. (2007). Circumventing the Manley-Rowe quantum efficiency limit in an optically pumped terahertz quantum-cascade amplifier. Physical review letters, 99(11), 117401.

16. Majkić, A., Zgonik, M., Petelin, A., Jazbinšek, M., Ruiz, B., Medrano, C., & Günter, P. (2014). Terahertz source at 9.4 THz based on a dual-wavelength infrared laser and quasi-phase matching in organic crystals OH1. Applied Physics Letters, 105(14), 141115.

17. Saito, K., Tanabe, T., Oyama, Y., Suto, K., & Nishizawa, J. I. (2009). Terahertz-wave generation by GaP rib waveguides via collinear phase-matched difference-frequency mixing of near-infrared lasers. Journal of Applied Physics, 105(6), 063102.

18. Chen, T., Sun, J., Li, L., & Tang, J. (2012). Proposal for efficient terahertz-wave difference frequency generation in an AlGaAs photonic crystal waveguide. Journal of Lightwave Technology, 30(13), 2156-2162.

19. Baehr-Jones, T., Hochberg, M., Soref, R., & Scherer, A. (2008). Design of a tunable, room temperature, continuous-wave terahertz source and detector using silicon waveguides. JOSA B, 25(2), 261-268.

20. Bravo-Abad, J., Rodriguez, A. W., Joannopoulos, J. D., Rakich, P. T., Johnson, S. G., & Soljačić, M. (2010). Efficient low-power terahertz generation via on-chip triply-resonant nonlinear frequency mixing. Applied Physics Letters, 96(10), 101110.

21. Williams, B. S. (2007). Terahertz quantum-cascade lasers. Nature photonics, 1(9), 517-525.

22. Mottaghizadeh, A., Gacemi, D., Laffaille, P., Li, H., Amanti, M., Sirtori, C., Santarelli, G., Hänsel, W., Holzwart, R., Li, L.H., & Linfield, E.H. (2017). 5-ps-long terahertz pulses from an active-mode-locked quantum cascade laser. Optica, 4(1), 168-171.

23. Kundu, I., Dean, P., Valavanis, A., Chen, L., Li, L., Cunningham, J.E., Linfield, E.H., & Davies, A.G. (2017). Quasi-continuous frequency tunable terahertz quantum cascade lasers with coupled cavity and integrated photonic lattice. Optics Express, 25(1), 486-496.

24. Xu, L., Curwen, C., Chen, D., Reno, J., Itoh, T., & Williams, B. (2017). Terahertz metasurface quantum-cascade VECSELs: theory and performance. IEEE Journal of Selected Topics in Quantum Electronics.

25. Jung, S., Kim, J.H., Jiang, Y., Vijayraghavan, K., & Belkin, M.A. (2017). Terahertz difference-frequency quantum cascade laser sources on silicon. Optica, 4(1), 38-43.

26. Sinha, R., Karabiyik, M., Al-Amin, C., Vabbina, P.K., Güney, D.Ö., & Pala, N. (2015). Tunable Room Temperature THz Sources Based on Nonlinear Mixing in a Hybrid Optical and THz Micro-Ring Resonator. Scientific Reports, 5, 9422.

27. Sinha, R., Karabiyik, M., Al-Amin, C., Vabbina, P.K., & Pala, N. (2014, March). Nonlinear optical resonators for tunable THz emission. In SPIE OPTO (pp. 898505-898505). International Society for Optics and Photonics.

28. Sinha, R., Karabiyik, M., Al-Amin, C., Vabbina, P.K., Shur, M., & Pala, N. (2014, May). Microdisk resonators for difference frequency generation in THz range. In SPIE Sensing Technology+ Applications (pp. 910208-910208). International Society for Optics and Photonics.

29. Sinha, R., Karabiyik, M., Ahmadivand, A., Al-Amin, C., Vabbina, P.K., Shur, M., & Pala, N. (2016). Tunable, Room Temperature CMOS-Compatible THz Emitters Based on Nonlinear Mixing in Microdisk Resonators. Journal of Infrared, Millimeter, and Terahertz Waves, 37(3), 230-242.

30. Maier, S. A. (2007). Plasmonics: fundamentals and applications. Springer Science & Business Media.

31. Ahmadivand, A., Sinha, R., Vabbina, P.K., Karabiyik, M., Kaya, S., & Pala, N. (2016). Hot electron generation by aluminum oligomers in plasmonic ultraviolet photodetectors. Optics express, 24(12), 13665-13678.

32. Ahmadivand, A., Gerislioglu, B., Sinha, R., Karabiyik, M., & Pala, N. (2017). Optical Switching Using Transition from Dipolar to Charge Transfer Plasmon Modes in Ge2Sb2Te5 Bridged Metallodielectric Dimers. Scientific reports, 7, 42807.

33. Ahmadivand, A., Sinha, R., Karabiyik, M., Kaya, S., & Pala, N. (2016, May). Fractal aluminum Cayley-trees to design plasmonic ultraviolet photodetectors. In SPIE Defense+ Security (pp. 98362Y-98362Y). International Society for Optics and Photonics.

34. Ahmadivand, A., Sinha, R., Kaya, S., & Pala, N. (2016). A molecular plasmonic Fano-router: Using hotspots in a single-stone ring-like structure. Optics Communications, 367, 123-129.

35. Ahmadivand, A., Sinha, R., & Pala, N. (2015). Hybridized plasmon resonant modes in molecular metallodielectric quad-triangles nanoantenna. Optics Communications, 355, 103-108.

36. Ahmadivand, A., & Pala, N. (2015). Plasmon resonance hybridization in self-assembled copper nanoparticle clusters: Efficient and precise localization of surface plasmon resonance (LSPR) sensing based on Fano resonances. Applied spectroscopy, 69(2), 277-286.

37. Ahmadivand, A., Sinha, R., Karabiyik, M., Vabbina, P.K., Gerislioglu, B., Kaya, S., & Pala, N. (2017). Tunable THz wave absorption by graphene-assisted plasmonic metasurfaces based on metallic split ring resonators. Journal of Nanoparticle Research, 19(1), 3.

38. Alvarez-Puebla, R., Liz-Marzán, L. M., & García de Abajo, F. J. (2010). Light concentration at the nanometer scale. The Journal of Physical Chemistry Letters, 1(16), 2428-2434.

39. Gramotnev, D. K., & Bozhevolnyi, S. I. (2010). Plasmonics beyond the diffraction limit. Nature photonics, 4(2), 83-91.

40. Ahmadivand, A., Sinha, R., & Pala, N. (2016). Resonance coupling in plasmonic nanomatryoshka homo-and heterodimers. AIP Advances, 6(6), 065102.

41. Ahmadivand, A., Sinha, R., Kaya, S., & Pala, N. (2016). Rhodium plasmonics for deep-ultraviolet bio-chemical sensing. Plasmonics, 11(3), 839-849.

42. Ahmadivand, A., Pala, N., & Güney, D.Ö. (2015). Enhancement of photothermal heat generation by metallodielectric nanoplasmonic clusters. Optics express, 23(11), A682-A691.

43. Ahmadivand, A., Sinha, R., Gerislioglu, B., Karabiyik, M., Pala, N., & Shur, M. (2016). Transition from capacitive coupling to direct charge transfer in asymmetric terahertz plasmonic assemblies. Optics Letters, 41(22), pp.5333-5336.

44. Ahmadivand, A., Sinha, R., & Pala, N. (2015, August). Graphene plasmonics: multiple sharp Fano resonances in silver split concentric nanoring/disk resonator dimers on a metasurface. In SPIE Nanoscience+ Engineering (pp. 954713-954713). International Society for Optics and Photonics.

45. Kauranen, M., & Zayats, A. V. (2012). Nonlinear plasmonics. Nature Photonics, 6(11), 737-748.

46. Zhang, Y., Manjavacas, A., Hogan, N. J., Zhou, L., Ayala-Orozco, C., Dong, L., Day, J.K., Nordlander, P., & Halas, N. J. (2016). Toward surface plasmon-enhanced optical parametric amplification (SPOPA) with engineered nanoparticles: a nanoscale tunable infrared source. Nano letters, 16(5), 3373-3378.

CHAPTER 2

Background and State of the Art

2.1   Review of THz Generation Approaches

Presently, there is no single electronic device able to oscillate in the bandwidth 0.5–10 THz. Only resonant tunneling diodes were able to oscillate around 700 GHz; other microwave and millimeter wave active devices, such as Gunn diodes or Impatt diodes, being not able to exceed oscillating frequencies beyond 400–500 GHz [1]. InP Gunn oscillators are able to generate 30 mW at 193 GHz; 3 mW at 300 GHz and more than 1 mW at 315 GHz; while a GaAs tunnel injection transit time diode produces 10 mW at 202 GHz [2]. Therefore, multiplication circuits are used to generate THz frequencies. A multiplier consists of a nonlinear electronic device, such as a Schottky varactor diode placed between an input and an output-matching network. Unfortunately, the output power is much lower than that of the input, which is a serious drawback for the THz frequency range. An input with a power of 200–300 mW at 100 GHz can be produced by HEMT amplifiers, but a multiplier with a high-order of multiplication from 100 GHz up to 1–3 THz is not feasible due to the very high losses.

Traditionally, gas lasers generate continuous wave (CW) THz signals in the frequency domain 0.9–3 THz with output powers in the range of 1–30 mW: A gas laser consists of a carbon dioxide laser that pumps a cavity filled with a gas such as CH_4; N_2; etc., which dictates the lasing frequency. The gas sources show no tunability and are very large, with dimensions exceeding 2-5 m. Free-electron lasers generate either CW or pulsed

high power THz radiation, but they are very costly and have very large dimensions, functioning in large rooms containing many additional facilities. Therefore, only a few are operating in the world. However, backward wave oscillators (BWO) are based on the same principles as an electron laser and are able to deliver a few mW in the range of 0.6–1.3 THz. In contrast with THz gas lasers, BWO are frequency tunable (for example, between 0.78 and 0.97 THz or 1 and 1.25 THz) with a high sweeping rate. BWO requires a water cooling system and high bias voltages of 1–6 kV at 25–45 mA. The weight of a BWO (without the cooling system and the power supplies) is more than 15 kg. However, THz gas lasers and BWOs are commercially available, being the only CW THz sources that can be bought from the market. They are both bulky and need a lot of accessories such as high power supplies, water-cooling systems [3].

Heterodyne mixing (photomixing) of two individual optical CW lasers (one of them being tunable) in a photoconductor produces a photocurrent with a frequency equal to the difference between the frequencies of the two lasers. When this difference frequency is within the THz range of frequencies the photocurrent is propagated along the transmission line or is radiated in free-space with the help of an antenna. There are two types of photomixers: discrete-element photomixers and distributed photomixers. Discrete-element photomixers are photoconductors, such as micrometric photoconductive gaps or MSM interdigitated structures, with a large bias field applied between their electrodes, illuminated by the two lasers sources and placed at the driving point of an antenna or an antenna array [4, 5]. Despite all the efforts the THz power obtained using photomixers is still very low: about 1 mW at 1 THz and 0.2 mW at 2 THz. The reason is that the optical

heterodyne process in photoconductors has a very poor efficiency. Another very important problem of photomixers is the synthesis of the difference of the optical frequencies. This is done with two CW semiconductor lasers, which are phase-locked, one of the lasers being tunable. The synthesis of optical difference frequencies is generally implemented with quite complicated setups [6].

Continuous tunable CW THz frequencies can also be obtained by parametric light scattering from the stimulated polariton scattering in nonlinear crystals. Optical nonlinear crystals such as $LiNbO_3$ or MgO doped $LiNbO_3$ produce stimulated polariton scattering when they are strongly pumped with a ns pulsed laser in the near-infrared region. The envelope of the THz signal generated in the way indicated above is a pulse with a duration of 3–4 ns; so that the THz signal oscillating at a ps scale can be viewed as a CW source with a large range of tunability (0.7–3 THz) and high peak powers (100 mW). However, since the pump is a bulky Q-switch Nd:YAG laser and since the distance between the mirrors of the optical cavity is 15 cm (only the nonlinear crystal is 6:5 cm long) this THz source is not miniaturized, but fits on a tabletop [7, 8].

One of the most exciting approaches to generate tunable THz radiation is the quantum cascade lasers (QCLs). Quantum cascade laser idea was proposed in 1971 [9] as a FIR radiation source and experimentally demonstrated in 1994 [10]. In a quantum cascade laser the light produced by one carrier transition between two levels is amplified due to photon-assisted tunneling of a single type of carriers in a sequence of coupled quantum wells (superlattice) that has a staircase-like band energy. The number of amplification stages dictates the output power. The radiation frequency is determined by

the energy difference of sub-bands between which radiative/lasing transitions occur. The first quantum cascade laser working in the THz range was reported in 2002 [11]. This laser delivers about 2 mW power at 4.4 THz and operates at 50 K. The output power decreases dramatically with increasing temperature and becomes nearly zero at room temperature.

Recently, intracavity difference-frequency generation (DFG) in mid-infrared QCLs (THz DFG-QCLs) allowed demonstration of electrically pumped monolithic semiconductor sources operable at room temperature in the 1–5 THz range. With the introduction of the Cherenkov waveguide scheme [12], the power output of THz DFG-QCLs has been dramatically improved. THz quantum cascade laser with a spectral tunability from 1.0 to 4.6 THz and power of 32 µW at room temperature has been demonstrated [13]. It is based on difference frequency generation in a heterostructure comprising over 60 layers and Cerenkov phase-matching scheme along with integrated dual-period distributed feedback gratings. More recently, UT Austin group demonstrated a ridge waveguide quantum cascade laser operating at room temperature and electrically tunable between 3.44 and 4.02 THz with the maximum output power of 6.3 µW [14]. The realization of a quantum cascade laser at THz frequencies encounters a series of difficulties and limitations due to the very large values of the wavelength. Among them are very large free-carrier absorption losses and the necessity of growing a very thick heterostructure. The 4.4 THz quantum laser mentioned above had 104 periods, each period containing 7 coupled quantum wells, each quantum well having two AlGaAs barriers (with a thickness of 1–4 nm) and one GaAs well (10–20 nm thick), resulting in a total number of 728 quantum wells. It is not at all easy to manufacture such a heterostructure.

Among all the major approaches of designing the THz emitters, the use of optical methods especially difference frequency generation (DFG) has been the most popular technique [15-24]. Z. Ruan *et. al.* investigated a metallic slot waveguide with a dielectric strip embedded within in order to achieve enhanced THz generation from DFG, but the use of metallic structures incurred extra losses for both the optical and THz waves and most importantly it was designed to generate a single DFG frequency at 3 THz [15]. K. Saito *et. al.* reported another scheme for efficient THz wave generation utilizing a GaP ridge waveguide embedded in a silicon slot waveguide. However, they employed birefringence phase matching technique, which led to perfect phase matching for only a single DFG frequency at 2.26 THz [23]. A. Andronico *et.al.* proposed a room temperature THz emitter based on DFG in a triply resonant Au/AlAs/GaAs/AlAs/Au microcylinder [20]. However, it has a very short spectral range between 2.4 and 6 THz. T. Baehr-Jones *et. al.* proposed a silicon based source employing nonlinear polymer for radiation in the 0.5-14 THz regime [25]. However, it was not possible to cover the abovementioned range of THz generation in one single device geometry due to the challenges associated with satisfying DFG phase matching conditions. Therefore, they proposed seven different devices with dimension variations to generate THz in the range of 0.5-2 THz, 2-2.5 THz, 2.5-3 THz, 3-3.5 THz, 3.5-5 THz, 5-6 THz, and 6-14 THz, respectively.

This short review presents that there is a strong need for research efforts to realize continuously tunable, room temperature, compact THz emitters covering the whole THz spectral range and delivering a few mW output power. The research works presented in this dissertation address this need and aims to design tunable and compact THz emitters

based on nonlinear photonics combined with silicon photonics and surface plasmon photonics.

2.2   Fundamentals of Nonlinear Optics

"Physics would be dull and life most unfulfilling if all physical phenomena around us were linear. Fortunately, we are living in a nonlinear world. While linearization beautifies Physics, nonlinearity provides excitement in Physics." [26]

2.2.1   Maxwell Equations in Nonlinear Optical Media

Nonlinear optics is the study of the behavior of light in nonlinear media, where the dielectric polarization responds nonlinearly to the applied electric field strength of the light. The physical laws with electromagnetic radiation can be summarized by the famous Maxwell equations, [26-30]

$$\nabla \cdot \mathbf{D} = \rho$$
$$\nabla \times \mathbf{E} = -\frac{\partial \mathbf{B}}{\partial t}$$
$$\nabla \cdot \mathbf{B} = 0 \qquad\qquad (2.1)$$
$$\nabla \times \mathbf{H} = \mathbf{J} + \frac{\partial \mathbf{D}}{\partial t}$$

where the electric quantities $\mathbf{D}$ and $\mathbf{E}$ are the electric displacement field and the electric field, respectively. The magnetic quantities $\mathbf{B}$ and $\mathbf{H}$ are the magnetic flux density and the magnetic field, respectively. The quantities associated with the medium itself are ρ, the free charge density, and $\mathbf{J}$, the free current density. These electric quantities, $\mathbf{D}$ and $\mathbf{E}$, are related with each other through the electric polarization field, $\mathbf{P}$, which is defined by the

material response to external electromagnetic radiation. Similarly, magnetic quantities are connected through magnetization, $\mathbf{M}$, of the medium [26-27].

$$\mathbf{D} = \varepsilon_0\mathbf{E} + \mathbf{P}$$
$$\mathbf{B} = \mu_0\mathbf{H} + \mathbf{M}$$

(2.2)

With the assumption of no free charge and no free currents in a nonmagnetic media, we take the curl of $\nabla \times \mathbf{E}$ and combine Eq. (2.1) and (2.2) and reach to the following expression,

$$\nabla^2\mathbf{E} - \frac{1}{c^2}\frac{\partial^2\mathbf{E}}{\partial t^2} = \frac{1}{\varepsilon_0 c^2}\frac{\partial^2\mathbf{P}}{\partial t^2}$$

(2.3)

In nonlinear optics, the optical response or the polarization field is described in terms of the applied electric field strength with the following expression,

$$\mathbf{P} = \varepsilon_0\chi^{(1)}\mathbf{E} + \varepsilon_0\chi^{(2)}\mathbf{E}^2 + \varepsilon_0\chi^{(3)}\mathbf{E}^3 + \cdots$$
$$\equiv \mathbf{P}^{(1)} + \mathbf{P}^{(2)} + \mathbf{P}^{(3)} + \cdots$$
$$\equiv \mathbf{P}^{(1)} + \mathbf{P}^{NL}$$

(2.4)

where ε_0 is the permittivity of free space, $\chi^{(1)}$, $\chi^{(2)}$, and $\chi^{(3)}$ are known as linear, second-order nonlinear optical and third-order nonlinear optical susceptibilities, respectively. Now, after substituting Eq. (2.4) into Eq. (2.3), the wave equation becomes

$$\nabla^2\mathbf{E} - \frac{\varepsilon}{c^2}\frac{\partial^2\mathbf{E}}{\partial t^2} = \frac{1}{\varepsilon_0 c^2}\frac{\partial^2\mathbf{P}^{NL}}{\partial t^2}$$

(2.5)

where $\varepsilon = 1 + \chi^{(1)}$ is a dimensionless quantity, known as relative permittivity or dielectric constant of the medium. The reason why the polarization plays a vital role in the description

18

of nonlinear optical phenomena is that a time-varying polarization can act as the source of new components of the electromagnetic field, as expressed by the above equation. This expression can be interpreted as an inhomogeneous wave equation in which the polarization associated with nonlinear response drives the electric field. Since, $\partial^2 \mathbf{P}^{NL} / \partial t^2$ is a measure of the acceleration of the charges that constitute the medium, this wave equation is consistent with Larmor's theorem of electromagnetism, which states that accelerated charges generate electromagnetic radiation [29]. This equation thus describes the wave that will be generated from the nonlinear polarization.

2.2.2   Nonlinear Optical Processes

Here, we will describe the nonlinear optical processes associated with second-order susceptibility, $\chi^{(2)}$. To illustrate the nonlinear frequency conversion processes, let us consider a circumstance in which two optical waves oscillating at frequencies ω_1 and ω_2 are incident upon a second-order nonlinear optical medium, which we can express as,

$$\mathbf{E}(t) = E_1 \exp(-i\omega_1 t) + E_2 \exp(-i\omega_2 t) + c.c. \tag{2.6}$$

Nonlinear polarization contributed by second-order susceptibility is given by [29],

$$
\begin{aligned}
\mathbf{P}^{(2)}(t) &= \varepsilon_0 \chi^{(2)} \mathbf{E}(t)^2 \\
&\equiv \varepsilon_0 \chi^{(2)} E_1^{\;2} \exp(-2i\omega_1 t) + \varepsilon_0 \chi^{(2)} E_2^{\;2} \exp(-2i\omega_2 t) + \\
&\quad 2\varepsilon_0 \chi^{(2)} E_1 E_2 \exp[-2i(\omega_1 + \omega_2)t] + \\
&\quad 2\varepsilon_0 \chi^{(2)} E_1 E_2^{\;*} \exp[-2i(\omega_1 - \omega_2)t] + \\
&\quad 2\varepsilon_0 \chi^{(2)} [E_1 E_1^{\;*} + E_2 E_2^{\;*}]
\end{aligned}
\tag{2.7}
$$

It is clearly observed that the polarization term now constitutes all different frequencies other than the input frequencies. Thus, this second-order nonlinear polarization, coupled into the wave Eq. (2.5), acts as a source to generate electric field at this new frequencies. The complex amplitudes of the various frequency components of the polarization term are summarized below with the appropriate name of the physical process, that each term represents,

$$\mathbf{P}(2\omega_1) = \varepsilon_0\chi^{(2)}E_1^{\ 2} : \text{Second Harmonic Generation (SHG)}$$
$$\mathbf{P}(2\omega_2) = \varepsilon_0\chi^{(2)}E_2^{\ 2} : \text{Second Harmonic Generation (SHG)}$$
$$\mathbf{P}(\omega_1 + \omega_2) = 2\varepsilon_0\chi^{(2)}E_1E_2 : \text{Sum Frequency Harmonic Generation (SFG)} \qquad (2.8)$$
$$\mathbf{P}(\omega_1 - \omega_2) = 2\varepsilon_0\chi^{(2)}E_1E_2^{\ *} : \text{Difference Frequency Generation (DFG)}$$
$$\mathbf{P}(0) = 2\varepsilon_0\chi^{(2)}(E_1E_1^{\ *} + E_2E_2^{\ *}) : \text{Optical Rectification (OR)}$$

2.2.2.1 Difference Frequency Generation

Difference frequency generation (DFG) is a second order nonlinear optical process, in which two optical waves at frequency ω_1 and ω_2 interact with a nonlinear optical medium to generate an output wave at the difference frequency $\omega_3 = \omega_1 - \omega_2$ [30]. Geometry of the interaction and photon energy level diagram for DFG are illustrated in Figure 2.1. Conservation of energy requires that for a photon generated at difference frequency (ω_3), a photon at the higher input frequency (ω_1) must be destroyed and another photon at the lower input frequency (ω_2) must be created. According to the photon energy level description of DFG, atom in the nonlinear medium first absorbs a photon at ω_1 and jumps to the highest virtual level and then decays by a two photon emission process, that is further stimulated by the presence of the input ω_2 field.
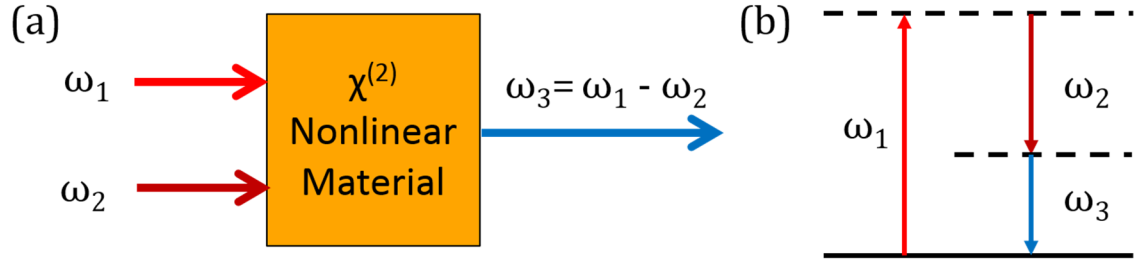
Figure 2.1 | Difference frequency generation. (a) Geometry of the interaction (b) Energy level description.

In this dissertation, we used DFG phenomenon to generate tunable THz radiation. We kept the input idler wave fixed at 1550 nm wavelength and then varied the input pump waves from 1546 nm to 1474 nm to achieve continuously tunable THz radiation across 0.5-10 THz.

2.2.2.2 Nonlinear Optical Materials

In order to observe successful DFG in THz range, nonlinear optical materials possessing the property of high second-order nonlinear susceptibility, $\chi^{(2)}$, need to be used in the designed platform. Some commercially available popular nonlinear materials and polymers such as aluminum nitride (AlN), potassium titanyl phosphate (KTP), gallium selenide (GaSe), Barium titanate ($BaTiO_3$), Lithium Niobate ($LiNbO_3$), Potassium Niobate ($KNbO_3$), monopotassium phosphate (KH_2PO_4, KDP), lithium tri-borate (LBO), β-barium borate (BBO) and SEO100 polymer from Soluxra Company can be considered for the designed THz emitters. Throughout this dissertation, for all the designed THz emitters, we have used optical properties of AlN for the nonlinear optical material due to its easy processing and being readily available.

2.2.2.3 Manley-Rowe Quantum Limit

According to Manly-Rowe relations, in DFG, annihilation of a number of photons at pump frequency ω_1 is associated with the creation of the same number of photons at THz frequency ω_T and idler frequency ω_2 [31-33]. This introduces an upper limit of the optical to THz conversion efficiency, also known as quantum efficiency. The highest achievable conversion efficiency is defined by the ratio of the generated wave frequency, ω_T, to the input pump wave frequency, ω_1. For instance, if we assume input optical pump wave at 200 THz frequency is used to generate 0.5 THz DFG, then the upper limit of optical power to THz power conversion efficiency is 0.25%. For 10 THz DFG, the efficiency rises up to 5%.

2.3   References

1. Eisele, H., Rydberg, A., & Haddad, G. I. (2000). Recent advances in the performance of InP Gunn devices and GaAs TUNNETT diodes for the 100-300-GHz frequency range and above. IEEE Transactions on Microwave Theory and Techniques, 48(4), 626-631.

2. Eisele, H. (2002). Conventional and novel approaches to RF power generation with two-terminal devices at terahertz frequencies. In Terahertz Electronics Proceedings, 2002. IEEE Tenth International Conference on (pp. 13-18). IEEE.

3. Dragoman, D., & Dragoman, M. (2004). Terahertz fields and applications. Progress in Quantum Electronics, 28(1), 1-66.

4. Siebert, K. J., Quast, H., & Roskos, H. G. (2001). Perspectives of continuous-wave optoelectronic THz imaging. In Terahertz sources and systems (pp. 127-143). Springer Netherlands.

5. Duffy, S. M., Verghese, S., & McIntosh, K. A. (2003). Photomixers for continuous-wave terahertz radiation. In Sensing with terahertz radiation (pp. 193-236). Springer Berlin Heidelberg.

6. Siebert, K., Siebe, F., Thomson, M., Baghbidi, J. Z., Leonhardt, R., & Roskos, H. G. (1999, September). Advances in continuous-wave THz generation. In Industrial Lasers and Inspection (EUROPTO Series) (pp. 234-243). International Society for Optics and Photonics.

7. Shikata, J. I., Kawase, K., Karino, K. I., Taniuchi, T., & Ito, H. (2000). Tunable terahertz-wave parametric oscillators using $LiNbO_3$ and $MgO: LiNbO_3$ crystals. IEEE Transactions on Microwave theory and Techniques, 48(4), 653-661.

8. Kawase, K., Shikata, J. I., & Ito, H. (2002). Terahertz wave parametric source. Journal of Physics D: Applied Physics, 35(3), R1.

9. Kazarinov, R. F., & Suris, R. A. (1971). Possibility of amplification of electromagnetic waves in a semiconductor with a superlattice. Soviet Physics Semiconductors-USSR, 5(4), 707-709.

10. Walther, C., Fischer, M., Scalari, G., Terazzi, R., Hoyler, N., & Faist, J. (2007). Quantum cascade lasers operating from 1.2 to 1.6 THz. Applied Physics Letters, 91(13), 131122.

11. Köhler, R., Tredicucci, A., Beltram, F., Beere, H. E., Linfield, E. H., Davies, A. G., Ritchie, D.A., Iotti, R.C., & Rossi, F. (2002). Terahertz semiconductor-heterostructure laser. Nature, 417(6885), 156-159.

12. Vijayraghavan, K., Adams, R. W., Vizbaras, A., Jang, M., Grasse, C., Boehm, G., Amann, M.C., & Belkin, M. A. (2012). Terahertz sources based on Čerenkov difference-frequency generation in quantum cascade lasers. Applied physics letters, 100(25), 251104.

13. Lu, Q. Y., Bandyopadhyay, N., Slivken, S., Bai, Y., & Razeghi, M. (2012). Widely tuned room temperature terahertz quantum cascade laser sources based on difference-frequency generation. Applied Physics Letters, 101(25), 251121.

14. Jung, S., Jiang, A., Jiang, Y., Vijayraghavan, K., Wang, X., Troccoli, M., & Belkin, M. A. (2014). Broadly tunable monolithic room-temperature terahertz quantum cascade laser sources. Nature communications, 5.

15. Ruan, Z., Veronis, G., Vodopyanov, K. L., Fejer, M. M., & Fan, S. (2009). Enhancement of optics-to-THz conversion efficiency by metallic slot waveguides. Optics express, 17(16), 13502-13515.

16. Theuer, M., Molter, D., Maki, K., Otani, C., L'huillier, J. A., & Beigang, R. (2008). Terahertz generation in an actively controlled femtosecond enhancement cavity. Applied Physics Letters, 93(4), 041119.

17. Kukushkin, V. A. (2006). Efficient generation of terahertz pulses from single infrared beams in C/GaAs/C waveguiding heterostructures. JOSA B, 23(12), 2528-2534.

18. Morozov, Y. A., Nefedov, I. S., Aleshkin, V. Y., & Krasnikova, I. V. (2005). Terahertz oscillator based on nonlinear frequency conversion in a double vertical cavity. Semiconductors, 39(1), 113-118.

19. Burgess, I. B., Rodriguez, A. W., McCutcheon, M. W., Bravo-Abad, J., Zhang, Y., Johnson, S. G., & Lončar, M. (2009). Difference-frequency generation with quantum-limited efficiency in triply-resonant nonlinear cavities. Optics express, 17(11), 9241-9251.

20. Andronico, A., Claudon, J., Gérard, J. M., Berger, V., & Leo, G. (2008). Integrated terahertz source based on three-wave mixing of whispering-gallery modes. Optics letters, 33(21), 2416-2418.

21. Bieler, M. (2008). THz generation from resonant excitation of semiconductor nanostructures: Investigation of second-order nonlinear optical effects. IEEE Journal of Selected Topics in Quantum Electronics, 14(2), 458-469.

22. Avetisyan, Y. H. (November, 1999). Cavity-enhanced terahertz region difference frequency generation in surface-emitting geometry. In SPIE's International Symposium on Optical Science, Engineering, and Instrumentation (pp. 501-506). International Society for Optics and Photonics.

23. Saito, K., Tanabe, T., & Oyama, Y. (2015). Design of an efficient terahertz wave source from a GaP waveguide embedded in a silicon slot waveguide. Journal of the European Optical Society-Rapid publications, 10.

24. Vodopyanov, K. L., Fejer, M. M., Yu, X., Harris, J. S., Lee, Y. S., Hurlbut, W. C., Kozlov, V.G., Bliss, D., & Lynch, C. (2006). Terahertz-wave generation in quasi-phase-matched GaAs. Applied Physics Letters, 89(14), 141119.

25. Baehr-Jones, T., Hochberg, M., Soref, R., & Scherer, A. (2008). Design of a tunable, room temperature, continuous-wave terahertz source and detector using silicon waveguides. JOSA B, 25(2), 261-268.

26. Shen, Y. R. (1984). The principles of nonlinear optics. New York, Wiley-Interscience.

27. Kujala, S. (2008). Optical second-harmonic generation from metal nanostructures. Tampere University of Technology.

28. Jackson, J. D. (1975). Electrodynamics. Wiley-VCH Verlag GmbH & Co. KGaA.

29. Boyd, R. W. (2008). Nonlinear Optics. Nonlinear Optics: Third Edition. By Robert W. Boyd. ISBN 978-0-12-369470-6. Published by Academic Press/Elsevier, Inc. Oxford, UK.

30. Lee, Y. S. (2009). Principles of terahertz science and technology (Vol. 170). Springer Science & Business Media.

31. Chen, T., Sun, J., Li, L., & Tang, J. (2012). Proposal for efficient terahertz-wave difference frequency generation in an AlGaAs photonic crystal waveguide. Journal of Lightwave Technology, 30(13), 2156-2162.

32. Suhara, T., & Fujimura, M. (2013). Waveguide nonlinear-optic devices (Vol. 11). Springer Science & Business Media.

33. Waldmueller, I., Wanke, M. C., & Chow, W. W. (2007). Circumventing the Manley-Rowe quantum efficiency limit in an optically pumped terahertz quantum-cascade amplifier. Physical review letters, 99(11), 117401.

CHAPTER 3

Tunable Room Temperature THz Sources based on Nonlinear Mixing in a Hybrid Optical and THz Micro-ring Resonator

3.1   Proposed Device

Compactness, broad tunability, simple alignment, and stable THz output are sought after properties in the new generation THz sources. We propose a tunable, compact room temperature THz source that could radiate in 0.5–10 THz with a tunability resolution of 0.05 THz. Figure 3.1 shows the proposed hybrid tunable THz source device with a 3D schematic and cross-section. The hybrid device consists of an optical ring resonator (orange colored) with the outer radius of 360 µm, width of 0.6 µm, thickness of 0.5 µm for the investigated case and with a material (e.g. AlN, $BaTiO_3$, $LiNbO_3$, polymer) having second order nonlinear susceptibility ($\chi^{(2)}$). We employ an optical straight bus waveguide placed at close proximity to the nonlinear ring in order to carry in the appropriate input infrared pump and idler waves so that it could generate DFG in the desired THz regime. These input waves will couple via evanescent field waves to the nonlinear ring where they are enhanced due to high Q factor of the resonator. The enhanced input waves make multiple round trips in the ring with resonant optical modes and generate THz waves via DFG phenomenon while interacting with the nonlinear material. Since the nonlinear ring cannot sustain the generated THz waves within itself due to their longer wavelength compared to input infrared, we added a THz ring resonator made of high resistivity Si with the same outer radius of 360 µm, 200 µm width and 120 µm thickness underneath the nonlinear ring resonator. The generated THz waves propagate in the THz ring with resonant THz modes

satisfying phase matching condition. Optical and THz resonators are separated by an insulation layer of 1 μm thick SiO$_2$ ring with same width of optical ring so that optical waves could propagate and interact well with the nonlinear material in nonlinear ring without being depleted via evanescent coupling to the THz ring with high-index Si. An engineered THz straight waveguide is placed underneath the input bus waveguide with the same insulation layer of SiO$_2$ so that it could out-couple the THz waves from the THz ring resonator and guide them to any point of interest including an antenna for out-coupling to free space. The device could be permanently bonded with quartz glass or borosilicate substrate. By keeping the idler input wave fixed at 1550 nm and varying the pump wave from 1546 nm to 1474 nm at each 0.4 nm interval satisfying resonance condition of the ring, the proposed THz source could emit THz radiation in 0.5 to 10 THz range with tunability resolution of 0.05 THz.
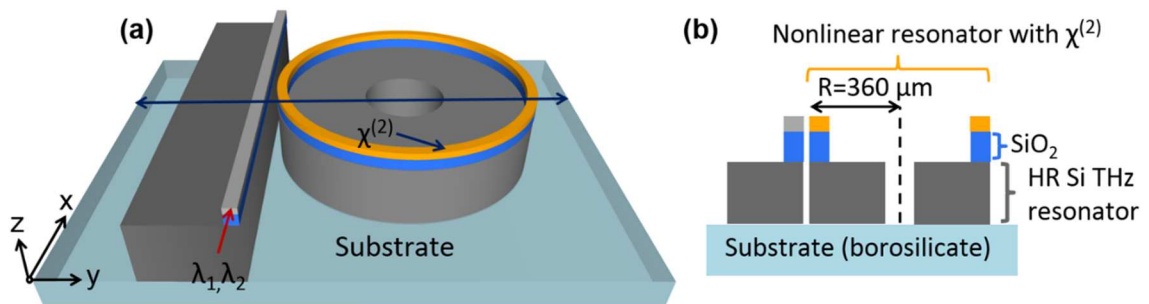
Figure 3.1. Proposed tunable THz source. (a) 3D schematic of the THz source device based on a hybrid nonlinear optical and THz micro-ring resonator. (b) Cross-sectional schematic of the proposed source device.

3.2 Results and Discussion

In this section, the design process of the micro-ring resonators and phase matching are presented. Then simulation results of the source device carried out in commercial simulation tools based on FDTD and FEM are presented in detail. Following, the expected output power of the proposed emitter is calculated analytically for selected nonlinear optical materials using the DFG theory. Finally proposed fabrication plan along with the attempted efforts and challenges are described.

3.2.1 Design of Micro-Ring Resonators

Micro-ring resonator is now considered as one of the most important building block of integrated photonics and has gained widespread interest over the past few years. It consists of a waveguide in a closed loop, commonly in the shape of a ring or racetrack. When placing the loop within close proximity of an input waveguide, light can be coupled into the cavity via evanescent field and light waves can propagate to circulate around the periphery of the cavity. Resonance take place because of the constructive interference for light whose phase change after each full trip around the closed loop is an integer multiple of 2π, i.e., in phase with the incoming light. Waves that do not meet this resonance condition are transmitted through the input waveguide. Resonance wavelength of the ring is defined by [1],

$$m\lambda_m = 2\pi R_{eff} n_{eff} \tag{3.1}$$

where m, λ_m, R_{eff}, and n_{eff} are resonant azimuthal mode number, resonant wavelength with mode number m, effective radius of the ring and effective mode index of the material in

28

the ring respectively. Minimum attenuation for the optical wave propagation in the ring resonator can be achieved if it is properly designed. One of the important parameters for designing a ring resonator is free spectral range (FSR), which is defined as the distance between two consecutive resonant peaks in the ring. The lower the FSR the higher the number of resonant absorption peaks in the ring for a particular bandwidth. The lower FSR is needed because tunability resolution of the source device is directly related to the number of resonant peaks in optical region. The relation between FSR and radius of the ring is defined by [1],

$$FSR = \frac{c}{2\pi n_g R_{eff}}$$
(3.2)

where c is the speed of light, n_g is the group index and R_{eff} is the effective radius of the ring. Group index takes into account the dispersion of the ring waveguide and is defined by [1],

$$n_g = n_{eff} - \lambda_m \frac{dn_{eff}}{d\lambda}$$
(3.3)

To calculate the group index, one needs to find the dispersion of the nonlinear waveguide. By using the eigenmode solver of finite element method based simulation tool, we investigated the effective mode indices of fundamental optical modes in the nonlinear optical waveguide considering the cross-section structure illustrated in Fig. 3.2(a). An isolation layer of SiO_2 with 1 μm thickness was used underneath the optical waveguide to prevent the evanescent coupling for the optical signal into the THz Si waveguide. We used the refractive index of aluminum nitride for the nonlinear waveguide in the eigenmode

simulation. With a fixed waveguide height of 0.5 μm, we simulated the effective mode indices of the nonlinear waveguide for three different waveguide widths of 0.6 μm, 0.8 μm and 1.0 μm. Simulated dispersion characteristics of the nonlinear waveguide for the input infrared waves ranging from 1350 nm to 1560 nm is shown in Fig. 3.2(c). It is observed that effective mode indices of the fundamental optical mode in the optical waveguide decrease with the increase in wavelength. Also, effective index for the fundamental mode of a specific wavelength decreases with a decrease in width of the waveguide while we keep the height constant. Equation (3.2) suggests that group index and effective radius of the ring is inversely proportional. So we look forward to minimizing the radius of the ring resonator by maximizing the group index. Group index of the waveguide can be calculated from the dispersion curves shown in Fig. 3.2(c) by applying equation (3.3). We found the group indices as 2.43, 2.51 and 2.65 for three different waveguide widths of 1 μm, 0.8 μm and 0.6 μm, respectively with 0.5 μm height. It is evident that smaller waveguide dimension gives larger group index. However, for the width smaller than 0.6 μm, it becomes very hard to confine the infrared input waves in the waveguide. Thus 0.6 μm width and 0.5 μm height values were chosen for the nonlinear waveguide which resulted the fundamental mode of 1550 nm shown in Fig. 3.2(b). For the investigated device, the tunability resolution or *FSR* of the nonlinear ring was set to 0.05 THz. By applying the group index of 2.65 and *FSR* of 0.05 THz in equation (3.2), we calculated outer radius of the nonlinear optical ring resonator to be 360 μm.
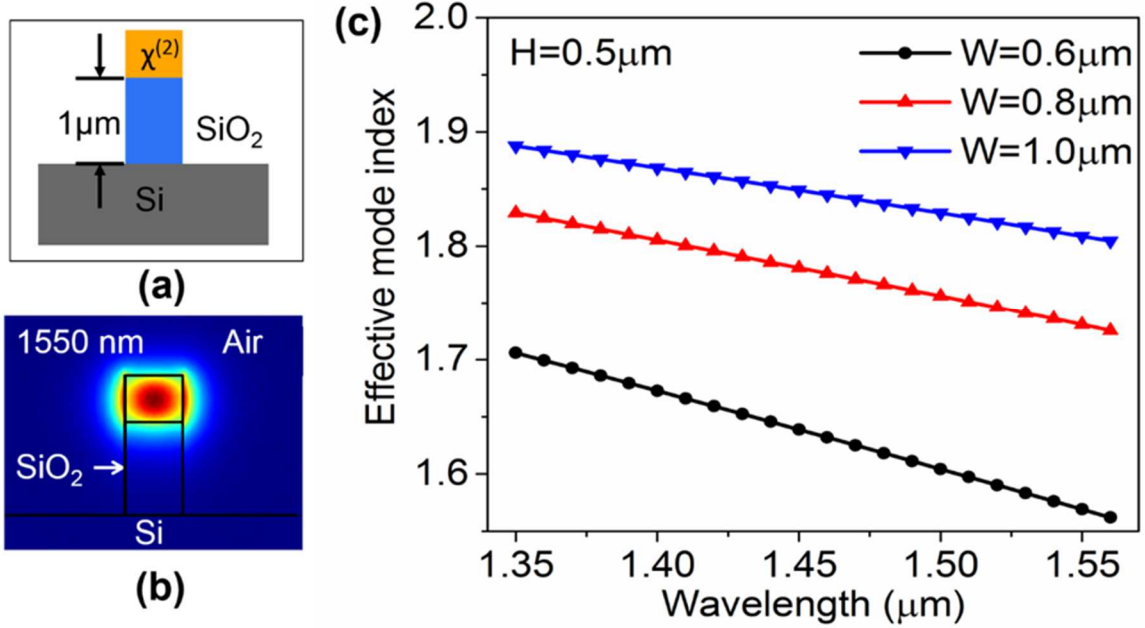
Figure 3.2 | Dispersion of nonlinear optical waveguide. (a) Cross-sectional schematic of the waveguide used to investigate optical mode indices by employing eigenmode solver. (b) Optical mode at 1550 nm with effective index of 1.5693 for 0.6 μm wide and 0.5 μm thick optical waveguide. (c) Simulated effective mode indices for three different waveguide widths (W=0.6 μm, 0.8 μm and 1.0 μm) of optical waveguide with a fixed height (H=0.5 μm) for 1350 nm to 1560 nm optical range.

If the gap between the bus waveguide and ring resonator is set at critical coupling condition, transmitted power in the bus waveguide drops to zero at resonant frequencies. This happens only when the coupled power is equal to the power loss in the ring ($\kappa^2=1-\alpha^2$), where κ^2 is defined as the fraction of power coupling between the bus waveguide and the micro-ring resonator and α is the amplitude after wave attenuation over one round trip in the ring [1]. In order to achieve efficient difference frequency generation in 0.5-10 THz, critical coupling needs to be maintained over 1474 nm to 1550 nm infrared waves in the nonlinear ring resonator. For this infrared band, we simulate the amplitude transmission α in the nonlinear ring with radius of 360 μm to be 0.99. Critical coupling is achieved at a

gap of 600 nm providing κ^2 to be 0.02. Simulated transmission spectrum of the nonlinear optical ring resonator with 360 μm radius and 600 nm coupling gap is presented in Fig. 3.3(a). We also show the Q factor for different coupling gap in Fig. 3.3(b). At critical coupling gap, we found the optical Q factor to be 620,000 near 1550 nm. When the coupling gap is increased beyond this critical point, the ring is operated in a weakly coupled regime leading to improved Q factors around 1,500,000 which are expected to correspond more closely to the resonator's intrinsic quality factor.

Mode number for the resonant optical modes in the resonator can also be estimated by applying resonant wavelengths observed in transmission spectrum and their respective effective indices from Fig. 3.2(c) in equation (3.1). For instance, 1550 nm optical wave, we found the resonant mode number to be (1, 2288). Here '1' and '2288' represent radial and azimuthal mode number respectively. κ^2 is defined as the fraction of power coupling between the bus waveguide and the micro-ring resonator. The waveguide power coupling coefficient κ^2 and the propagation power loss coefficient κ_p^2 can be estimated from transmission spectrum of the ring resonator to be $\kappa^2 = \pi \times (FWHM) \times [1 - \sqrt{\gamma}] / FSR$ and

$\kappa_p^2 = 2\pi \times (FWHM) \times \sqrt{\gamma} / FSR$, where γ is defined as the minimum power transmission in the through-port and FWHM is the full width at half maximum of the resonant peak [2]. To be compared with the losses in straight waveguides, which is often quoted in dB/cm, the propagation loss in a microring resonator can be expressed as $-10 \times \log_{10}(1 - \kappa_p^2) / (2\pi R_{eff})$, where $2\pi R_{eff}$ is the perimeter of the microring resonator [2]. From the transmission spectrum of the critically coupled ring resonator over the infrared range of our interest, we calculated the FWHM, FSR and γ to be 2.5±0.1 pm, 0.4±0.01

nm and 0.001±0.0005. The estimated κ^2 and κ_p^2 are 0.019±0.0014, 0.0012±0.0004 respectively and the corresponding propagation loss is 0.023±0.01 dB/cm. Using the value of minimum power transmission γ, we also found high extinction ratios of 30±3 dB for the ring resonator over the infrared range of our interest.
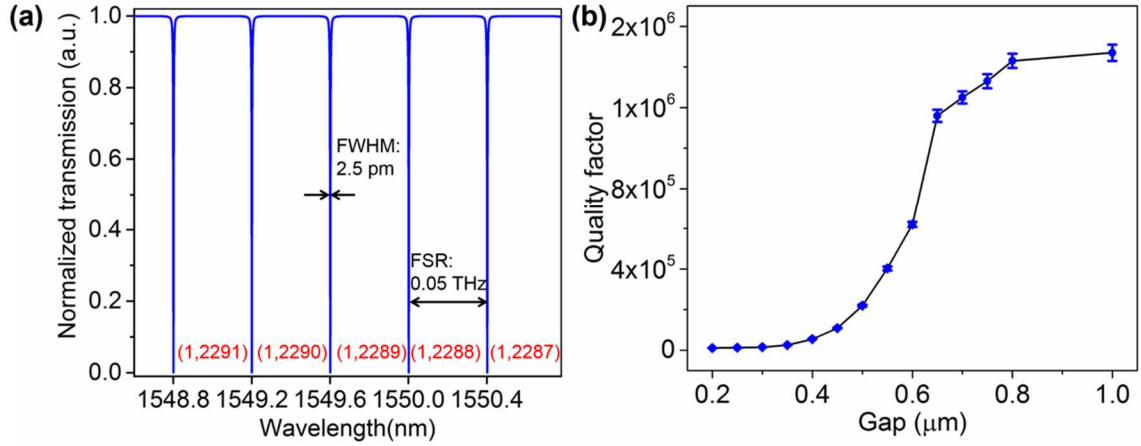
Figure 3.3 | Transmission spectrum of optical ring resonator. (a) Transmission spectrum of the nonlinear optical micro-ring resonator with 360 μm radius, 0.6 μm width and 600 nm critical coupling gap. The Q factor and FSR are extracted to be 620,000 and 0.05 THz respectively. Numbers (red) at each absorption peak represent resonant mode number (radial, azimuthal) in the ring resonator for that wavelength. (b) The dependence of Q factors on the coupling gap of micro-ring resonator.

3.2.2 Phase Matching Condition

Satisfying the phase matching condition (PMC) is the most challenging part of the design. Only if this condition is satisfied, the generated THz will co-propagate with the optical waves and show coherent amplification. Phase matching condition can be written as,

33

$$n_3 = \frac{n_{o1}\omega_1 - n_{o2}\omega_2}{\omega_3} \qquad\qquad (3.4)$$

where $\omega_1, \omega_2, \omega_3$ are input pump, idler and the generated THz angular frequencies respectively and n_{o1}, n_{o2}, n_3 are effective indices at pump, idler and THz frequencies, respectively. Since we have already designed the nonlinear optical waveguide, the THz waveguide can now be engineered to meet the PMC. By applying the effective indices of infrared input waves obtained from Fig. 3.2(c) in equation (3.4), we find that the effective indices of THz modes have to be in the range of 2.6 to 2.7 for phase matching. Hence, THz waveguide must be designed in such a way that it supports and confines the THz modes with effective indices lying in this region.

It is well known that Si can be used to guide radiation in the near-infrared (NIR), and that high resistivity Si is relatively transparent in much of the THz. Thus, high resistivity Si waveguides were chosen to guide THz for its high refractive index and it can concentrate modes with much smaller than the size of the modes of ordinary optical fibers and can be efficiently coupled to nonlinear materials or polymers [3, 4]. Loss tangent and attenuation coefficient of Si at any frequency can be calculated using the formulae $\tan\delta = 1/(\omega\varepsilon_{Si}\varepsilon_0\rho)$ and $\alpha_{Si} = (\pi\sqrt{\varepsilon_{Si}}\tan\delta)/\lambda$ respectively, where ρ is resistivity of Si and ε_0, ε_{Si} are permittivity of free space and relative permittivity of Si respectively. For low impurity concentration ε_{Si} is almost a real value, which is approximately equal to the high frequency relative permittivity. We estimate the loss tangent at 1 THz for $10 k\Omega \cdot cm$

high resistivity Si with $\varepsilon_{Si} = 11.67$ to be 1.54×10^{-5} and the attenuation coefficient to be 0.55 m^{-1}.

We investigated the dispersion of THz Si waveguides for different dimensions to find a suitable waveguide dimension with required THz mode effective indices for phase matching. For THz waveguide with a fixed height of 120 μm, we simulated effective indices of five different THz frequencies by varying the waveguide width from 120 μm to 280 μm. The simulated results are shown in Fig. 3.4(a) for 0.5, 0.8, 1.0, 1.5 and 2.0 THz. It is clearly observed that for THz wave with smaller frequency and larger wavelength like 0.5 and 0.8 THz, effective mode indices increase rapidly with a small increase in waveguide width. But if one goes further to higher frequencies of THz waves, the change in effective indices becomes nearly insignificant for a small increase in waveguide width. This is due to the smaller wavelength for which it is easier to confine the wave and find a particular mode index in that large waveguide. Waveguide width of 200 μm is chosen for which effective mode indices are in the range 2.6 to 2.7 for all the five different THz waves presented in Fig. 3.4(a). THz modal profiles are simulated by eigenmode solver in the engineered THz waveguide with 200 μm width and 120 μm height to show the confinement of THz waves with required mode indices. Modal profiles in the THz waveguide are shown in Fig 3.4(b), 3.4(c), 3.4(d) and 3.4(e) for 0.5, 1.0, 1.5 and 2.0 THz respectively.
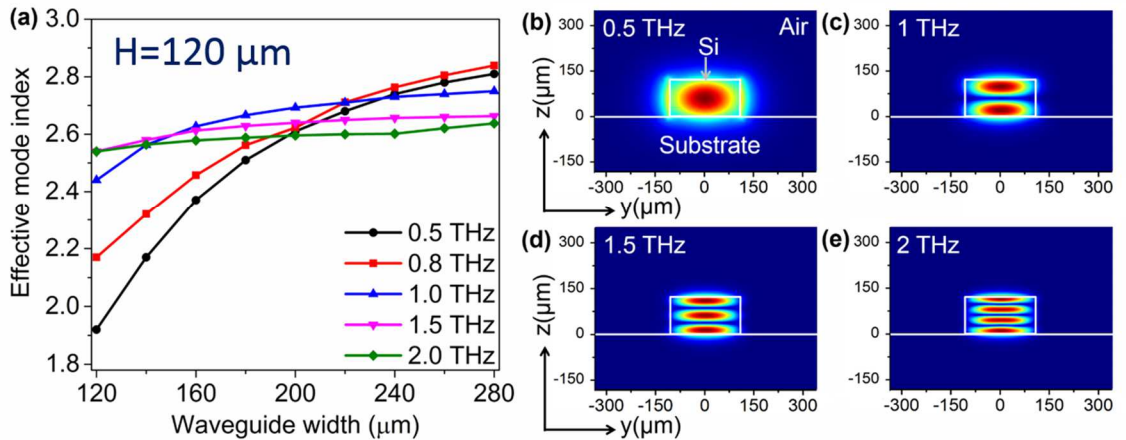
Figure 3.4. | Engineering THz waveguide satisfying phase matching condition.
(a)Simulated effective indices of the THz high resistivity Si waveguide with a fixed height of 120 μm by varying the waveguide width from 120 μm to 280 μm, showing the change in effective indices in THz waveguide for 0.5, 0.8, 1.0, 1.5 and 2.0 THz. Showing THz modal field profiles in the THz waveguide cross-section for (b) 0.5 THz (c) 1.0 THz (d) 1.5 THz and (e) 2.0 THz.

3.2.3 Numerical Simulations by FDTD and FEM

A two-tier approach was adopted for THz generation simulations due to the large physical dimensions of the entire device for the 0.5–10 THz range. First, a smaller hybrid micro-ring resonator was designed and investigated by full 3D simulations using a commercially available FDTD tool and the results were compared with the ones obtained by 2D simulations. Once the accuracy of 2D simulations was confirmed, a larger hybrid micro-ring resonator for 0.5–10 THz range was designed and investigated.

The first design includes a hybrid micro-ring resonator of 6 μm outer radius, with an optical ring resonator of 0.6 μm width and 0.5 μm thickness and input waveguides with the same dimensions. Underneath, a THz ring resonator and THz straight waveguides with the width of 3.5 μm and thickness of 2 μm were added to out-couple the generated THz

radiation. Optical and THz structures were separated by a 1 µm SiO$_2$ thick layer. For this small ring resonator, critical coupling is achieved at a gap of 500 µm. Second order nonlinear optical susceptibility $\chi^{(2)}$ was taken as 300 pm/V for the nonlinear optical ring resonator. Two optical beams at 1560 nm and 1350 nm were excited at two input straight optical waveguides respectively with electric field amplitude of 1×10^7 V/m and linewidth of 0.15 THz.

Electric field profiles at different planes from the 3D simulation are analyzed in order to fully understand how the proposed device works. First, electric field at the generated THz frequency is observed on plane A in the THz ring resonator placed underneath the nonlinear optical resonator as indicated in Fig. 3.5(a). The field profile on that plane is presented in Fig. 3.5(d) which clearly shows that the DFG THz wave is confined to the THz ring resonator with resonant mode. Then we observed electric field on another plane B as marked in Fig. 3.5(c). This plane was chosen in order to observe and prove if the THz wave generated in the nonlinear ring is coupled to the bottom THz ring resonator and also if it out-couples to the THz straight receiver waveguide from the ring resonator. The electric field presented in Fig. 3.5(e) evidently shows that the THz wave generated in the optical ring is coupling to the THz ring resonator and again from there it is out-coupling to the THz receiver waveguide. We simulated the same design also in 2D using the same FDTD tool and obtained the exact same output characteristics proving their accuracy.
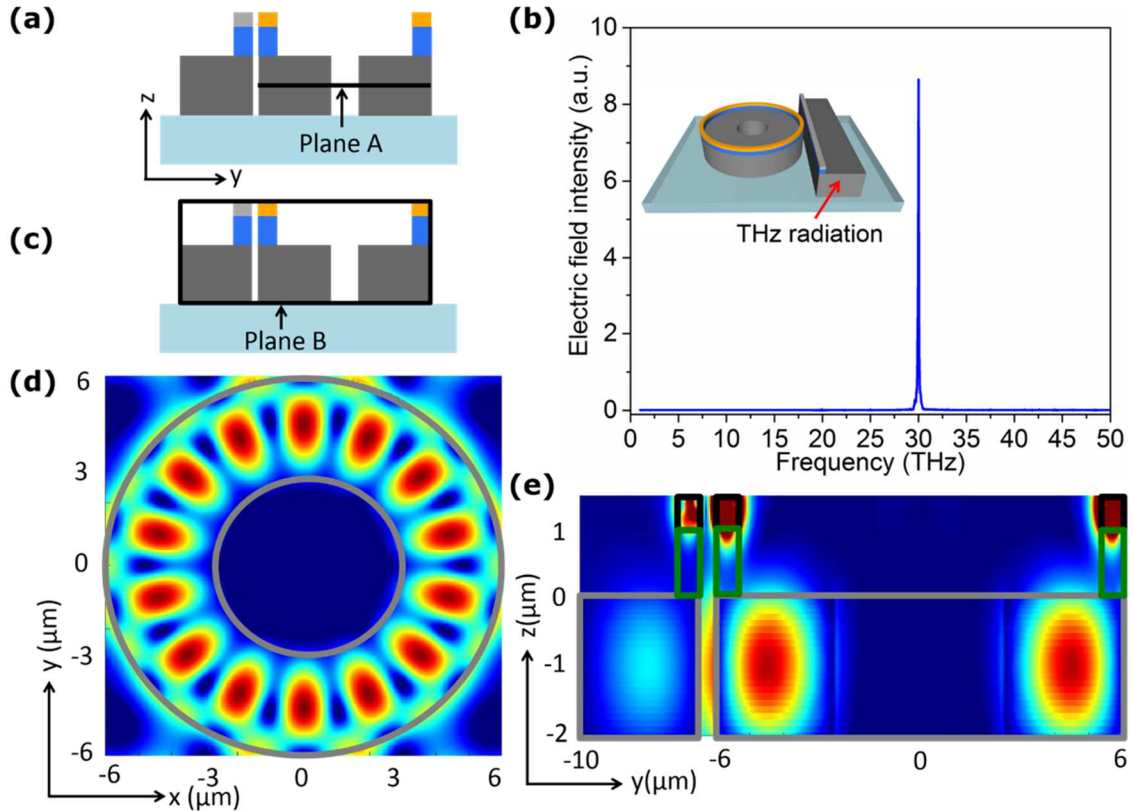
Figure 3.5 | Electric field profiles obtained from 3D simulation of a hybrid optical and THz micro-ring resonator THz source with 6µm radius. DFG is generated at 30 THz for two input optical waves at 1560 nm and 1350 nm. (a) Cross-section of the 3D THz source showing plane A in the THz ring resonator. (b) Showing 30 THz DFG field profile for plane A which is placed at XY plane in the THz ring resonator. It is clearly observed that the DFG THz is well confined in the ring with resonant mode. (c) Cross-section of the 3D THz source showing plane B. This plane was selected in order to observe the coupling of the THz generated in the nonlinear ring to THz ring resonator and THz straight waveguide as well. (d) Electric field profile on plane B where it is clearly observed that the DFG THz is coupling to the THz ring resonator placed underneath the nonlinear ring. It is also shown that THz is out-coupling from the ring resonator to the straight THz waveguide.

And finally power spectrum at the output straight THz receiver waveguide was analyzed in order to observe DFG peak. The output spectrum presented in Fig. 3.5(b) shows a clear DFG peak at 30 THz which is in good agreement with the theoretical calculations

38

for DFG process [5]. We found the linewidth of the generated THz waves to be 0.3 THz which is two times the bandwidth we set for the input infrared wave. Now we convert the 3D multi-layer structure in 2D simulation for better computational efficiency. Since only one layer with ring resonator structure can be considered in 2D, we chose to simulate only the top nonlinear optical ring resonator coupled with two input waveguides at two opposite sides. The same $\chi^{(2)}$ value of 300 pm/V was used in the nonlinear ring resonator and input waves were excited with same effective mode indices, electric field amplitude and linewidth at 1560 nm and 1350 nm respectively. Then this geometry was also simulated by the same 2D simulation tool and the exact same results were obtained proving the accuracy of 2D simulations.

In the second step, the previously described DFG emitter with 360 µm radius nonlinear ring coupled to two input optical bus waveguides was simulated in 2D using FDTD tool for output spectrum. The gap between the input bus waveguide and ring resonator was kept at 600 nm for which critical coupling condition is satisfied. The same second order nonlinear optical susceptibility $\chi^{(2)}$ of 300 pm/V was used for the nonlinear ring resonator. Electric field amplitude and linewidth of input waves were set to 1×10^7 V/m and 0.015 THz respectively. Resonant wavelengths obtained from the simulated transmission spectrum of the nonlinear ring resonator must be selected as inputs to generate a difference frequency in the ring. While the idler input wave was kept fixed at 1550 nm wavelength, another input pump wave was varied and set to 1542 nm, 1534 nm, 1526 nm, 1519 nm, 1511 nm, 1503 nm, 1496 nm, 1488nm, 1481 nm and 1474 nm consequently to achieve difference frequency generation in the THz range of our interest. The simulated

output power spectra for those different simulations are shown in Fig. 3.6(a). Sharp DFG

peak is observed near at 1 THz, 2 THz, 3 THz, 4 THz, 5 THz, 6 THz, 7 THz, 8 THz, 9 THz

and 10 THz respectively in power spectra for those different input pump waves. We found

the linewidth of the generated THz waves to be 0.03 THz which is two times the input

pump bandwidth. Here we explain how the proposed source device operates while

generating difference frequency at 5 THz only. For the input, 1550 nm idler wave with

resonant mode number (1, 2288) and 1511 nm pump wave with resonant mode number (1,

2388) were chosen to satisfy the resonant condition in the nonlinear ring resonator. These

two optical wave pulses were excited at the two ends of the input bus waveguides as it is

shown in Fig. 3.1(a). Since they satisfy the resonance condition, the input waves make

multiple round trips in high Q ring resonator cavity with enhanced optical intensity

resulting in efficient DFG process. According to the DFG theory, these two waves incident

upon a nonlinear material should produce the difference frequency field at 5 THz. Indeed,

the simulated power spectrum in the ring resonator shown in Fig. 3.6(a) clearly presents a

sharp DFG peak at 5 THz. In the proposed THz source, we expect this generated THz in

the nonlinear ring to couple to the THz ring placed underneath as it is shown for a small

scale 3D simulation in Fig. 3.5(e). Since both the optical and THz waveguide are

engineered satisfying phase matching condition, DFG THz will travel in THz ring cavity

with resonant mode and experience coherent amplification. Electric field distribution in the

THz Si micro-ring resonator with whispering gallery resonant mode is presented in Fig.

3.6(b) for 5 THz DFG. THz straight waveguides placed at two opposite sides could out-

couple the THz from the ring and guide it to any point of interest. Now, keeping the idler

optical fixed at 1550 nm and the pump optical wave could be varied around this wavelength

satisfying the resonance condition of the ring to attain difference frequency output in 0.5-10 THz with tunability resolution of 0.05 THz at the receiver end.
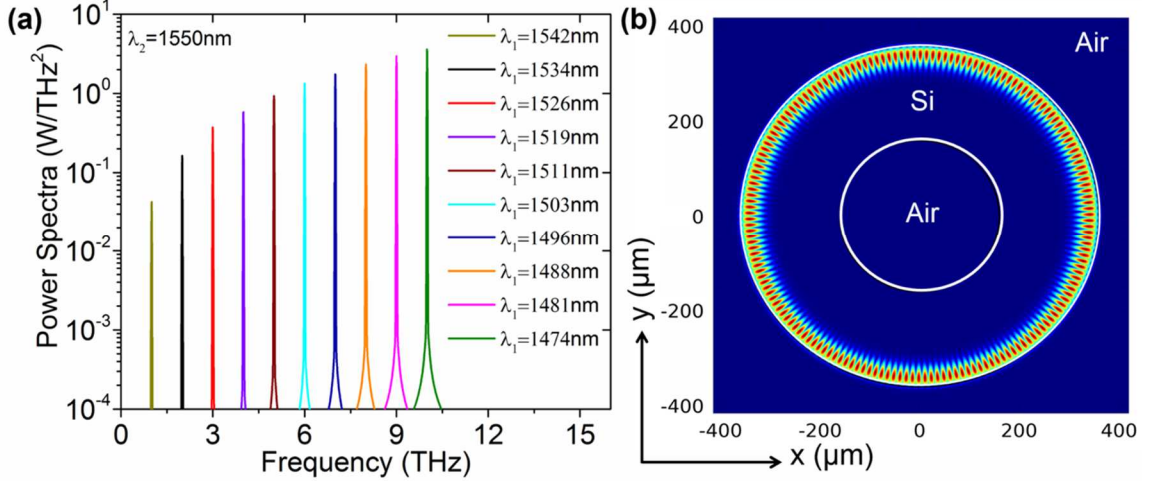
Figure 3.6 | 2D simulation result of the proposed THz source with 360 µm radius. (a) When one input beam was kept fixed at 1550 nm wavelength, another input wave was varied and set to 1542 nm, 1534 nm, 1526 nm, 1519 nm, 1511 nm, 1503 nm, 1496 nm, 1488nm, 1481 nm and 1474 nm consequently, sharp DFG peak is observed near at 1 THz, 2 THz, 3 THz, 4 THz, 5 THz, 6 THz, 7 THz, 8 THz, 9 THz and 10 THz respectively in power spectra at the receiver waveguide. (b) Showing electric field distribution in the THz ring resonator for 5 THz. At this frequency, we observe whispering gallery mode resonance that is why electric field is confined to the outer boundary of the ring resonator.

3.2.4 Analytical Model for Output THz Estimation

Difference frequency generation (DFG) is a second order nonlinear optical process which generates an electromagnetic wave of frequency ω_3 when two optical beams at slightly different frequencies ω_1 and ω_2 are incident upon a nonlinear material, such that the output frequency is the difference between the two input frequencies: $\omega_3 = \omega_1 - \omega_2$. Let us assume that a strong undepleted pump optical wave $E^1(z,t)$ and an idler optical wave of $E^2(z,t)$

41

with amplitudes $E_{\omega 1}$ and $E_{\omega 2}$ are propagating along with the generated THz field of $E^3(z,t)$ in z direction of the nonlinear medium [5],

$$E^1(z,t) = \frac{1}{2}[E_{\omega 1}(z)e^{i(k_1 z - \omega_1 t)} + c.c.],$$

$$E^2(z,t) = \frac{1}{2}[E_{\omega 2}(z)e^{i(k_2 z - \omega_2 t)} + c.c.], \qquad (3.5)$$

$$E^3(z,t) = \frac{1}{2}[E_{\omega 3}(z)e^{i(k_3 z - \omega_3 t)} + c.c.]$$

where, $k_1 = \dfrac{\omega_1 n_{o1}}{c}, k_2 = \dfrac{\omega_2 n_{o2}}{c}, k_3 = \dfrac{\omega_3 n_3}{c}$ and $c.c.$ stands for complex conjugate; n_{o1}, n_{o2} and

n_3 are the effective mode indices for two optical beams and generated THz wave respectively. Second order nonlinear polarization is characterized by [6],

$$P_{NL}^i = \varepsilon_0 \chi^{(2)} \sum_{j,k=1,2,3} \delta_{ijk} E_j E_k \qquad (3.6)$$

where, $\delta_{123} = 1$, δ_{ijk} is symmetric under all permutations of its indices and vanishes unless (ijk) are all distinct. Corresponding nonlinear polarization with the frequencies ω_1, ω_2 and ω_3 are

$$P_{NL}^1(z,t) = \varepsilon_0 \chi^{(2)}[2E_{\omega 2}E_{\omega 3}e^{i\{(k_2+k_3)z - \omega_1 t\}} + c.c.],$$

$$P_{NL}^2(z,t) = \varepsilon_0 \chi^{(2)}[2E_{\omega 1}E_{\omega 3}^* e^{i\{(k_1-k_3)z - \omega_2 t\}} + c.c.], \qquad (3.7)$$

$$P_{NL}^3(z,t) = \varepsilon_0 \chi^{(2)}[2E_{\omega 1}E_{\omega 2}^* e^{i\{(k_1-k_2)z - \omega_3 t\}} + c.c.],$$

Now nonlinear polarization $P_{NL}^3(z,t)$ acts as a source for the propagation of THz field $E^3(z,t)$ in the z direction. So the governing wave equation is,

$$\frac{\partial^2 E^3(z,t)}{\partial z^2} - \frac{n_3^2}{c^2}\frac{\partial^2 E^3(z,t)}{\partial t^2} = \frac{1}{\varepsilon_0 c^2}\frac{\partial^2 P_{NL}^3(z,t)}{\partial t^2} \tag{3.8}$$

By substituting equation (3.5) and (3.7) into the wave equation (3.8), we obtain

$$\frac{d^2 E_{\omega 3}(z)}{dz^2} + 2ik_3 \frac{dE_{\omega 3}(z)}{dz} = -\frac{\chi^{(2)}\omega_3^2}{2c^2}\left[2E_{\omega 1}E_{\omega 2}^* e^{i(k_1-k_2-k_3)z}\right] \tag{3.9}$$

Invoking the slowly varying envelope approximation [27], where the first term in equation (3.9) can be neglected since THz field amplitude $E_{\omega 3}$ does not change appreciably for the propagation distance of a wavelength, the wave equation is reduced to

$$\frac{dE_{\omega 3}(z)}{dz} = iG_{\omega 3}E_{\omega 1}E_{\omega 2}^* e^{i\Delta kz}; G_{\omega 3} = \frac{\omega_3 \chi^{(2)}}{2cn_3} \tag{3.10}$$

where, $\Delta k = k_1 - k_2 - k_3$ is the momentum mismatch. The amplitudes of the optical waves also vary slowly in the propagating direction and obey the similar wave equations,

$$\frac{dE_{\omega 1}(z)}{dz} = iG_{\omega 1}E_{\omega 2}E_{\omega 3}e^{-i\Delta kz}; G_{\omega 1} = \frac{\omega_1 \chi^{(2)}}{2cn_{o1}} \tag{3.11}$$

$$\frac{dE_{\omega 2}(z)}{dz} = iG_{\omega 2}E_{\omega 1}E_{\omega 3}^* e^{i\Delta kz}; G_{\omega 2} = \frac{\omega_2 \chi^{(2)}}{2cn_{o2}} \tag{3.12}$$

We solve these equations to find the THz field variation over distance z by assuming the phase matching condition holds, therefore, $\Delta k = 0$ and pump wave field $E_{\omega 1}$ is undepleted. The amplified idler wave field and the DFG THz field can be written as,

$$E_{\omega 2}(z) = E_{\omega 20}\cosh gz \tag{3.13}$$

43

$$E_{\omega 3}(z) = i \sqrt{\frac{\omega_3 n_{o2}}{\omega_2 n_3}} E_{\omega 20} \sinh gz \qquad (3.14)$$

where $g = \sqrt{G_{\omega 3} G_{\omega 2}} E_{\omega 1}$ and $E_{\omega 20}$ is the electric field of idler wave at $z = 0$.

The THz field described in equation (3.14) is generated in the high Q optical ring resonator due to the interaction of two input infrared optical pump and idler waves carried in by the input waveguides placed at two sides of the nonlinear ring. We assume half circumference of the ring (C/2) to be the maximum travelled distance where two input waves interact with the nonlinear material resulting in THz generation without being changed due to out-coupling to the straight bus waveguides. This generated THz couples to the THz ring resonator where it is well confined with resonant mode. Then THz wave out-couples to the THz straight receiver waveguides placed at close proximity to the resonator. THz field at the receiver waveguide can be written as [1],

$$E_d = -i\sqrt{a}\kappa \sqrt{\frac{\omega_3 n_{o2}}{\omega_2 n_3}} E_{r20} \sinh \frac{gC}{2} \qquad (3.15)$$

where a and κ are the total round trip attenuation and power coupling coefficient in the ring resonator and E_{r20} is the initial electric field of idler wave in the ring resonator. If the area of the THz mode at the receiver waveguide is A and n_{eff} is the effective mode index for the generated THz wave in the waveguide, then THz output power at the receiver waveguide can be estimated by the following formula,

$$P_{out} = \frac{n_{eff}}{2} \varepsilon_0 c |E_d|^2 \cdot A \qquad (3.16)$$

We estimated the THz output power of the proposed device analytically by employing the above-mentioned analytical model that we developed. Both optical beams are assumed to be at a power level of 0.5 W in the input bus waveguides. Some commercially available popular nonlinear materials and polymers such as aluminum nitride, potassium titanyl phosphate (KTP), GaSe and SEO100 polymer from Soluxra company with $\chi^{(2)}$ value of 5 pm/V, 27.4 pm/V, 108 pm/V and 500 pm/V respectively were used in the calculation. The THz output power of the device was estimated at 1 THz by considering the attenuation coefficient of 0.55 m^{-1} for high resistivity Si at 1 THz. For the analytical estimation, we used values of round trip attenuation and coupling coefficient to be 0.99 and 0.02 that we found while designing the ring resonator. We calculated THz output power at the receiver waveguide to be 2.2 µW, 66 µW, 1 mW and 27 mW, respectively for those same nonlinear materials employing equation (3.16). By considering the cross-sectional area of the THz receiver waveguide, output intensity at 1 THz was estimated to be 92 W/m^2, 2.75 kW/m^2, 43 kW/m^2 and 1.1 MW/m^2 respectively for those materials.

3.2.5   Fabrication Efforts and Problems Faced

The proposed microring resonators based THz emitter devices can be fabricated using standard nanofabrication tools and techniques. An undoped high resistivity (HR) Si wafer anodic-bonded to a borosilicate substrate is thinned to the thickness of the designed THz HR Si waveguide, 120 µm, and afterwards 1 µm SiO$_2$ layer is grown on top of Si using the plasma-enhanced chemical vapor deposition (PECVD) to make the insulation layer

between optical and THz resonators. Optical nonlinear layer either could be sputtered for the AlN case or spun-cast for the polymer case. Finally, electron-beam lithography (EBL) and deep reactive ion etching (DRIE) can be used to construct the optical and THz microring resonators including input and output straight bus waveguides. The proposed process flow for fabrication is summarized in Fig. 3.7.
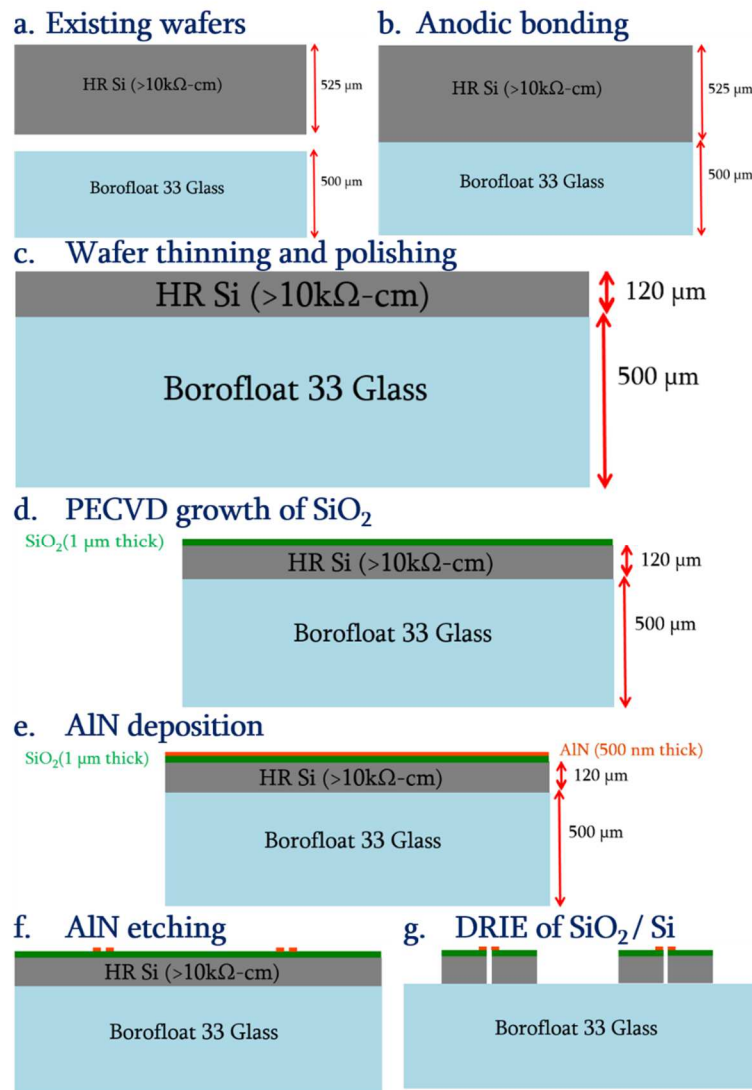
Figure 3.7 | Proposed fabrication process flow of THz emitters. (a) Existing wafers. (b) Anodic bonding. (c) Wafer thinning to 120 μm and polishing. (d) 1 μm thick PECVD growth of SiO_2. (e) 500 nm thick AlN deposition. (f) AlN etching. (g) DRIE of SiO_2/Si.

We started the fabrication of the first batch of prototypes by considering AlN as nonlinear material due to its easy processing and being readily available. Here, 500 nm thin film of AlN is deposited on top of PECVD grown SiO_2 layer of the pre-processed bonded wafer with atomic layer deposition (ALD) technique. We worked over a year on the optimization of the process recipes for AlN etching and deep reactive ion etching (DRIE) of high resistivity (HR) Si. Unfortunately, due to the very small gap between the optical or THz ring resonators and their respective straight waveguides compared to the thicknesses of those waveguides, we could not reach to our required features. We came to a understanding that it will require more process developments to reach to our requirement of high etching aspect ratio, which we could not pursue any longer due to financial budget limitation. Here, we will briefly summarize the findings of our fabrication efforts and also the proposed solution to the problems faced at each step.

For AlN etching process developments, we divided the work into three sections – mask fabrication, lithography to pattern and finally etching. With the help of stepper we prepared our mask. After the fabrication of mask, we found out that the test mask came out over biased. For instance, we designed the mask for ring resonator with 600 nm width and 500 nm gap, instead it came out with 682 nm width and 417 nm gap, which was almost 100 nm over biased (see Fig. 3.8b). In mask fabrication, the critical dimension was very difficult to control mainly due to two reasons: chromium etch rate and undercut was not constant for all the features and also it was shifting the feature size depending the area of the nearby exposed patterns (see Fig. 3.8c). Therefore, the proposed solution to these

problem is either we need to change our layout design file accordingly to compensate the bias or we outsource to fabricate this mask from a company with exact features we require.
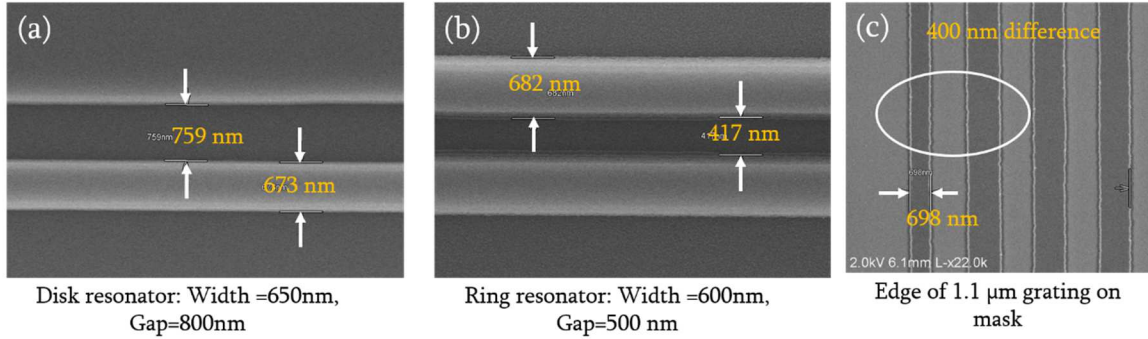
Figure 3.8 | SEM images of the fabricated test mask for AlN etching. (a) Disk resonator. (b) Ring resonator. (c) Tapered input grating.

In the lithography step, we used SPR 955-0.9 photoresist with 3000 rpm speed to get 970 nm thick photoresist on AlN/SiO$_2$/Si chip. We used 1:1 (DI : Microposit) developer because it attacks AlN far slower than the TMAH (Tetramethylammonium hydroxide) based developers (e.g. AZ 726MIF) do. However, this chosen developer has poor selectivity to unexposed photoresist compared to TMAH based developers and also the developing rate varies significantly with age. First, we used Si chip to transfer the pattern with 0.27s exposure dose and the pattern came out precise with vertical sidewall as requires (see Fig. 3.9a). Then we used our AlN/SiO$_2$/Si chip to transfer the patterns, but in this case it came out with non-vertical sidewall, which was unexpected (see Fig. 3.9b and Fig. 3.10). We figured out that the focus shift due to AlN film stress makes this difficult to achieve required features on AlN samples, which will likely be worse for bonded samples with borosilicate. In Fig. 3.10, it is seen that in the same die we got different dimensions in the

center than in the edge due to the focus shift. Small die area helped to reduce the focus shift, but even 1 μm die caused variation. The AlN film stress was caused by the deposition technique and can be controlled if used suitable technique to achieved required properties.

0.27 sec exposure on Si
2 μm grating pattern

0.27 sec exposure on AlN
2 μm grating pattern
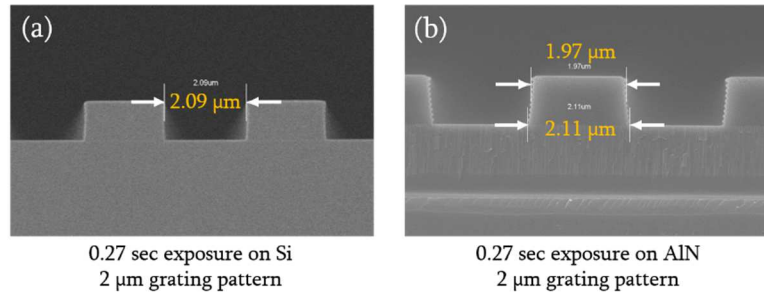
Figure 3.9 | SEM images of the patterned photoresist on Si and AlN chips. (a) Si sample came out with vertical sidewall. (b) AlN chip gave non-vertical sidewall.

0.29 sec exposure
0.6 μm grating near die center

0.29 sec exposure
0.6 μm grating near die edge

500 nm grating: near die center
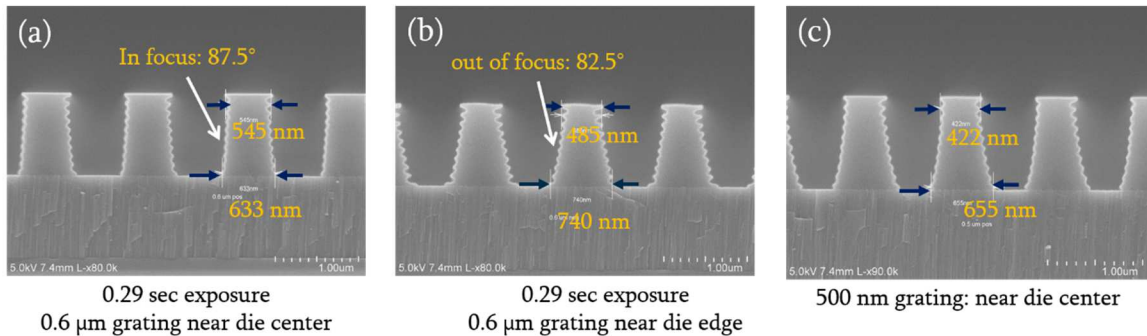
Figure 3.10 | SEM images in different area of the patterned photoresist on AlN samples. (a) In focus in the die center still gave 87.5° sidewall. (b) Out of focus in the edge of the die with sidewall degradation. (c) Die center in a different grating with poor sidewall.

In order to achieve AlN thin films with very high quality and excellent surface morphology, radio frequency (RF) magnetron reactive sputtering is considered preferable compared to other available deposition techniques [7]. Also, sputtered AlN thin films are proven to be realized as excellent candidates for integrated optics for a variety of features

49

[8]. First, with optimized process settings, the sputter-deposited AlN thin films feature a columnar micrograin structure with highly c-axis orientation ([0002] direction) normal to the film plane, which is extremely preferred and essential for exploitation of the largest component of AlN's $\chi^{(2)}$ tensor (d_{33}) in order to explore the fullest potential of nonlinear phenomena observed in AlN. Second, unlike other nitride deposition, AlN can be sputtered with very low process pressures, which allow to achieve micrometer thick films ensuring the fabrication of AlN waveguides with highly confined optical modes. Third, AlN sputtering process is thermally compatible with critical CMOS processes, since the equilibrium wafer temperature does not exceed 350 °C while sputtering. Finally, AlN can be sputter-deposited with excellent surface smoothness on a variety of crystalline and amorphous CMOS materials, such as, Si, SiO_2, Si_3N_4 and even metals.

With the transferred photoresist patterns, trial etching was performed using inductively coupled plasma (ICP) reactive ion etching (RIE) in Cl_2/BCl_3/Ar atmospheric conditions. We tried different power settings and gas flow combinations and found two relatively better recipes (see Fig. 3.11). Cross-sectional SEM images of AlN etching trials are shown in Fig. 3.11. Both the recipes gave non-vertical sidewall (64.7° for recipe 1 and 68.4° for recipe 2) and we could not achieve the desired features due to poor selectivity (effective selectivity of 0.32:1 with recipe 1 and selectivity of 0.34:1 with recipe 2) of the photoresist and heavy resist erosion. Once the erosion reaches the film surface, the features widen considerably. The poor selectivity is a very common problem with AlN etching. Also the heavy resist erosion was observed due to enhanced resist etch rate at the optimal sputter angle. One of the other possible reasons might be thicker photoresist, which makes

lithography challenging suggesting thinner AlN would be feasible. We came to understanding that either we need to change our design to have around 300 nm thickness of AlN instead of 500 nm, or we can try different photoresist other than SPR 955-0.9. Also in order to improve selectivity, we can use a hard oxide mask instead of photoresist, in that case the selectivity will be very high around 5:1. The oxide mask would allow to use AZ 726MIF developer, which is more repeatable and better characterized.
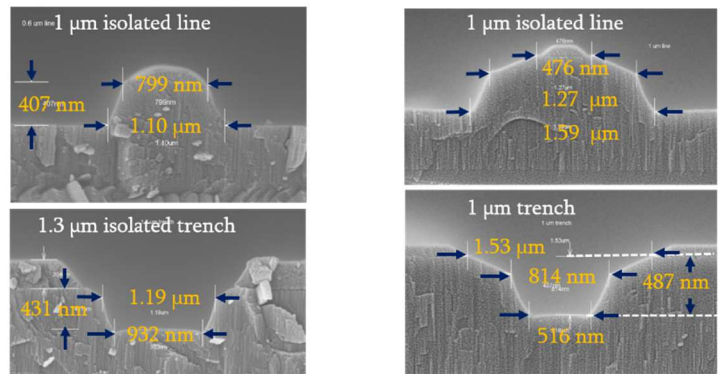
Figure 3.11 | Cross-section SEM images for AlN etching results with two different recipes. Both the recipes provided poor vertical sidewall ~65° due to poor selectivity.

Deep reactive ion etching (DRIE) technique was adopted to achieve the required high aspect ratio etching of high resistivity (HR) Si to fabricate THz resonators. The etching aspect ratio we targeted was around 200:1 (600 nm gap and 120μm deep etch). After having different trials, we found two relatively better recipes with aspect ratio of approximately 50:1 as shown in Fig. 3.12. Therefore, in order to reach the required features,

it demands significant recipe developments, which we could not pursue any longer due to financial budget limitation.
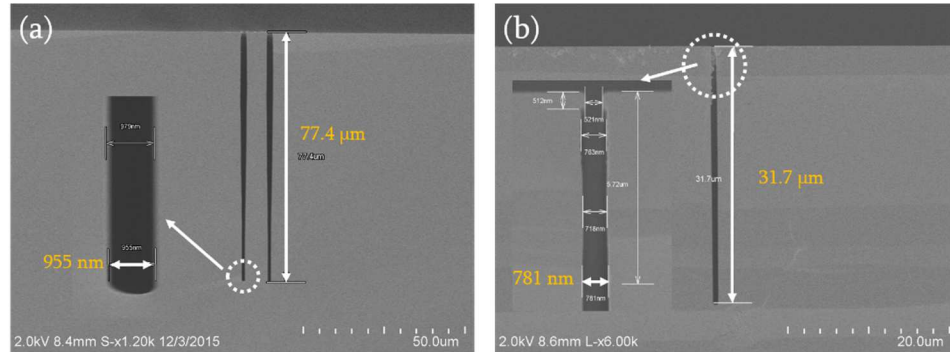
Figure 3.12 | Cross-section SEM images for DRIE of HR Si samples. We achieved successful etching with the aspect ratio of around 50:1.

3.3   Summary

In summary, we have proposed and systematically investigated a novel tunable, compact room temperature terahertz (THz) source based on difference frequency generation in a hybrid optical and THz micro-ring resonator. We described detailed design steps of the source capable of generating THz wave in 0.5–10 THz with a tunability resolution of 0.05 THz by using high second order optical susceptibility ($\chi^{(2)}$) in crystals and polymers. The phase matching condition was successfully satisfied for the first time across 0.5-10 THz DFG range in single geometry device by engineering both the optical and THz resonators with appropriate effective indices. We have also successfully developed an analytical model estimating THz output power of the device by using practical values of susceptibility in available crystals and polymers. The proposed source can enable tunable, compact THz

emitters, on-chip integrated spectrometers, inspire a broader use of THz sources and motivate many important potential THz applications in different fields.

3.4 References

1. Bogaerts, W., De Heyn, P., Van Vaerenbergh, T., De Vos, K., Kumar Selvaraja, S., Claes, T., Dumon, P., Bienstman, P., Van Thourhout, D., & Baets, R. (2012). Silicon microring resonators. Laser & Photonics Reviews, 6(1), 47-73.

2. Xiao, S., Khan, M. H., Shen, H., & Qi, M. (2007). Modeling and measurement of losses in silicon-on-insulator resonators and bends. Optics Express, 15(17), 10553-10561.

3. Almeida, V. R., Barrios, C. A., Panepucci, R. R., & Lipson, M. (2004). All-optical control of light on a silicon chip. Nature, 431(7012), 1081-1084.

4. Hochberg, M., Baehr-Jones, T., Wang, G., Shearn, M., Harvard, K., Luo, J., Chen, B., Shi, Z., Lawson, R., Sullivan, P., & Jen, A. K. (2006). Terahertz all-optical modulation in a silicon–polymer hybrid system. Nature materials, 5(9), 703-709.

5. Lee, Y. S. (2009). Principles of terahertz science and technology (Vol. 170). Springer Science & Business Media.

6. Yang, Z., Chak, P., Bristow, A. D., van Driel, H. M., Iyer, R., Aitchison, J. S., Smirl, A.L., & Sipe, J. E. (2007). Enhanced second-harmonic generation in AlGaAs microring resonators. Optics letters, 32(7), 826-828.

7. Lin, C. M., Lien, W. C., Felmetsger, V. V., Hopcroft, M. A., Senesky, D. G., & Pisano, A. P. (2010). AlN thin films grown on epitaxial 3C–SiC (100) for piezoelectric resonant devices. Applied Physics Letters, 97(14), 141907.

8. Xiong, C., Pernice, W. H., & Tang, H. X. (2012). Low-loss, silicon integrated, aluminum nitride photonic circuits and their use for electro-optic signal processing. Nano letters, 12(7), 3562-3568.

CHAPTER 4

Tunable Room Temperature CMOS-Compatible THz Emitters based on Nonlinear Mixing in Microdisk Resonators

4.1   Proposed Device

A novel tunable, compact, room temperature THz emitter has been proposed which radiates in 0.5-10 THz range with tuning frequency resolution of 0.05 THz. Figure 4.1 presents schematic of the source device in three dimensional and cross-sectional view. The top orange colored microdisk resonator with outer radius and thickness of 390 µm and 0.5 µm respectively is made of a second order nonlinear material such as aluminum nitride or lithium niobate or any similar materials or polymers with $\chi^{(2)}$ value. A straight bus waveguide with 0.65 µm wide and 0.5 µm thick is placed adjacent to nonlinear disk in order to carry in the required two near-infrared input pump and idler optical waves. The input beams carried by fibers can be coupled into the straight waveguides using grating couplers or tapered inlet waveguides. Critical coupling is achieved at the gap distance of 550 nm between the microdisk resonator and straight waveguide. Another disk resonator made of high resistivity (HR) Si with 120 µm thickness is provided underneath the optical disk resonator with an isolation layer in order to support the DFG THz. The insulation layer is made of SiO_2 with 1 µm thickness. A straight THz waveguide of 180 µm wide and 120 µm thick is placed underneath the input bus waveguide to out-couple the THz beam from the cavity and guide it to any point of interest. Due to the large quality factor ($Q \sim 10^6$) of the proposed microdisk resonators to ensure large energy built-up inside the cavity, the coupling efficiency of generated THz wave from microdisk resonator to the receiver straight THz waveguide is found to be 10%.
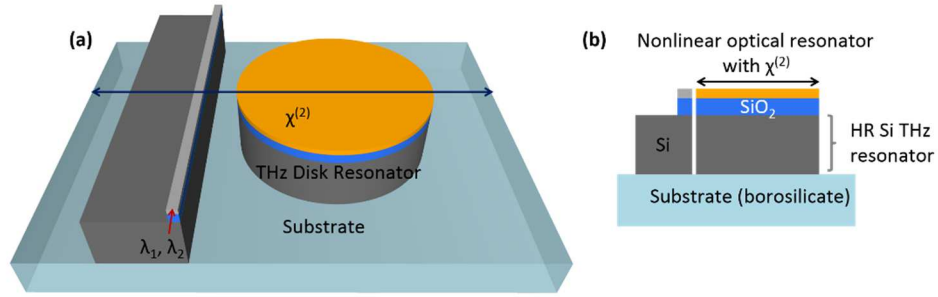
Figure 4.1 | Schematic of the proposed device. (a) 3D structure of the proposed THz emitter consisting of nonlinear and THz microdisk resonator. (b) Cross-sectional view of the emitter.

4.2   Results and Discussion

The complete design steps of the device are presented here in detail satisfying phase matching condition for DFG. Then the concept of device operation is validated with a full scale 3D simulation of a smaller version of the proposed device. Afterwards we simulate the actual device to find DFG in the desired range and calculate power-normalized optical to THz conversion efficiency as well. We also developed an analytical model to estimate THz output power from the source device. Finally, we compared the performance of this THz emitter against the one designed with micro-ring resonators.

4.2.1   Design of Microdisk Resonators

Microdisk resonators with whispering gallery resonant modes exhibit tunability, narrow resonance linewidths and extraordinary optical field intensities that originally led to their use in integrated photonics applications as one of the most significant building blocks. If the round trip of a light wave inside the disk is equal to an integer number of wavelengths,

M, it couples into the resonator in phase with itself, which is known as the resonance condition. If *M*, λ_M, n_{eff} and *R* be the azimuthal mode number, corresponding resonant wavelength, effective index of the respective mode and radius of the disk, then resonance condition is defined by the following relation [1],

$$M \lambda_M = 2\pi R n_{eff} \qquad (4.1)$$

In order to design any disk resonator free spectral range (FSR) is considered to be an important parameter, which is defined by the separation between two consecutive whispering gallery mode resonant frequencies. A smaller FSR ensures a larger number of resonant peaks in a particular frequency range resulting in a higher tunability resolution in the disk. FSR and radius of the disk resonator is inversely related by [1],

$$FSR = c / (2\pi R n_g) \qquad (4.2)$$

where n_g is the group index in the disk resonator and *c* is the speed of light in free space. Here we present detailed step by step design processes for microdisk resonators based THz source with tunability resolution of 0.05 THz in 0.5-10 THz range. First step is to design the nonlinear optical disk resonator. For the proposed device, tunability resolution is defined by the FSR of the nonlinear disk. Hence FSR is set to 0.05 THz. According to Eq. (4.2), radius of the disk can be calculated if we get to find group index of the resonant optical modes in the disk. Dispersion of the resonant modes in the disk is taken into account while estimating group index which is defined by the following equation [2],

$$n_g = n_{eff} - \lambda_M \frac{dn_{eff}}{d\lambda} \qquad (4.3)$$

56

The microdisk resonators have multiple sets of resonances with fundamental and higher order radial modes. For a fixed radius of the microdisk resonator, higher order radial resonant modes exhibit a larger FSR compared to the fundamental radial mode [3]. Therefore, the fundamental radial mode of microdisk is chosen in order to minimize the radius of the disk ensuring a smaller FSR between the resonant modes. Hence, effective indices of the first order radial whispering gallery modes (WGM) are numerically investigated in the nonlinear optical microdisk resonator [1]. Refractive index of aluminum nitride, which is 2.12 at 1550 nm, is considered in the simulation. By keeping the radius unchanged, effective mode indices in the disk are simulated for three different thicknesses of 0.4 μm, 0.5 μm and 0.6 μm. Figure 4.2 shows the simulation results of dispersion characteristics in the disk for the infrared input optical waves with wavelengths from 1470-1550 nm. It is evident from the figure that effective indices of WGMs in the microdisk decrease with increasing wavelength and decreasing thickness. The group indices are calculated to be 2.41, 2.45 and 2.39 for the disk thicknesses of 0.4 μm, 0.5 μm and 0.6 μm respectively. The 0.5 μm thick optical microdisk resonator is chosen finally due to its larger group index, which results in smaller radius for the disk. The outer radius of the nonlinear optical resonator is estimated to be 390 µm by putting the values of group index and FSR into Eq. (4.2). The azimuthal mode number, *M*, of whispering gallery resonant modes for a certain wavelength in a microdisk resonator can be estimated numerically [1]. Figure 4.3 shows the mode number with respect to the corresponding resonant wavelength for the designed nonlinear optical microdisk with 390 μm radius and 0.5 μm thickness. The distance between the two consecutive resonant modes is found to be 0.4 nm, which corresponds to FSR of 0.05 THz proving the accuracy of the design.
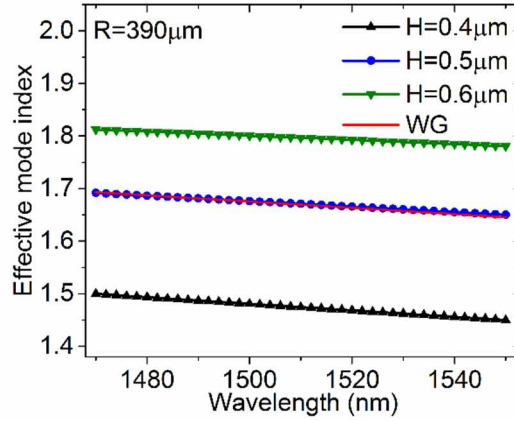
Figure 4.2 | Dispersion of microdisk resonators. Simulated effective indices of first order radial whispering gallery resonant modes for three different thicknesses (H=0.4 μm, 0.5 μm and .06 μm) of nonlinear optical microdisk with radius of 390 μm. The effective index of the fundamental mode of input bus straight waveguide (WG) with 0.65 μm width and 0.5 μm thickness is also shown. Effective mode indices of this waveguide closely match with the indices of 0.5 μm thick microdisk resonator.

Whispering gallery resonant modes are excited in the microdisk resonator by the infrared waves propagating in the input bus straight waveguides. The fundamental and higher order radial resonances are possible in the disk due to the absence of the inner cylindrical boundary. A desired order radial mode of resonances can be excited efficiently in the microdisk only if the index matching between the radial mode and the bus waveguide mode is achieved [3, 4]. Therefore, the straight bus waveguide needs to be engineered to match its effective index with desired order cavity mode. Hence, fundamental mode effective indices in the input waveguide are investigated by varying its width while keeping the height fixed at 0.5 µm. For the 0.65 µm waveguide width, a close index match is found between the waveguide mode and the fundamental radial mode in the designed microdisk resonator with 390 µm radius and 0.5 µm thickness, which is shown in Fig. 4.2. Hence,

58

input bus waveguide with 0.65 µm width and 0.5 µm thickness is chosen for the proposed device.
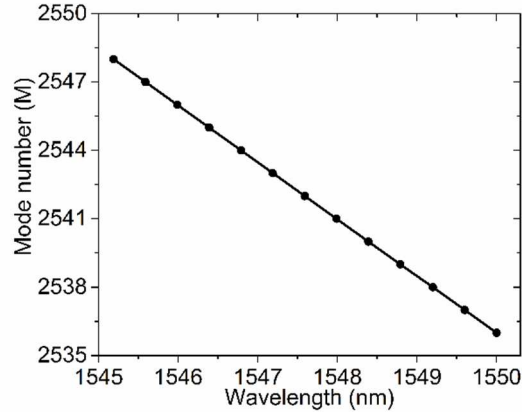
Figure 4.3 | Excited resonant modes inside microdisk resonator. Azimuthal mode number with respect to first order radial WGM resonant wavelength in the designed nonlinear optical disk resonator of 390 µm radius.

Critical coupling condition is a fundamental property of resonators coupled to straight waveguides [5]. The resonator is considered to be critically coupled only when internal resonator loss is equal to the coupling loss. In that case at resonant frequencies, zero transmission occurs in the input straight bus waveguide due to the fact that round trip amplitude transmission τ becomes equal to the direct transmission coefficient r [5-7]. Maintaining critical coupling over 1474-1550 nm infrared optical waves in the nonlinear disk is necessary in order to achieve efficient DFG in 0.5-10 THz range. For this infrared band, value of amplitude transmission is numerically simulated and found to be 0.995 in the designed nonlinear disk resonator. Compared to the micro-ring resonator of same dimension, the amplitude transmission is higher in the disk resonator, mainly due to the absence of the inner cylindrical boundary [8]. The disk geometry permits the supported

mode to reside closer to the resonator center and decrease the radiation losses. Critical coupling is achieved at the gap distance of 550 nm between the disk resonator and bus waveguide at which coupling coefficient κ reaches to 0.1 satisfying $\tau = r$. We find the field amplitude enhancement inside the disk to be 10.025 employing Eq. (4.5) mentioned in the analytical model section.

Phase matching condition (PMC) must be met for efficient DFG operation. In this case, THz waves get coherently amplified while co-propagating with the input infrared optical waves. This condition can be defined by the following relation,

$$n_T \omega_T = n_1 \omega_1 - n_2 \omega_2 \tag{4.4}$$

where n_T, n_1 and n_2 are the effective mode indices at ω_T, ω_1 and ω_2 frequencies respectively. Modal phase matching technique has been adopted here in which effective mode indices of three interacting waves involving DFG phenomenon must satisfy Eq. (4.4). By applying the fundamental WGM effective indices of the input infrared waves observed in the designed nonlinear disk resonator into Eq. (4.4), it is found that effective indices of THz waves are required to be around the value of 2.46 in order to satisfy PMC for DFG in 0.5-10 THz range. Therefore, THz microdisk resonator must be engineered to support the resonant WGM indices at THz frequencies of interest with the effective indices around 2.46. High resistivity (HR) Si is chosen to guide THz radiation due to its transparency in much of the THz range and high refractive index which facilitates to concentrate THz waves in much smaller sizes than that of ordinary optical fibers [9-11]. It also makes the proposed THz emitter compatible with Si-CMOS technology.

Dispersion of first order radial THz WGM indices is investigated in HR Si microdisk resonator with varied thicknesses while keeping the radius unchanged at 390 μm. For the simulation of HR Si microdisk resonator, a fixed refractive index of 3.42 is considered because it remains almost same over the THz region of interest. Figure 4.4 shows the simulated results of effective indices for the disk thicknesses of 110 μm, 120 μm and 130 μm. Also shown the required effective indices which will satisfy phase matching condition over the whole 0.5-10 THz frequency range.
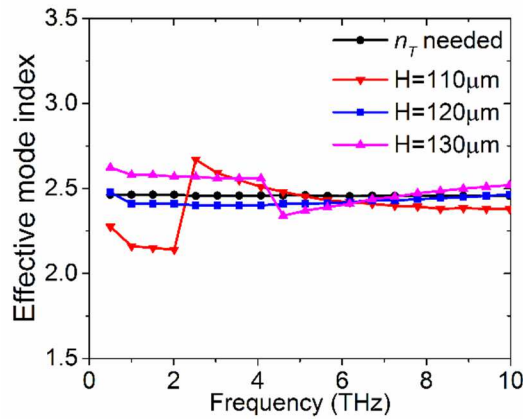
Fig. 4.4 | Dispersion of THz microdisk resonators. Dispersion of first order radial resonant mode in THz HR Si microdisk resonator with radius 390 μm for different thicknesses (H=110 μm, 120 μm and 130 μm).

As seen, effective indices with 120 μm thick microdisk resonator provide the closest match against required indices over the entire THz frequency range of interest. Therefore, THz microdisk resonator with 120 μm thickness and same outer radius of 390 μm is chosen and placed underneath the nonlinear disk to support the DFG THz radiation. With the help of eigenmode solver in finite element method (FEM) based simulation tool, we simulated the THz wave modal profiles in the HR Si THz microdisk resonator to show

61

the WGM resonances with the required mode indices [12]. Fig. 4.5 shows the modal profiles in the THz disk resonator for 0.5, 0.6, 0.8 and 1 THz.
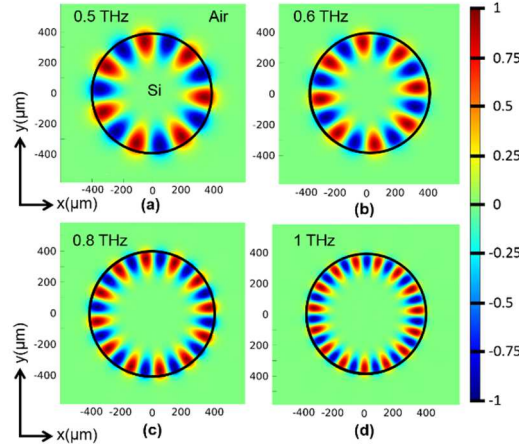
Figure 4.5 | Resonant THz modal profiles inside the disk. First order radial whispering gallery resonant modes in HR Si THz microdisk resonator with appropriate effective indices satisfying phase matching condition.

4.2.2 Numerical Simulations by FDTD and FEM

In the proposed device, we expect the DFG THz in the top nonlinear disk to couple into the THz disk resonator which is especially designed to support THz radiation with resonant WGM indices satisfying phase matching condition. From where it will out-couple to the output receiver straight THz waveguide. Due to the large physical dimension of the designed emitter for DFG in 0.5-10 THz range and vast difference between the wavelength corresponding to the input and generated waves, a smaller version of the source device is designed and simulated in 3D with commercially available simulation tool based on FDTD and after that the extracted simulation results are analyzed to prove the concept [13]. Then

it is converted into a 2D model in order to investigate THz generation in the proposed device with better computational efficiency.

First we performed 3D simulation on a smaller source device which was designed to support 30 THz DFG, where nonlinear optical disk was of 6.5 µm radius and 0.5 µm thickness with input bus waveguide of 0.65 µm width and 0.5 µm thickness. Critical coupling was achieved when the gap between the bus waveguide and disk was kept at 500 nm. Underneath, a THz disk resonator of same radius with 2 µm thickness and THz straight waveguides of 3 µm width and 2 µm thickness were added with a SiO_2 insulation layer of 0.25 µm thickness. The nonlinearity $\chi^{(2)}$ was set to 100 pm/V in the top nonlinear disk. Two infrared pump and idler waves at 1550 nm and 1342 nm were excited in the input bus waveguides with 0.2 THz bandwidth and power level at 1 W each. According to the DFG theory, these two input waves should produce DFG at 30 THz. Simulation results obtained from this device are presented in Figure 4.6. Power spectrum shown in Fig. 4.6(b) was taken at the output straight THz waveguide which clearly confirms the generated peak at 30 THz with linewidth of 0.4 THz. Then we monitored the electric field at 30 THz on plane A (see Fig. 4.6(a)), which is presented in Fig. 4.6(d). The field profile clearly shows first order radial WGM resonance, as expected. Then we observe electric field at 30 THz on plane B (see Fig. 4.6c), which is presented in Fig. 4.6(e). It is clearly evident that THz generated in the nonlinear disk is coupling to the HR Si disk provided underneath and also it is out-coupling to the output straight THz waveguide, as expected. Since 30 THz DFG having smaller wavelength couples from the nonlinear disk to HR Si disk through the oxide layer, it is expected that in the proposed device DFG in 0.5-10 THz range having larger

wavelengths should easily couple to the THz disk provided underneath. With the same input parameters, this geometry is simulated in 2D using the same simulation tool considering only the top nonlinear disk resonator with straight waveguide. The same output characteristics are found after the simulation, which validates the accuracy of the 2D simulations.

In the simulation of the proposed THz emitter device, we kept the idler optical beam fixed at 1550 nm and set the pump beam varying between 1546-1474 nm at approximately 0.4 nm interval satisfying WGM resonance condition of the nonlinear disk resonator, to obtain THz radiation in 0.5-10 THz range with a tuning frequency resolution of 0.05 THz. This resolution is limited by the FSR of the disk and could be improved by designing a disk with a larger radius following the Eq. (4.2). The proposed actual device was simulated in 2D using the same FDTD tool in order to prove the DFG in the desired THz range. We set the $\chi^{(2)}$ value at 100 pm/V and input infrared power level at 1W each with 0.01 THz bandwidth. Then pump wave was varied and set at ten different position between 1546 nm to 1474 nm while keeping the idler at 1550 nm in the bus waveguide. The power spectra recorded at the end of the receiver straight waveguide from those simulations are presented in Fig. 4.7(a). Sharp DFG peaks are observed at the exact THz frequencies in 0.5-10 THz range that we expected from the chosen input waves according to DFG theory. The linewidth of the generated THz wave is found to be 0.02 THz, which is dictated by the bandwidth of the input infrared optical waves. It is possible to achieve sharper linewidth by reducing the input waves' linewidth.
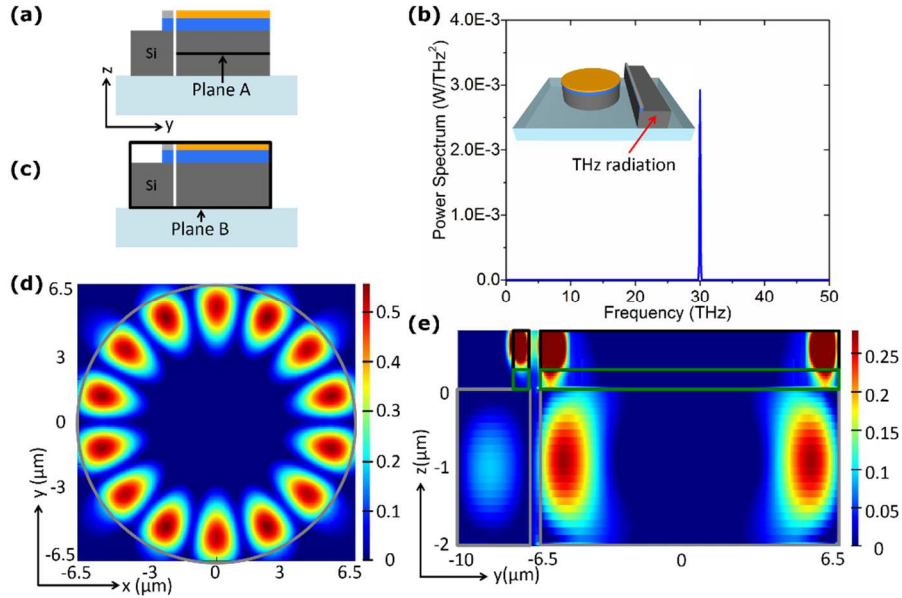
Figure 4.6 | 3D simulations performed on a smaller DFG emitter. Full 3D simulation results of a 6.5 µm radius emitter with two infrared input beams excited at 1550 nm and 1342 nm. (a) Cross-section of the emitter indicating plane A inside the THz disk resonator in order to record WGM THz resonances. (b) Power spectrum at the end of the receiver THz straight waveguide, which shows a sharp DFG peak at 30 THz confirming DFG theory. (c) Cross-section of emitter indicating plane B. (d) Showing first order radial WGM resonance at 30 THz recorded on plane A inside the HR Si disk resonator (e) Electric field profile at 30 THz on plane B.
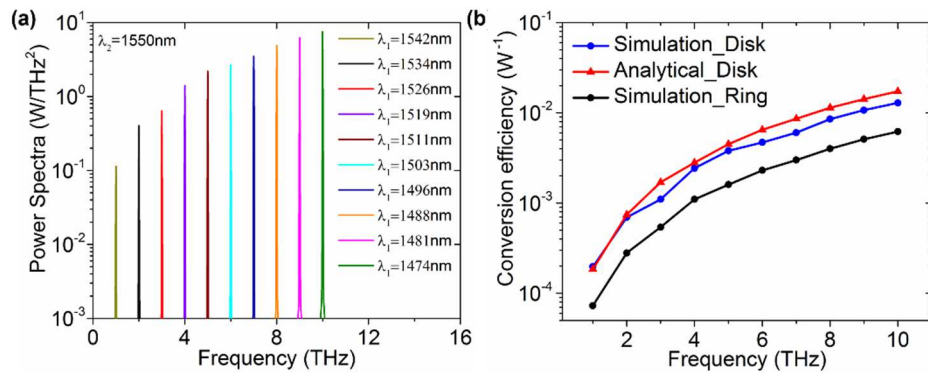
Figure 4.7. | Simulation results of the proposed THz emitter. (a) Power spectra with DFG peaks in 0.5-10 THz range in the proposed THz emitter with 390 µm radius disk resonators. Output THz power was collected at the end of the receiver straight waveguide. (b) Power-normalized optical to THz conversion efficiency for both the microdisk and microring resonators based THz emitters.

65

4.2.3 Analytical Model for Output THz Estimation

Difference-frequency generation (DFG) involves the interaction of two near-infrared optical waves at ω_1 and ω_2 in a nonlinear material and generates an electromagnetic wave at ω_T which is the exact difference between two input frequencies [14]. Let us assume that a pump optical wave and an idler optical wave with amplitudes E_{1b} and E_{2b} are excited in the input bus waveguides (see Fig. 4.1(a)). Therefore, inside the cavity disk resonator the enhanced input wave fields can be described as [6],

$$E_{1,2c} = BE_{1,2b}; B = \kappa / (1 - r\tau) \tag{4.5}$$

where, B is the field enhancement factor inside the disk resonator, r is the transmission coefficient in the bus waveguide and κ, τ are the coupling coefficient and round trip amplitude transmission in the disk resonator respectively. Employing slowly varying amplitude approximation and introducing loss coefficients, we find the following coupled first order differential equations for the three waves involving the nonlinear DFG process [6, 15-17],

$$\frac{dE_{1c}(x)}{dx} = -\frac{\alpha_1}{2} E_{1c} + i\omega_1 \Gamma E_{2c} E_{Tc} \exp(-i\Delta kx)$$

$$\frac{dE_{2c}(x)}{dx} = -\frac{\alpha_2}{2} E_{2c} + i\omega_2 \Gamma E_{1c} E_{Tc}^* \exp(i\Delta kx) \tag{4.6}$$

$$\frac{dE_{Tc}(x)}{dx} = -\frac{\alpha_T}{2} E_{Tc} + i\omega_T \Gamma E_{1c} E_{2c}^* \exp(i\Delta kx)$$

where α_1, α_2 and α_T are the loss coefficients for pump, idler and THz waves, E_{Tc} is generated THz amplitude, x is the propagation distance and $\Delta k = k_1 - k_2 - k_T$ represents phase mismatch. The Γ refers to the coupling coefficient in DFG process which is expressed as,

$$\Gamma = \chi^{(2)} \sqrt{\mu_0 / (2cn_1 n_2 n_T A_{eff})} \tag{4.7}$$

where μ_0 is permeability of free space, A_{eff} is effective nonlinear interaction area and n_1, n_2, n_T are effective mode indices at pump, idler and THz frequencies respectively. In order to solve Eq. (4.6) for DFG THz wave, we consider the input pump and idler powers to be undepleted mainly because only a fraction of pump powers contribute to generate THz radiation. Also we assume phase matching condition (Δk=0) is met by employing modal phase matching technique. Then we can estimate the THz field after one round trip propagation distance (L=$2\pi R$) inside the nonlinear disk resonator as [9, 15-17],

$$E_{Tc}(x=L) = \frac{2i\omega_T \Gamma E_{1c} E_{2c}^* \exp(-i\alpha_T L/2)}{(\alpha_T - \alpha_1 - \alpha_2)} \times \left(\exp(\frac{\alpha_T - \alpha_1 - \alpha_2}{2} L) - 1 \right) \tag{4.8}$$

In the proposed emitter device, this generated THz field will couple into the THz disk provided underneath where it will be confined with resonant whispering gallery mode indices ensuring phase matching condition and finally the straight THz waveguide placed in closed proximity to the disk resonator will out-couple the DFG THz waves from the cavity and guide to the point of interest. Hence, THz output power in the receiver waveguide can be written as [6],

$$P_{out} = \left| \kappa E_{Tc}(x=L) \right|^2 \tag{4.9}$$

4.2.4 Quantum-limited THz Conversion Efficiency

According to Manly-Rowe relations, in DFG, annihilation of a number of photons at pump frequency ω_1 is associated with the creation of the same number of photons at THz

frequency ω_T and idler frequency ω_2 [15, 18-19]. This introduces an upper limit of the optical to THz conversion efficiency. The highest achievable conversion efficiency is defined by the ratio of ω_T to ω_1. If P_{1b}, P_{2b} and P_{out} represent input pump powers in the bus waveguide and generated THz power respectively, we can calculate the power-normalized optical to THz conversion efficiency for the proposed emitter by $\eta=P_{out}/P_{1b}/P_{2b}$ [15, 20-22]. Conversion efficiency is calculated at each DFG frequency with the simulation results presented in Fig. 4.7(a). With $P_{1b}=P_{2b}=1$ W input pump powers, we achieve output power of 0.197 mW, 1.1 mW and 12.9 mW at 1 THz, 3 THz and 10 THz DFG respectively. The corresponding values of power-normalized conversion efficiency are found to be 1.97×10^{-4} W^{-1}, 1.1×10^{-3} W^{-1} and 1.29×10^{-2} W^{-1}. We also analytically estimate the power normalized conversion efficiencies for those DFG frequencies by employing Eq. (4.9) and present those along with the simulated values in Fig. 4.7(b). As seen, there is a good agreement between the two. We plotted the simulated power-normalized conversion efficiencies for microring resonators based THz emitter as well in Fig. 4.7(b) [8]. In this case, the efficiencies were found to be 7.3×10^{-5} W^{-1}, 5.4×10^{-4} W^{-1} and 6.2×10^{-3} W^{-1} at 1 THz, 3 THz and 10 THz DFG respectively. Thus, we have achieved to get two times higher enhancement in THz conversion efficiency with microdisk resonators compared to microring resonators. To the best of our knowledge, the efficiency of the proposed THz emitter is relatively higher than the recently reported values [15, 20-22].

4.3   Summary

We have presented a detailed design of a novel tunable room temperature CMOS-compatible THz emitter using microdisk resonators. A nonlinear optical disk resonator is

designed with FSR of 0.05 THz, which defines the tunability resolution of the device. Another microdisk resonator using the HR Si is engineered to support the whispering gallery resonant modes for the DFG THz waves with effective indices around 2.46 meeting the phase matching condition. Full 3D FDTD simulations are carried out for a smaller version of the proposed source to prove the concept. As seen from the simulation results, the THz radiation is generated at the top nonlinear disk due to mixing of the two infrared waves and couples to the bottom THz disk overcoming the SiO_2 insulating layer. The THz radiation is resonated with the first order radial mode and out-couples to the receiver straight THz waveguide. The nonlinear mixing of the two appropriate infrared input waves in the proposed device has resulted in the sharp DFG peaks in 0.5-10 THz range as confirmed by the 2D simulations. We have achieved power-normalized conversion efficiency of 1.97×10^{-4} W^{-1} and 1.29×10^{-2} W^{-1} at 1 and 10 THz respectively. We believe, the proposed source can enable on-chip integrated THz systems.

4.4 References

1. Grutter, K. (2013). Optical whispering-gallery mode resonators for applications in optical communication and frequency control.

2. Bogaerts, W., De Heyn, P., Van Vaerenbergh, T., De Vos, K., Kumar Selvaraja, S., Claes, T., Dumon, P., Bienstman, P., Van Thourhout, D., & Baets, R. (2012). Silicon microring resonators. Laser & Photonics Reviews, 6(1), 47-73.

3. Hagness, S. C. (1998). FDTD computational electromagnetics modeling of microcavity lasers and resonant optical structures (Doctoral dissertation, Northwestern University).

4. Soltani, M., Yegnanarayanan, S., & Adibi, A. (2007). Ultra-high Q planar silicon microdisk resonators for chip-scale silicon photonics. Optics express, 15(8), 4694-4704.

5. Yariv, A. (2002). Critical coupling and its control in optical waveguide-ring resonator systems. IEEE Photonics Technology Letters, 14(4), 483-485.

6. Amarnath, K. (2006). Active microring and microdisk optical resonators on indium phosphide (Doctoral dissertation).

7. Boyd, R. W., & Heebner, J. E. (2001). Sensitive disk resonator photonic biosensor. Applied Optics, 40(31), 5742-5747.

8. Sinha, R., Karabiyik, M., Al-Amin, C., Vabbina, P. K., Güney, D. Ö., & Pala, N. (2015). Tunable Room Temperature THz Sources Based on Nonlinear Mixing in a Hybrid Optical and THz Micro-Ring Resonator. Scientific Reports, 5, 9422.

9. Baehr-Jones, T., Hochberg, M., Soref, R., & Scherer, A. (2008). Design of a tunable, room temperature, continuous-wave terahertz source and detector using silicon waveguides. JOSA B, 25(2), 261-268.

10. Dai, J., Zhang, J., Zhang, W., & Grischkowsky, D. (2004). Terahertz time-domain spectroscopy characterization of the far-infrared absorption and index of refraction of high-resistivity, float-zone silicon. JOSA B, 21(7), 1379-1386.

11. Almeida, V. R., Barrios, C. A., Panepucci, R. R., & Lipson, M. (2004). All-optical control of light on a silicon chip. Nature, 431(7012), 1081-1084.

12. COMSOL Multiphysics 4.3b. Available: http://www.comsol.com/products. (Date of access: 01/10/2015).

13. Lumerical Solutions, Inc. Available: http://www.lumerical.com/tcad-products/fdtd/. (Date of access: 01/10/2015).

14. Lee, Y. S. (2009). Principles of terahertz science and technology (Vol. 170). Springer Science & Business Media.

15. Chen, T., Sun, J., Li, L., & Tang, J. (2012). Proposal for efficient terahertz-wave difference frequency generation in an AlGaAs photonic crystal waveguide. Journal of Lightwave Technology, 30(13), 2156-2162.

16. Boyd, R. W. (2008). Nonlinear Optics. Nonlinear Optics: Third Edition. By Robert W. Boyd. ISBN 978-0-12-369470-6. Published by Academic Press/Elsevier, Inc. Oxford, UK.

17. Yariv, A. (1997). Optical electronics in modern communications (Vol. 1). Oxford University Press, USA.

18. Suhara, T., & Fujimura, M. (2013). Waveguide nonlinear-optic devices (Vol. 11). Springer Science & Business Media.

19. Waldmueller, I., Wanke, M. C., & Chow, W. W. (2007). Circumventing the Manley-Rowe quantum efficiency limit in an optically pumped terahertz quantum-cascade amplifier. Physical review letters, 99(11), 117401.

20. Saito, K., Tanabe, T., Oyama, Y., Suto, K., & Nishizawa, J. I. (2009). Terahertz-wave generation by GaP rib waveguides via collinear phase-matched difference-frequency mixing of near-infrared lasers. Journal of Applied Physics, 105(6), 063102.

21. Ruan, Z., Veronis, G., Vodopyanov, K. L., Fejer, M. M., & Fan, S. (2009). Enhancement of optics-to-THz conversion efficiency by metallic slot waveguides. Optics express, 17(16), 13502-13515.

22. Saito, K., Tanabe, T., & Oyama, Y. (2015). Design of an efficient terahertz wave source from a GaP waveguide embedded in a silicon slot waveguide. Journal of the European Optical Society-Rapid publications, 10.

CHAPTER 5

Engineered Core-shell Nanostructures for Plasmon Enhanced Difference Frequency

Generation in THz Range

5.1   Proposed Device

In this chapter, we have proposed and investigated in detail, for the first time, a spherical core-shell nanostructures utilizing plasmonic resonances in order to achieve enhanced difference frequency generation (DFG) across 0.5-10 THz range with continuous tunability. The proposed structure is composed of Au core acting as plasmonic nanocavity, which is encapsulated by an intrinsic second order ($\chi^{(2)}$) nonlinear optical (NLO) crystal (e.g. AlN, BaTiO$_3$, LiNbO$_3$, KTP, KbNO$_3$) and an SiO$_2$ outer layer preventing interparticle near-field coupling. Our simulations show that substantially intensified tunable THz output can be achieved when the proposed nanoengineered composite is exposed with appropriate input pump and idler waves. The spectral linewidth of the THz radiation can also be tuned by controlling the pulse width of the input optical waves. Here, we engineered the proposed structure with a resonance peak around 800 nm. In order to achieve continuously tunable THz generation across 0.5-10 THz range, we kept the idler fixed at 800 nm and varied the pump wave from 798.9 nm to 779.2 nm. DFG THz generation process through the proposed core-shell nanostructures are illustrated in Figure 5.1.
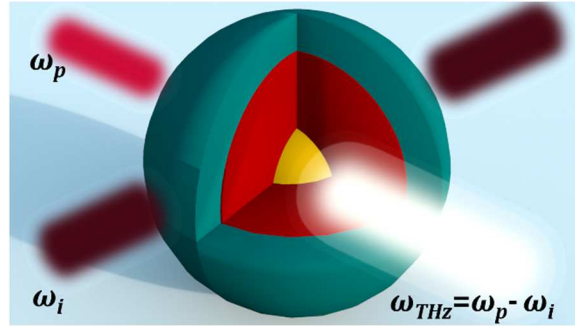
Figure 5.1 | Schematic illustration of DFG. Core-shell nanostructures are exposed with the resonant pump and signal optical waves, ω_p and ω_i respectively in order to achieve appropriate DFG in THz frequency.

5.2   Design, Simulation Results and Discussion

In this section, we present simulation results with detail design steps from engineering the core-shell structure with appropriate resonance peak to continuously tunable THz generation across 1-10 THz range. Here, we also provide a fair comparison of the proposed core-shell structure with Au as core against the bare nonlinear core and two other core-shell nanostructures with NLO and SiO_2 as core material. Detail numerical analysis of the proposed core-shell structures was performed using three-dimensional (3D) finite-difference time-domain (FDTD) method (Lumerical package 2016) [1]. Perfectly matched layers (PMLs) were used as the boundaries, and the light source was a linear electrical plane wave. The nonlinear $\chi^{(2)}$ value was set to 300 pm/V. The 3D grid sizes in all three axes were set to 5 nm. For simulation, we used AlN as nonlinear optical (NLO) material. Refractive indices of AlN, Au and SiO_2 were taken from Pastrňák and Roskovcová, Johnson and Christy, and Palik, respectively [2-4].

The first design goal was to engineer the core-shell nanostructure in such a way that it supports resonances at the desired pump and idler frequencies around 800 nm, which is

done by selectively determining the size of the different layers of the structure. First, we engineered the bare NLO spherical core with the diameter size of 340 nm, as shown in Figure 5.2(a). The scattering cross-section of the engineered bare NLO core is presented in Figure 5.3, which shows a very wide plasmonic resonance with weak scattering peak around 800 nm. Recently, an engineered core-shell structure with NLO as core, Au and SiO_2 as outer shells, has been reported for difference frequency generation at near infrared frequencies [5]. Hence, we engineered our first core-shell structures placing NLO as core. This structure consists of 260 nm diameter NLO nanoparticle with 50 nm encapsulation with Au layer and another 50 nm coating of SiO_2 outer layer, as illustrated in Figure 5.2b. The scattering cross-section of the engineered core-shell structure is presented in Figure 5.3, which corresponds to relatively stronger scattering dipole at 800 nm wavelength compared to bare NLO core. Difference frequency generation process can be enhanced significantly if the structure shows higher scattering either at input frequencies or at the generated frequency or both [5]. Now, if we choose NLO as a core, then the generated wave has to pass through the Au layer, which might cause losses. Hence, we tried to engineer the next core-shell structure with SiO_2 as core. This engineered core-shell structure consists of 80 nm diameter of SiO_2 sphere with 30 nm of Au coating and 80 nm of NLO outer shell, as shown in Figure 5.2(c). We calculated scattering of the core-shell structure, which exhibits a wide resonance around 800 nm and a stronger scattering compared to the other two designed structures, as shown in Figure 5.3. Then, we engineered the proposed core-shell structures selecting Au as core material. The proposed engineered structure consists of 100 nm diameter Au, 130 nm coating of NLO material and 40 nm of SiO_2 encapsulation layer, as illustrated in Figure 5.2(d). Scattering of the

proposed structure is presented in Figure 5.3, corresponding to a strong resonance peak around 800 nm. Thus the proposed oriented spherical core-shell structure provides the well confined and higher scattering plasmon resonance mode compared to the above-mentioned other oriented core-shell structures.
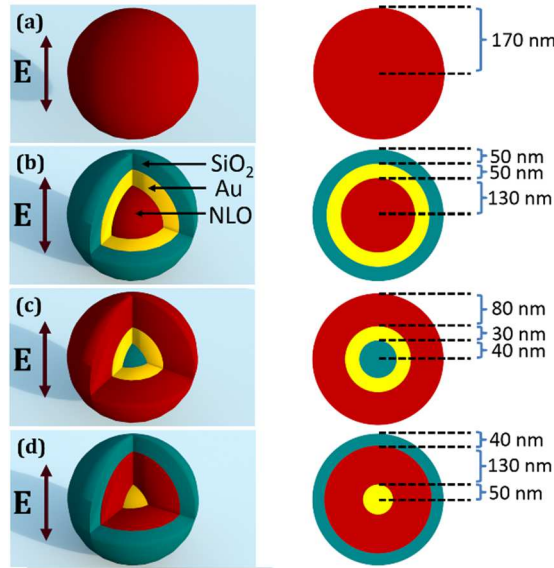
Figure 5.2 | Schematic of the core-shell nanostructures. (a) Engineered bare NLO core. (b) Engineered core-shell nanostructure with NLO as core. (c) Engineered core-shell structure with SiO_2 as core. (d) The proposed core-shell nanostructure with Au as core.

According to DFG theory as described in Chapter 2, polarization due to second-order nonlinearity acts as a source to generate DFG electric field wave, which is proportional to the amplitude of both the input pump and idler optical waves [6]. Therefore, the proposed core-shell structures require further investigation to ensure that the structures support resonance modes with high electric field enhancement. Hence we put a monitor in the middle of the structure to observe the electric field intensity at optical waves. The behavior of electric field intensity enhancement inside the bare NLO core and the core-

shell structures, as mentioned in Figure 5.2, is presented in Figure 5.4. It is clearly evident from the figure that bare NLO core show the weakest input field intensity of 3.5 at its respective resonant peak. On the other hand, we achieved the highest field intensity enhancement of 490 at 800 nm resonance wavelength for the proposed core-shell structure with Au as core. The other two core-shell structures with NLO as core and SiO_2 as core exhibit intensity enhancement of 36 and 120, respectively. The resonance electric field modes at 800 nm for all the investigated structures are summarized in Figure 5.5. For the bare NLO core, the mode profile is weakly concentrated inside the nonlinear core material while large amount of energy is outside the material coupled to air. Since, efficient DFG operation require a significant amount of energy of the resonant mode to be concentrated in the nonlinear material, this bare NLO core will show very weak DFG. On the other hand, for the proposed core-shell structures, it is clearly observed that plasmon resonance mode is strongly concentrated in the NLO material with very high electric field intensity. Therefore, it promises to show strong DFG compared to other structures.
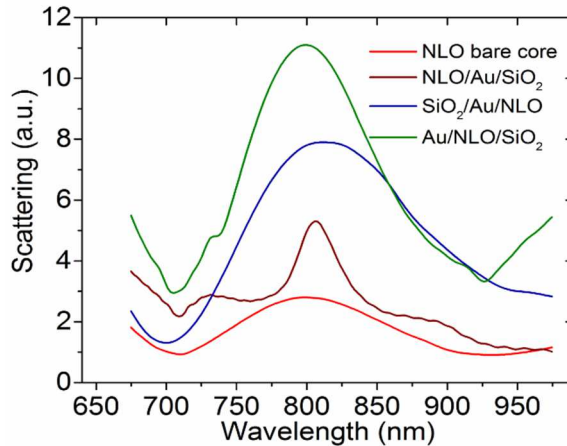
Figure 5.3 | Scattering of spherical core-shell structures. The proposed core-shell structures show strong scattering with resonance peak compared to other structures.
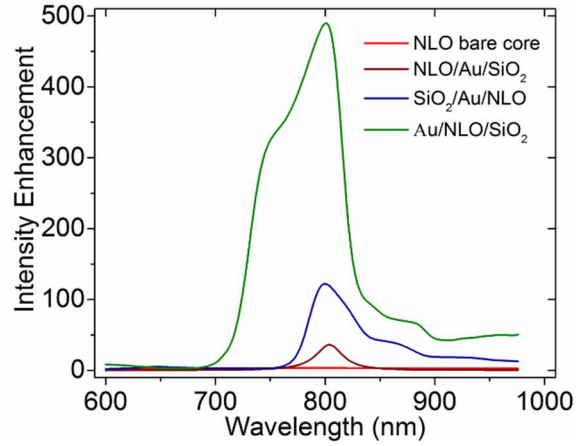
Figure 5.4 | Comparison of Intensity Enhancement. The proposed core-shell structure show highest intensity enhancement for input frequencies compared to other structures.
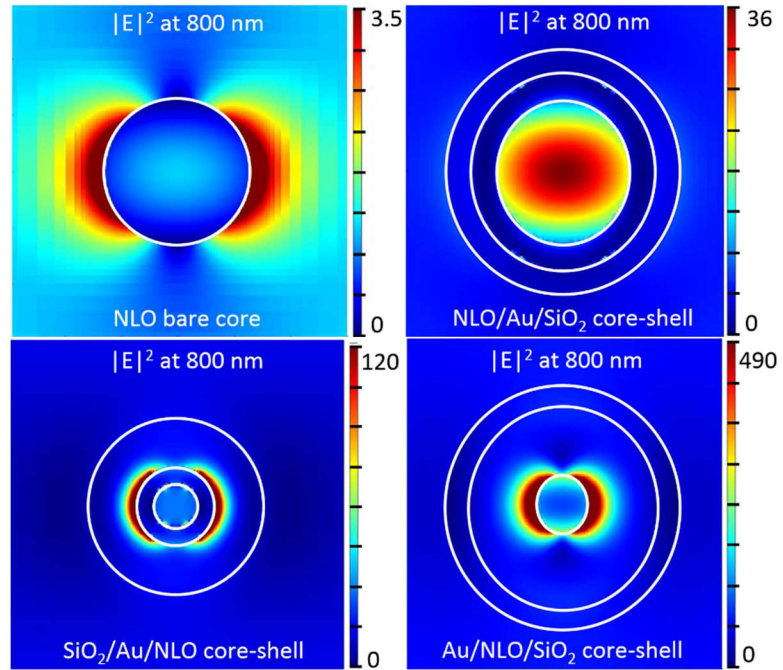
Figure 5.5 | Resonant modal profiles. The proposed core-shell structure showing highly concentrated modal profiles in NLO with highest intensity enhancement.

Finally, the engineered structures were simulated in 3D to achieve DFG in the desired THz range. The input electric field was taken as linear electrical plane wave with 2 ps pulse length, 4 ps offset corresponding to 0.22 THz bandwidth. While the idler input

wave was kept fixed at 800 nm wavelength, the resonant scattering peak observed in Figure 5.3, the pump input wave was varied and set to 797.9 nm, 795.8 nm, 793.7 nm, 791.6 nm, 789.5 nm, 787.4 nm, 785.2 nm, 783.3 nm, 781.3 nm and 779.2 nm consequently to achieve difference frequency generation in the 1-10 THz range of our interest. The output THz power spectra achieved from the proposed core-shell nanostructure are shown in Figure 5.6. The linewidth of the generated THz waves is found to be 0.44 THz, which is two times the input bandwidth selected. Hence, the spectral linewidth of the generated THz output can also be tuned by modulating the input bandwidth.
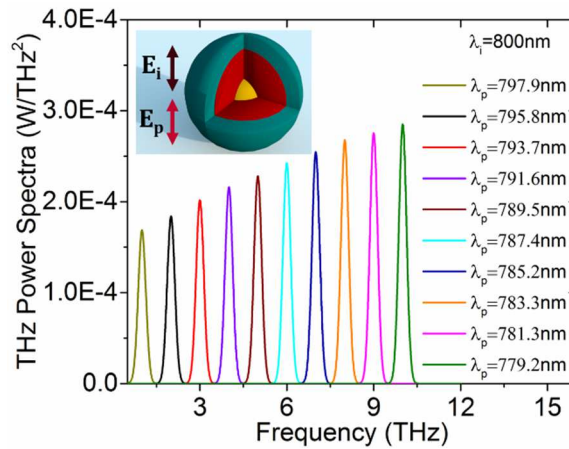
Figure 5.6 | 3D simulation results of DFG in the proposed structure. Continuously tunable THz radiation was achieved by keeping the idler input fixed at 800 nm and varying the pump wave from 797.9 nm to 779.2 nm.

Then, the proposed core-shell structure was compared against other mentioned structures in terms of DFG THz output power, which is summarized in Figure 5.7. Peak power of the DFG pulse was calculated by dividing the total energy of the pulse with full width half maximum (FWHM) pulse duration. From the figure, it is evident that approximately 10^4 times more power was achieved with the proposed core-shell structure

compared to bare NLO core. This is due to the highly concentrated plasmonic resonance with high intensity enhancement at the input frequencies in the proposed core-shell structure, as observed in Figure 5.5.
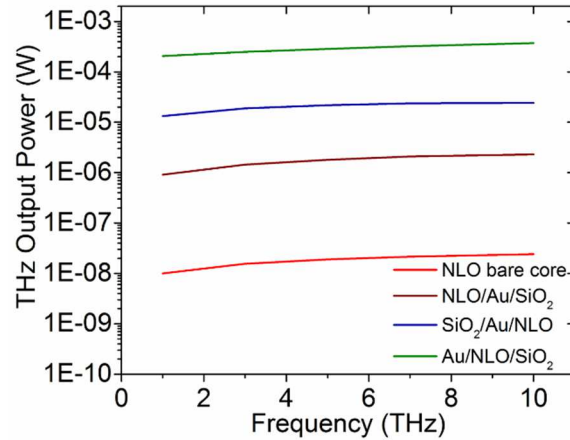
Figure 5.7 | THz output power comparison. The proposed core-shell structure show 10^4 times power enhancement compared to bare NLO core.

5.3   Summary

We have proposed and numerically investigated a core-shell nanostructure for plasmon enhanced difference frequency generation in 0.5-10 THz range with continuous tunability. The proposed structure was compared against bare NLO core, core-shell with NLO as core and core-shell with SiO_2 as core, in terms of scattering, input field intensity enhancement, resonance modal profiles and THz output power. The proposed nanostructure showed 10^4 times more THz output power compared to bare NLO core.

5.4   References

1. Lumerical Solutions, Inc. Available: http://www.lumerical.com/tcad-products/fdtd/. (Date of access: 01/10/2015).

2. Pastrňák, J., & Roskovcova, L. (1966). Refraction index measurements on AlN single crystals. physica status solidi (b), 14(1).

3. Johnson, P. B., & Christy, R. W. (1972). Optical constants of the noble metals. Physical review B, 6(12), 4370.

4. Palik, E. D. (1998). Handbook of optical constants of solids (Vol. 3). Academic press.

5. Zhang, Y., Manjavacas, A., Hogan, N. J., Zhou, L., Ayala-Orozco, C., Dong, L., Day, J.K., Nordlander, P., & Halas, N. J. (2016). Toward surface plasmon-enhanced optical parametric amplification (SPOPA) with engineered nanoparticles: a nanoscale tunable infrared source. Nano letters, 16(5), 3373-3378.

6. Lee, Y. S. (2009). Principles of terahertz science and technology (Vol. 170). Springer Science & Business Media.

CHAPTER 6

Plasmonic Nanogap Antenna Enhanced DFG in THz Range

6.1 Proposed Device

We have presented a novel plasmonic nanogap antenna geometry – the dimer rod-tapered antenna (DRTA) and created hot-spot in their gap, where the incident electric field intensity is enhanced by a factor of 4.1×10^5. The performance of this antenna structure was compared against widely used dimer rod type antenna (DRA) in terms of normalized scattering intensity and electric field intensity enhancement. As the intensity of the difference frequency generation (DFG) field wave is proportional to the square of the intensity of the fundamental optical waves, this DFG nonlinear process can be highly enhanced from the strongly intensified incident field wave in these structures [1]. In this work we propose, for the first time, to incorporate a second-order nonlinear optical crystal (e.g. AlN, $BaTiO_3$, $KNbO_3$, $LiNbO_3$, KTP, electro-optic polymer) into the hot-spot of plasmonic nanogap antennas to achieve continuously tunable enhanced DFG across the 0.5-10 THz range. The proposed structure is illustrated in Figure 6.1 with a three dimensional schematic. The detail numerical analysis of the proposed structures was carried out using commercial finite difference time domain (FDTD) method based commercial simulation tool. The plasmonic DRTA was engineered to support resonances with high electric field intensity enhancement at both the input pump and idler wavelengths around 1550 nm to facilitate DFG in the region of interest. Simulation results for the proposed device showed approximately hundred times enhancement in THz generation when compared with a standard DRA structure. Tunable THz output in the 0.5-10 THz

81

region was achieved by keeping the idler input wave fixed at 1550 nm wavelength and changing the pump wavelength from 1546 nm to 1474 nm. The spectral linewidth of the output THz radiation can also be tuned by controlling the pulse width of the input waves.
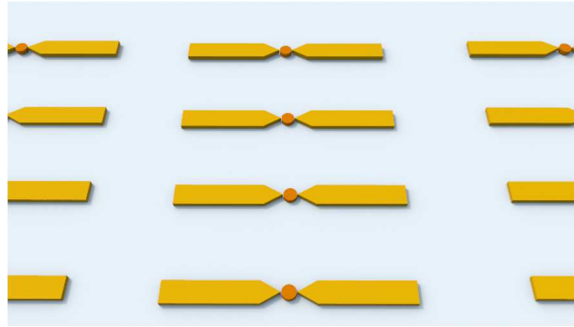
Figure 6.1 | Proposed device structure. Three dimensional schematic of periodic clusters of plasmonic nanogap antenna coupled nonlinear nanodot structures on a quartz substrate.

6.2   Design, Simulation Results and Discussion

The proposed device consists of infinitely extended array of periodic clusters of DRTA coupled nonlinear nanodot structure on a quartz substrate. Each unit is separated by 2μm distance from each other in order to prevent interparticle coupling for the input infrared optical waves. First goal of this work was to design the DRTA structure with a detail comparison against the standard DRA structure by investigating in detail the optical properties of the structures. We used gold to construct our antenna structure. The problem of solving cluster arrays can be solved by treating a single unit with periodic boundary condition in the simulation. 3D FDTD nonlinear simulations were performed using commercial Lumerical package FDTD Solutions v8.15 [2]. Periodic boundary conditions were applied to both the x and y axis and perfectly matched layers (PMLs) were used at

the z axis boundaries. We used linear electrical plane wave as the input optical light source. The nonlinear $\chi^{(2)}$ value was set to 10 pm/V. Regional mesh was used with a minimum mesh size of 0.5 nm in all three axes. We used refractive index of AlN, Au and quartz Pastrňák and Roskovcová, Johnson and Christy, and Palik, respectively [3-5]. In order to calculate and optimize the optical response of the proposed antenna structure, the Green's tensor method was used by taking into account the influence of the substrate as well [6, 7].

First of all the incorporation of the high refractive index NLO nanodot into the hot-spot of the Au nanogap antennas influences the plasmonic resonance mode of the nano-antennas, since these are highly sensitive to changes in the dielectric environment. In particular, the plasmonic resonance mode experiences a red shift to higher wavelengths due to the increase in the surrounding effective dielectric constant [8, 9]. Therefore, the alone antenna structure needs to be engineered first for a smaller wavelength and then again investigated along with NLO nanodot to make sure it provides the resonance mode at the wavelength of our interest. It is well known that the resonance of DRA can be spectrally tuned by varying the length of the antenna arms [10, 11]. The dimension of the engineered DRA coupled NLO nanodot structure is illustrated in Figure 6.2(a). The engineered DRA is composed of two identical nanorod placed side by side with 20 nm gap in between them. Each nanorod is 280 nm in length, 40 nm in width and 40 nm in thickness. The scattering spectra of the alone antenna and antenna coupled with nanodot are shown in Figure 6.3. Polarization direction of the incoming light was chosen as parallel to the length of the antenna arm. Then antenna showed a resonance peak at 1475 nm and NLO nanodot coupled DRA exhibited a red shift in resonance to 1550 nm wavelength as expected.
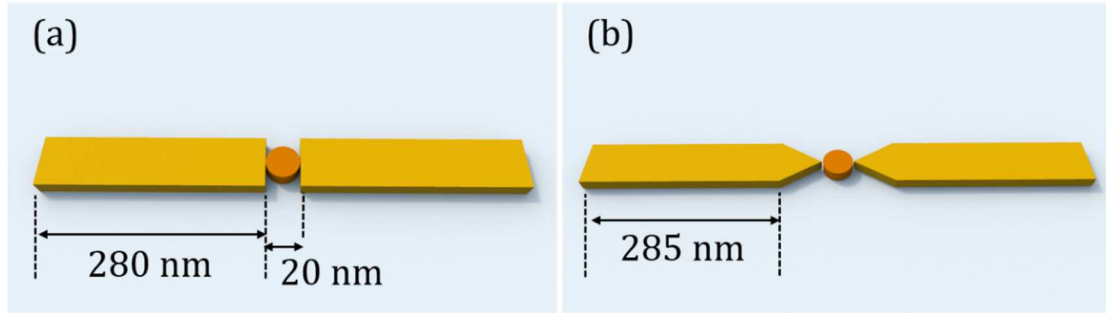
Figure 6.2 | Geometry of antennas coupled with NLO nanodot on quartz substrate.
(a) A standard dimer rod type antenna (DRA) with NLO nanodot in their nanogap. (b) The proposed novel antenna geometry – dimer rod-tapered antenna (DRTA) with NLO nanodot positioned in the hot-spot.

Then the proposed DRTA coupled NLO nanodot structure was engineered with the dimension as illustrated in Figure 6.2(b), to support resonance scattering peak at 1550 nm wavelength. The rectangular part of the antenna arm is of 285 nm in length, 40 nm in width and 40 nm in thickness and the tapered arm size is of 40 nm in length. The scattering spectra of the proposed structure is shown in Figure 6.3, which shows the resonance of the DRTA at 1520 nm wavelength and it shifts to 1550 nm wavelength after coupling the NLO nanodot of 20 nm diameter.

After confirming the resonance peak at the desired wavelength, the structures were further investigated to observe the electric field intensity enhancement in the hot-spot. We put a monitor in the middle of the antenna structure perpendicular to z axis observe the field intensity enhancement. The calculated intensity enhancement for both the DRA and proposed DRTA antenna coupled nanodot devices are summarized in Figure 6.4. The intensity enhancement for the proposed DRTA based structure was found to be of 4.1×10^5, while it was of 4×10^4 for DRA, which is 10.25 times smaller. Resonance modal profiles at

1550 nm for both the structure are shown in Figure 6.5, which correspond to dipole type resonances as seen from the Figure.
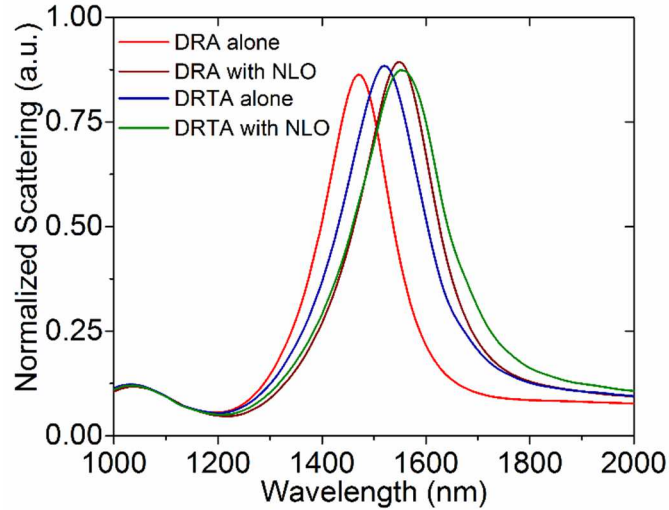
Figure 6.3 | Normalized scattering of antennas. Scattering spectra are summarized for dimer rod type antenna (DRA) alone, DRA along with NLO nanodot, the proposed novel dimer rod-tapered antenna (DRTA) alone and DRTA antenna with NLO nanodot positioned in the hot-spot.

Finally, the engineered DRTA coupled NLO nanodot structures were simulated in 3D to achieve DFG in the desired THz range. The input electric field was taken as linear electrical plane wave with 2 ps pulse length, 4 ps offset corresponding to 0.22 THz bandwidth. While the idler input wave was kept fixed at 1550 nm wavelength, the resonant scattering peak observed in Figure 6.3, the pump input wave was varied from 1546 nm to 1474 nm continuously to achieve tunable difference frequency generation in the 0.5-10 THz range of our interest. The output THz power spectra achieved from the proposed DRTA based nanostructure are shown in Figure 6.6. The linewidth of the generated THz waves is found to be 0.44 THz, which is dependent on the spectral width of the input optical waves and found to be two times the input bandwidth selected. Hence, the spectral

linewidth of the generated THz output can also be tuned by modulating the input bandwidth.
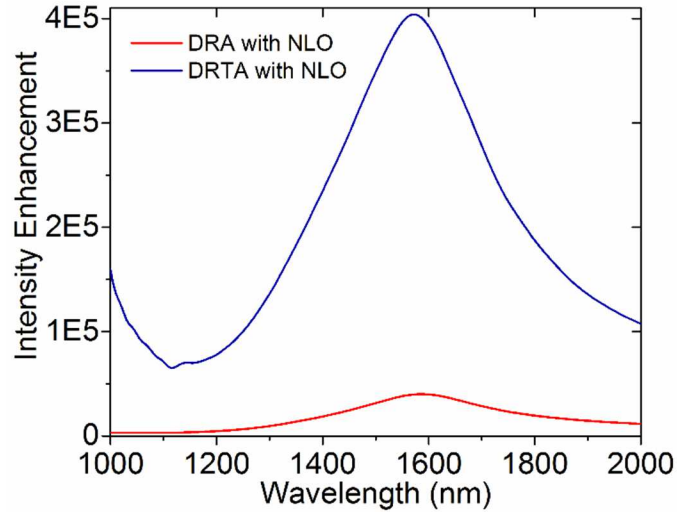
Figure 6.4 | Investigation of input optical field enhancement. The structure were engineered to have plasmonic resonance at 1550 nm wavelength. For that frequency, we observed electric field intensity enhancement of 4.1×10^5 and 4×10^4 for the proposed novel DRTA nanostructure and a standard DRA structure incorporated with nonlinear optical material in the middle of the antenna nanogap.

Then, the proposed DRTA coupled NLO nanodot emitter was compared against standard DRA coupled emitter structure in terms of DFG THz output power, which is summarized in Figure 6.7. Peak power of the DFG pulse was calculated by dividing the total energy of the pulse with the full width half maximum (FWHM) pulse duration of the generated wave. From the figure, it is evident that approximately 100 times more power was achieved with the proposed antenna structure compared to using the standard DRA structure. This is due to the highly concentrated plasmonic resonance with high intensity enhancement at the input frequencies in the nanogap of the proposed novel antenna geometry, as observed in Figure 6.5.
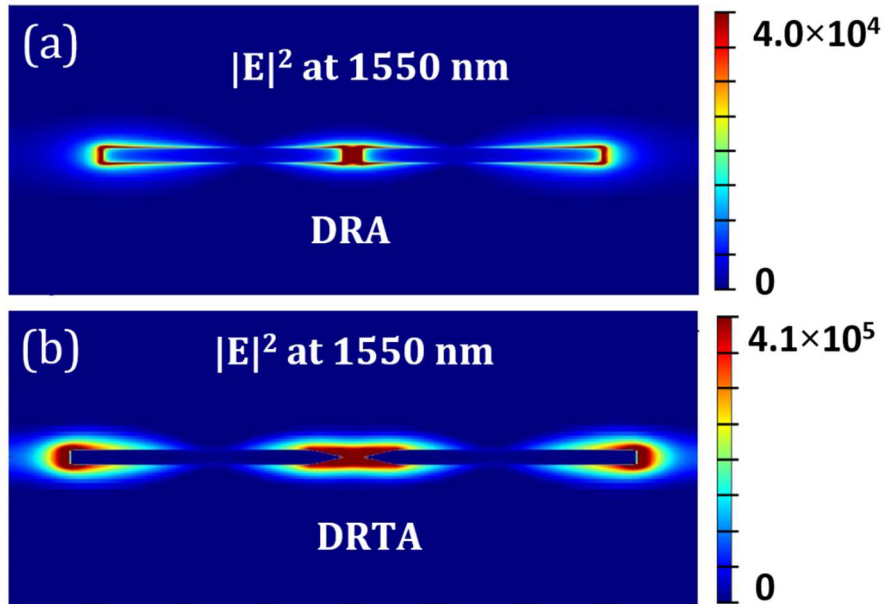
Figure 6.5 | Plasmonic resonance modal profile. (a) Electric field intensity modal profile for the plasmonic resonance observed at 1550 nm wavelength with a standard dimer rod type antenna along with NLO nanodot positioned in the nanogap. (b) Field intensity resonant modal profile for the proposed dimer rod-tapered antenna structure.
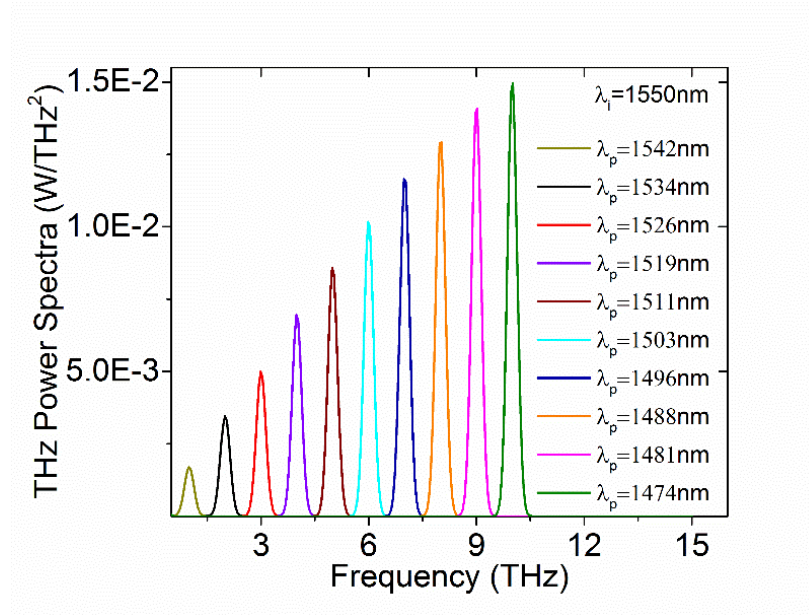
Figure 6.6 | 3D simulation results of DFG in the proposed structure. Continuously tunable THz radiation was achieved by keeping the idler input fixed at 1550 nm and varying the pump wave from 1546 nm to 1474 nm.
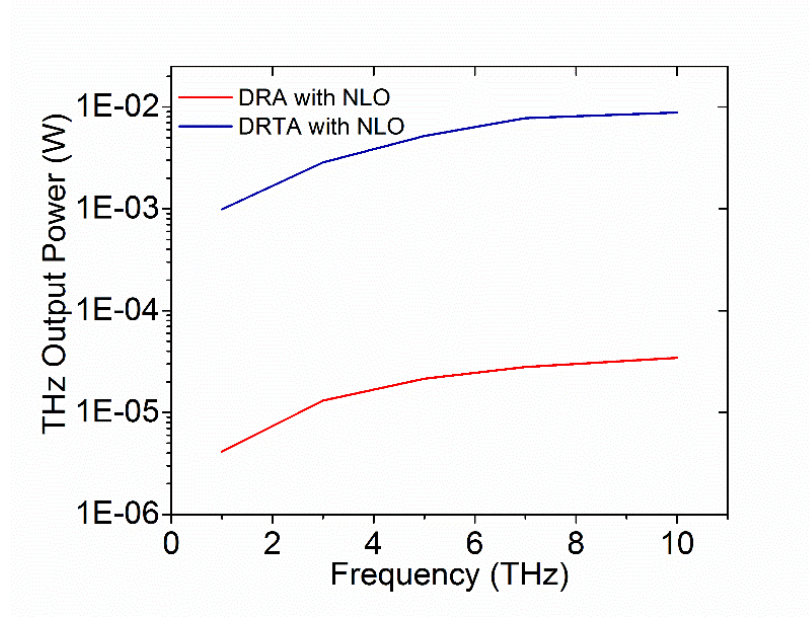
Figure 6.7 | THz output power comparison. The proposed antenna structure showed approximately two orders of enhancement in THz output power, when compared to standard DRA based emitter.

6.3   Summary

We have proposed and numerically investigated a novel plasmonic antenna geometry, DRTA, which showed a huge intensity enhancement of 4.1×10^5 creating a hot-spot in the nanogap between the dimer. Further, we have proposed a novel THz emitter by incorporating NLO nanodot particle in the hot-spot of the engineered DRTA for nanogap enhanced plasmonic resonance based difference frequency generation in 0.5-10 THz range with continuous tunability. The proposed structure was further compared against a simple DRA based emitter, in terms of scattering, input field intensity enhancement, resonance modal profiles and THz output power. The proposed nanostructure showed approximately 100 times more THz output power compared to the DRA based emitter.

6.4 References

1. Lee, Y. S. (2009). Principles of terahertz science and technology (Vol. 170). Springer Science & Business Media.

2. Lumerical Solutions, Inc. Available: http://www.lumerical.com/tcad-products/fdtd/. (Date of access: 01/10/2015).

3. Pastrňák, J., & Roskovcova, L. (1966). Refraction index measurements on AlN single crystals. physica status solidi (b), 14(1).

4. Johnson, P. B., & Christy, R. W. (1972). Optical constants of the noble metals. Physical review B, 6(12), 4370.

5. Palik, E. D. (1998). Handbook of optical constants of solids (Vol. 3). Academic press.

6. Paulus, M. and Martin, O.J. (2001). Light propagation and scattering in stratified media: a Green's tensor approach. JOSA A, 18(4), pp.854-861.

7. Kern, A.M. and Martin, O.J. (2009). Surface integral formulation for 3D simulations of plasmonic and high permittivity nanostructures. *JOSA A*, *26*(4), pp.732-740.

8. Aouani, H., Rahmani, M., Navarro-Cía, M. and Maier, S.A. (2014). Third-harmonic-upconversion enhancement from a single semiconductor nanoparticle coupled to a plasmonic antenna. Nature nanotechnology, 9(4), pp.290-294.

9. Metzger, B., Hentschel, M., Schumacher, T., Lippitz, M., Ye, X., Murray, C.B., Knabe, B., Buse, K. and Giessen, H. (2014). Doubling the efficiency of third harmonic generation by positioning ITO nanocrystals into the hot-spot of plasmonic gap-antennas. *Nano letters*, *14*(5), pp.2867-2872.

10. Fischer, H. and Martin, O.J. (2008). Engineering the optical response of plasmonic nanoantennas. *Optics express*, *16*(12), pp.9144-9154.

11. Thyagarajan, K., Rivier, S., Lovera, A. and Martin, O.J. (2012). Enhanced second-harmonic generation from double resonant plasmonic antennae. Optics express, 20(12), pp.12860-12865.

CHAPTER 7

Difference Frequency Generation across THz Range by Film-Coupled Plasmonic

Grating Resonators

7.1 Proposed Device

Because of their ability to strongly localize and enhance optical fields, plasmonic nanostructures have the potential to dramatically enhance the inherent nonlinear response of materials. In this work, we present the impact of this plasmonic interaction by investigating continuously tunable difference frequency generation (DFG) in the 0.5-10 THz range from a platform of film-coupled plasmonic grating resonators. Figure 1 shows the three dimensional and cross-sectional view of the proposed THz emitter device. Here, 200 nm of Al film layer and the engineered Al grating resonators are separated by a 20 nm thin nonlinear optical (NLO) material (e.g. AlN, $BaTiO_3$, $KNbO_3$, $LiNbO_3$, KTP, BBO, electro-optic polymer) film. This nanoscale junction, with an ultra-smooth interface, forms a waveguide cavity resonator with a controllable large electric field enhancement, whose plasmon resonance can be easily tuned independently by adjusting the grating width and period [1]. The grating was engineered with 610 nm width, 715 nm period, 150 nm thickness and 50 μm length to support a plasmonic resonance at 1550 nm wavelength. We observed an electric field intensity enhancement of 620 for the resonant mode in the engineered resonators. High resistivity (HR) Si was chosen as substrate due to its transparency across the THz range of interest [2-5].

The proposed structure can be fabricated using the standard nanofabrication tools and techniques. 200 nm of Al can be deposited on top of an undoped high resistivity (HR)

Si wafer with electron-beam evaporation technique. Nonlinear layer of 20 nm could be either sputtered for the AlN case or spun-cast for the polymer case. Finally, electron-beam lithography (EBL) can be used to construct the periodic arrays of Al grating resonators with lift-off techniques.
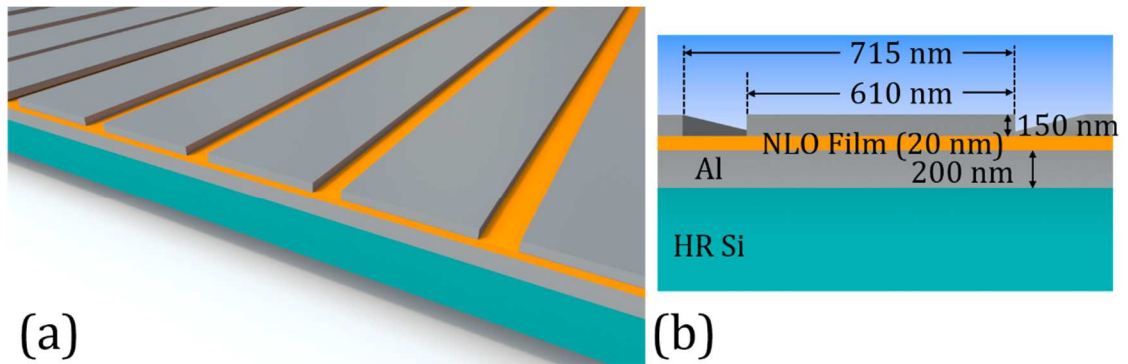
Figure 7.1 | Proposed device structure. (a) Three dimensional schematic of film-coupled plasmonic grating resonators. (b) Cross-sectional view of the same THz emitter device showing the dimension and material.

7.2   Design, Simulation Results and Discussion

The proposed device consists of infinitely extended array of periodic grating resonators coupled to thin NLO film. First task of this work was to design the plasmonic grating resonators in order to obtain the desired resonant mode at 1550 nm wavelength. Commercial Lumerical package FDTD Solutions v8.15 was used to investigate in detail the proposed grating based THz emitter device [6]. Since, the grating structures itself are in periodic fashion, only one periodical unit of grating was considered to observe optical properties and DFG generation with periodic boundary condition. This grating resonators geometry can be modelled in two dimension by considering the cross-section of the device as shown in Figure 7.1(b), which not only takes all the layers of the device into account but

91

also provides better computational efficiency. Periodic boundary conditions were applied to the x axis and perfectly matched layers (PMLs) were used at the y axis boundaries. We used linear electrical plane wave as the input optical light source. The nonlinear $\chi^{(2)}$ value was set to 100 pm/V. Regional mesh was used with a minimum mesh size of 0.5 nm in all axes around the metal grating and NLO and metal film layers. We used refractive index of AlN from Pastrňák and Roskovcová and refractive index for Al and high resistivity Si both from Palik [7, 8].

The geometry of film-coupled grating resonators result in a coupled plasmonic structure that behaves as an optical frequency patch antenna in such a way that the thin NLO gap layer between the metal film and metal grating defines a waveguide cavity resonator, where plasmons can propagate along the width and are reflected at the edges [9, 10]. Therefore, both the grating width and the nonlinear film layer thickness determine the plasmon resonance frequency. More specifically, the grating width defines the cavity length, on the other hand the NLO film layer determines the effective index in the waveguide. We need to investigate in detail the resonance behavior, resonance electric field modal profile especially how it is concentrated and the intensity enhancement factor of the resonant mode. Therefore, the proposed film-coupled grating resonators were studied extensively in order to understand its behavior by varying the geometrical dimension of each layer. We observed that with all other dimension fixed, increasing NLO film layer thickness makes a blue-shift in the plasmon resonance. It was also found that the variation of the grating width affects only the resonance wavelength, while variation of the NLO layer thickness affects both the resonance and the field intensity enhancement factor. For

any structure, a resonant modal profile, which show better confinement inside the NLO layer along with high intensity enhancement, is mostly sought to achieve efficient and enhanced DFG.

Reflectance spectrum of the engineered grating structures is presented in Figure 7.2. When the polarization of the incident electric field is oriented along the length of the grating (transverse electric, TE), no resonance is observed because the length of the waveguide is too long (50 μm) to support resonance around 1550 nm wavelength of interest. For the opposite polarization (transverse magnetic, TM), where electric field is oriented along the width of the grating, a strong minimum dip approaching zero is observed in the reflectance spectrum at 1550 nm, as seen from Figure 7.2. It indicates the film-coupled grating resonators behave as a near-perfect absorber, where almost all the photonic energy incident on the structures is coupled into the gap region [11]. In order to provide more evidence to support this behavior, the power absorption profile was also calculated for the design system, as shown in Figure 7.3, which exhibits a peak with a value of 0.9995 approaching unity. The electric field intensity modal profile is presented in Figure 7.4. Here the electric fields are mostly confined in the NLO film layer underneath the grating, as required for efficient operation of DFG, and it also makes sure that near field coupling between the grating resonators is minimized. Since the electric field intensity enhancement factor inside the NLO layer determines the enhancement of DFG operation, we put a monitor in the middle of the NLO film layer and the obtained intensity enhancement is presented in Figure 7.5. It shows maximum intensity enhancement of 620 at the resonant wavelength.
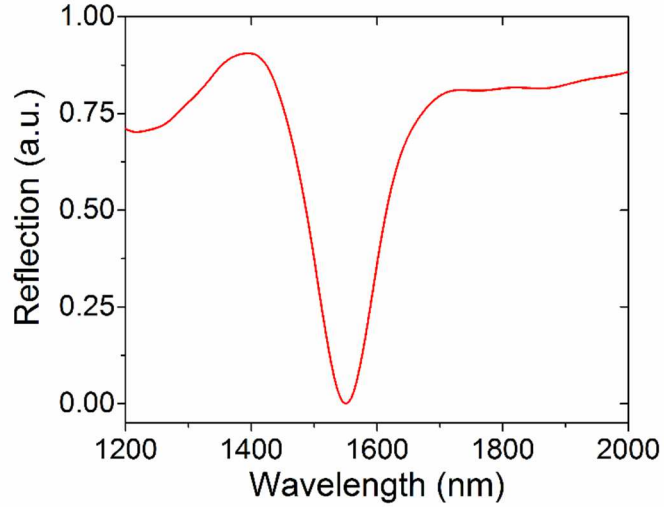
Figure 7.2 | Reflection spectrum. Reflection was calculated for the engineered film-coupled grating resonators, which show a clear resonant dip approaching zero at 1550 nm wavelength.
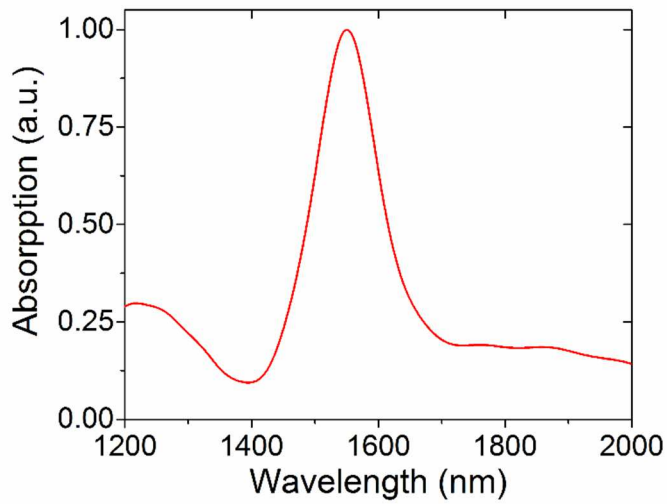
Figure 7.3 | Power absorption. The designed film-coupled resonators act as a near perfect absorber at the resonant wavelength, which is confirmed by the power absorption monitor showing a peak with a value of 0.9995 close to unity.
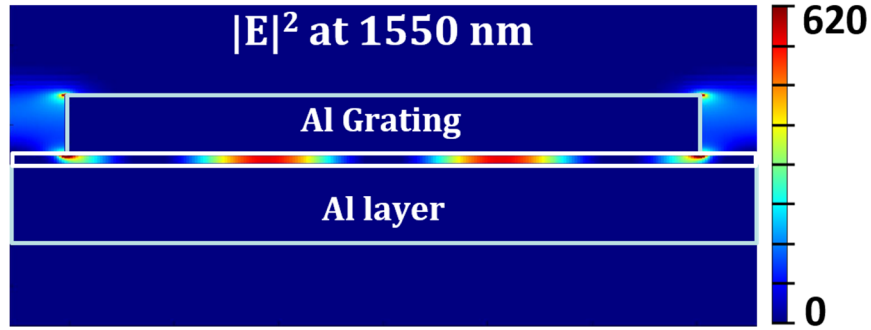
Figure 7.4 | Plasmonic resonance modal profile. Electric field intensity modal profile for the plasmonic resonance observed at 1550 nm wavelength with the engineered structure showing electric field confined in the NLO layer and the grating gap region.
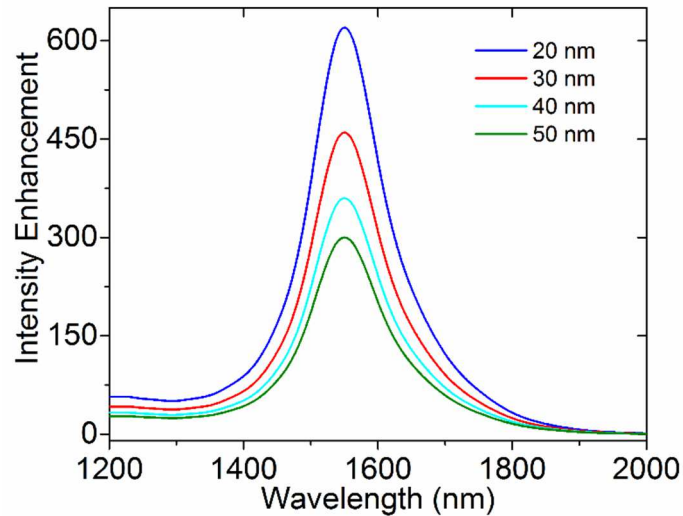
Figure 7.5 | Investigation of electric field intensity enhancement. The film-coupled grating resonators were engineered to have plasmonic resonance at 1550 nm wavelength. At that wavelength, we observed electric field intensity enhancement of 620.

Finally, the engineered film-coupled grating resonator structures were simulated in 3D to achieve DFG in the desired THz range. The input electric field was taken as linear electrical plane wave with 2 ps pulse length, 4 ps offset corresponding to 0.22 THz bandwidth. The amplitude of electric field was taken as 10^8 V/m. While the idler input wave was kept fixed at 1550 nm wavelength, the resonant absorption peak observed in

Figure 7.3, the pump input wave was varied from 1546 nm to 1474 nm continuously to achieve tunable difference frequency generation in the 0.5-10 THz range of our interest. The output THz power spectra achieved from the proposed grating based nanostructure are shown in Figure 7.6. The linewidth of the generated THz waves is found to be 0.44 THz, which is dependent on the spectral width of the input optical waves and found to be two times the input bandwidth selected. Hence, the spectral linewidth of the generated THz output can also be tuned by modulating the input bandwidth. Peak power of the DFG pulse can be calculated by dividing the total energy of the pulse with the full width half maximum (FWHM) pulse duration of the generated wave. We observed 119 μW, 553 μW and 678 μW output power at 1 THz, 5 THz and 10 THz, respectively. The THz output power is summarized in Figure 7.7 in terms of NLO film layer thickness variation. With 20 nm thickness of NLO film layer, we achieved 5 times more in THz output power compared to 50 nm NLO film layer thickness.
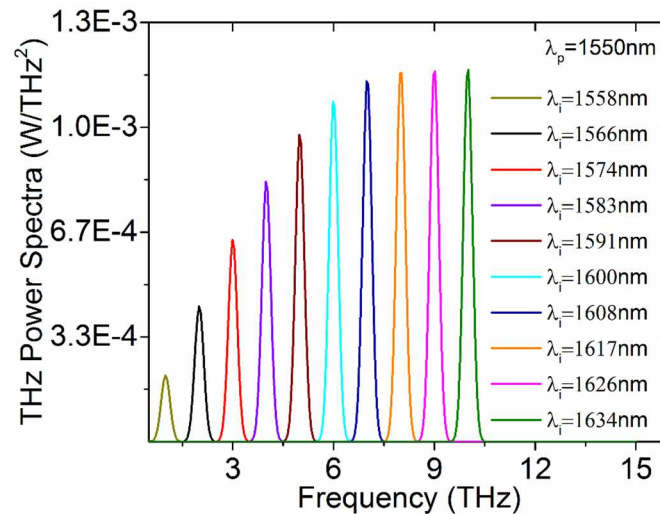
Figure 7.6 | 3D simulation results of DFG in the proposed structure. Continuously tunable THz radiation was achieved by keeping the idler input fixed at 1550 nm and varying the pump wave from 1546 nm to 1474 nm.
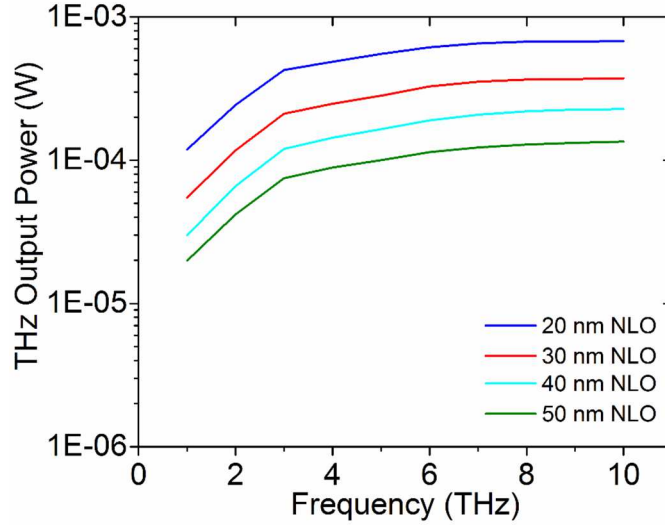
Figure 7.7 | THz output power comparison in terms of NLO film layer thickness. Achieved 5 times more output power for 20 nm NLO film layer thickness than for 50 nm thickness.

7.3   Summary

We have proposed and numerically investigated NLO film-coupled Aluminum grating resonators acting as a near-perfect absorber in order to achieve enhanced difference frequency generation across the 0.5-10 THz range with continuous tunability. For the absorption resonance peak, it showed a maximum field intensity enhance of 620.

7.4   References

1. Lassiter, J.B., Chen, X., Liu, X., Ciracì, C., Hoang, T.B., Larouche, S., Oh, S.H., Mikkelsen, M.H. and Smith, D.R. (2014). Third-harmonic generation enhancement by film-coupled plasmonic stripe resonators. *ACS Photonics*, *1*(11), pp.1212-1217.

2. Sinha, R., Karabiyik, M., Al-Amin, C., Vabbina, P.K. and Pala, N. (2014, March). Nonlinear optical resonators for tunable THz emission. In *SPIE OPTO* (pp. 898505-898505). International Society for Optics and Photonics.

3. Sinha, R., Karabiyik, M., Al-Amin, C., Vabbina, P.K., Güney, D.Ö. and Pala, N., 2015. Tunable room temperature THz sources based on nonlinear mixing in a hybrid optical and THz micro-ring resonator. *Scientific reports*, *5*.

4. Sinha, R., Karabiyik, M., Ahmadivand, A., Al-Amin, C., Vabbina, P.K., Shur, M. and Pala, N. (2016). Tunable, Room Temperature CMOS-Compatible THz Emitters Based on Nonlinear Mixing in Microdisk Resonators. *Journal of Infrared, Millimeter, and Terahertz Waves*, *37*(3), pp.230-242.

5. Sinha, R., Karabiyik, M., Al-Amin, C., Vabbina, P.K., Shur, M. and Pala, N. (2014, May). Microdisk resonators for difference frequency generation in THz range. In *SPIE Sensing Technology+ Applications* (pp. 910208-910208). International Society for Optics and Photonics.

6. Lumerical Solutions, Inc. Available: http://www.lumerical.com/tcad-products/fdtd/. (Date of access: 01/10/2015).

7. Pastrňák, J., & Roskovcova, L. (1966). Refraction index measurements on AlN single crystals. physica status solidi (b), 14(1).

8. Palik, E. D. (1998). Handbook of optical constants of solids (Vol. 3). Academic press.

9. Lassiter, J.B., McGuire, F., Mock, J.J., Ciracì, C., Hill, R.T., Wiley, B.J., Chilkoti, A. and Smith, D.R. (2013). Plasmonic waveguide modes of film-coupled metallic nanocubes. *Nano letters*, *13*(12), pp.5866-5872.

10. Ciracì, C., Britt Lassiter, J., Moreau, A. and Smith, D.R. (2013). Quasi-analytic study of scattering from optical plasmonic patch antennas. *Journal of Applied Physics*, *114*(16), p.163108.

11. Moreau, A., Ciraci, C., Mock, J.J., Hill, R.T., Wang, Q., Wiley, B.J., Chilkoti, A. and Smith, D.R. (2012). Controlled-reflectance surfaces with film-coupled colloidal nanoantennas. *Nature*, *492*(7427), pp.86-89.

CHAPTER 8

Application of THz Plasmonic Metasurfaces

8.1   Terahertz Magnetoplasmonic Metasurface with Toroidal resonances for Switching Application

In chapter 5, 6 and 7, we have designed different plasmonic resonance metasurfaces combined with NLO material with near infrared resonant frequencies to achieve tunable THz emission. These plasmonic metasurfaces can be engineered to excite sharp resonances at THz frequencies, which are highly sensitive to environmental perturbations and can be used towards switching and bio-sensing applications. In this chapter, we numerically analyzed, then fabricated and experimentally demonstrated a novel THz plasmonic metasurface based on multi-metallic unit cells as a THz switch. Here, instead of investigating conventional planar unit cells, we report on the observation of toroidal dipole using artificially engineered multi-metallic planar plasmonic resonators. The proposed resonators are designed with iron (Fe) and titanium (Ti) components acting as magnetic resonators and forming torus, respectively. The performed detail numerical analysis and then the experimental verifications confirm that the engineered plasmonic metasurfaces allow for the peculiar electromagnetic excitation of toroidal dipole in the THz domain with observed experimental quality factor of 18.

8.1.1   Toroidal Dipole Resonance

Recently, third family of electromagnetic multipoles have been reported, which are known as anapole or toroidal [1]. Between them, toroidal dipole mode are considered as the most

strong one, which can be viewed as a circular head to tail arrangements of magnetic dipoles, all squeezed into a single point as shown in Fig. 8.1. Toroidal resonant modes are peculiar localized electromagnetic excitations, which are categorized in different family of resonant modes far away from classical or conventional electromagnetic modes namely electric and magnetic dipole modes. These type of resonances can be identified as circular head to tail magnetic currents rotating around torus. The toroidal dipole is not a part of standard multipole expansion, despite corresponding to a unique current density. It is an elusive counterpart of the charge and magnetic dipoles, which is produced by currents flowing on the surface of a torus along its meridian as shown in Fig. 8.2b.
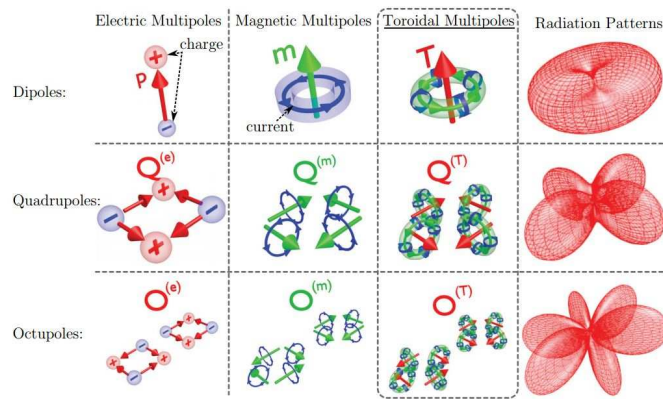
Figure 8.1 | Three families of dynamic multipoles. The three columns on the left showing the charge-current distributions, which contribute to the classical electric and metallic multipoles and the unconventional toroidal multipoles. Figure reproduced from ref. 1, APS.

8.1.2 Fabrication of Proposed Plasmonic Metasurface

Two level lithography based microfabrication processes were developed by designing two different mask for Ti and Fe respectively to fabricate the proposed THz plasmonic metasurfaces as shown in Fig. 8.2a. In order to provide the required transparency in the

THz domain, undoped and high resistivity (HR) Si wafer (>10 kΩ.cm) with the crystal orientation of <100> was used as substrate [2, 3]. The wafer was sonicated consequently in acetone, isopropyl alcohol (IPA) and deionized (DI) water for 10 minutes each and finally dried by Nitrogen to make it ready for the fabrication process. We selected a negative photoresist (NLOF 2020) for lithography process. We spin-coated the photoresist in two steps with 100 rpm/s ramp, 500 rpm/s speed for 5 sec in first step and 500 rpm/s ramp, 3000 rpm/s for 45 sec in the final step. The photoresist thickness was obtained as 2 μm. We prebaked the samples for 90 sec at 110°C and then exposed it for 5 sec with OAI (800) Mask Aligner. The exposed samples were post-baked for 90 more seconds at the same 110°C. Then we used MF26A developer for 20 sec to achieve our required feature. Using e-beam evaporation, we then deposited 300 nm of Ti layer with the rate of 2 Å/s (99.99% purity for Ti with process pressure ~5×10^{-7} Torr). The lift-off process was performed for 15 min by immersing the samples in acetone sonication bath. The the samples were plunged in remover PG for 120 min at 70 °C heat followed by IPA and DI water rinse. By following the same steps and using the second mask, we deposited Fe with e-beam evaporation tool (99.95% purity for Fe, pressure ~5×10^{-7} Torr).

8.1.3   Experimental Results and Discussion

Figure 8.2(a) represents the artistic 3D schematic view of the proposed THz plasmonic multi-metallic metasurfaces unit on a HR Si substrate explicitly mentioning the incident THz beam profile direction and electric field polarization. The device geometry with detail material specifications are demonstrated in Fig. 8.2b with a top-view profile. Figure 8.2c presents an SEM image of the fabricated arrays of unit cell with the gap distance of D_g=3

μm between central horizontal and peripheral curved resonators. The focused SEM image of the single plasmonic unit cell is shown in Fig. 8.2d. In calculating the optical characteristics of the proposed unit cell, experimentally obtained permittivity values for Fe by Ordal *et al*. for the satellite split curved resonators were used [4]. Room temperature natural oxide formation (Fe_2O_3) of a few nanometers on top of Fe curved structures were also considered for accurate calculation [5]. We used refractive index of Ti and Si both from Palik for the central resonator and substrate respectively [6]. The formation of circular magnetic fields in the center of the structure was achieved by exciting localized modes with an input THz beam in negative z axis direction as shown in Fig. 8.2a. The effective electric dipole moment experiences dramatic suppression by the excited strong electric resonance mode supported by the central Ti resonator and the weak magnetic resonance modes in the Fe curved resonators [7, 8]. For the magnetic resonance mode (**m**), it creates strong magnetic fields oscillating circularly in opposite direction at the edge of the Ti block and leads to excite weaker magnetic modes horizontal to the central Ti section as shown in Fig. 8.3a [9]. On the other hand, Fig. 8.3b illustrates the formation of a head-to-tail configuration of the magnetic moments contributing to the desired toroidal dipole (**T**) around the center of the unit cell supported by the torus surface currents (**j**) along the meridian in circular fashion. The arrows specifically highlight the current and magnetic dipole moment direction as in close-loop manner. And due to the designed antisymmetric geometry of the proposed plasmonic metasurface, the required head-to-tail configuration for toroidal dipole mode was observed perpendicular to the central Ti block.
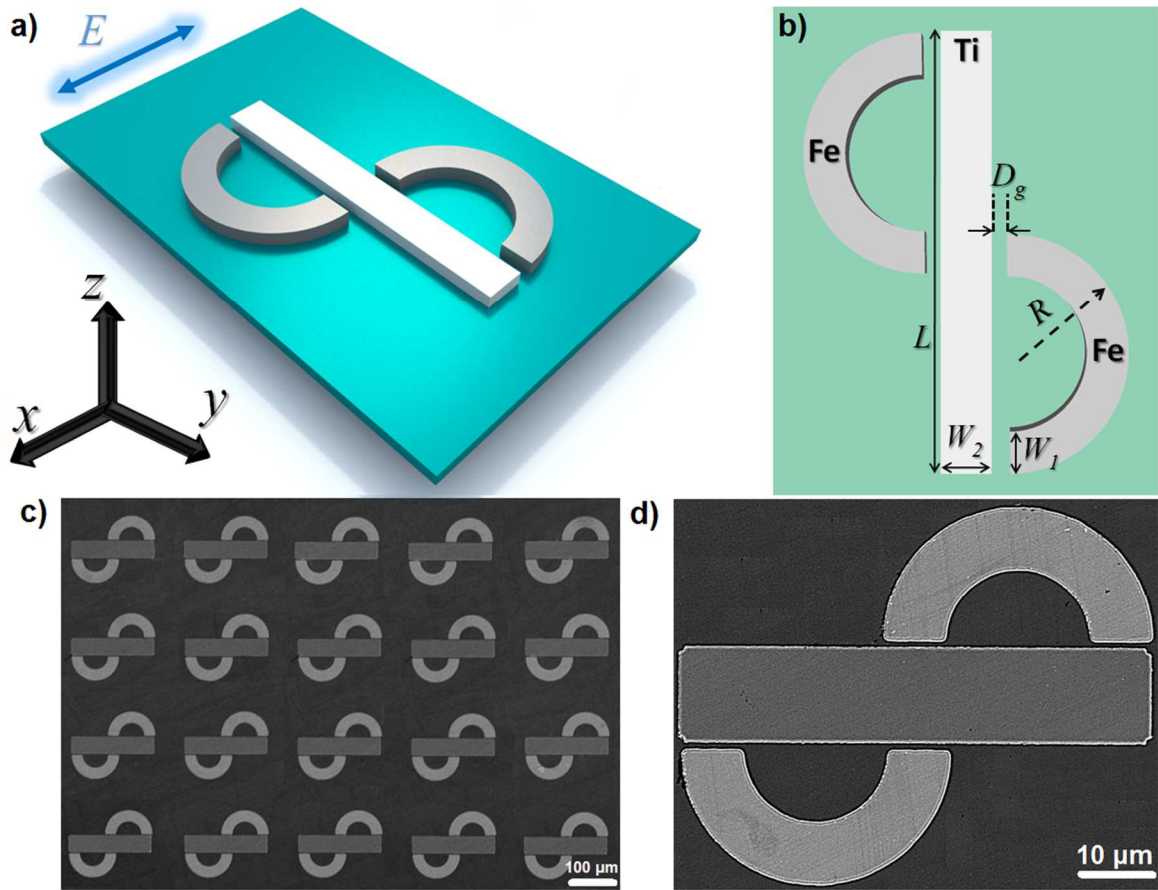
Figure 8.2 | Proposed switch based on THz plasmonic metasurfaces. (a) 3D schematic of the proposed unit cell of plasmonic metasurface. (b) A top-view schematic of the multi-metallic unit cell with detail geometrical description. (c) The SEM image of fabricated proposed plasmonic structures in arrays for the unit cells with the gap spots between surrounding and central resonators of D_g=3 µm with L=240 µm, R=50 µm, W_1=30 µm, and W_2=40 µm. (d) The focused SEM images for each unit cell with D_g=3 µm.

We can calculate the corresponding transmission of the magnetic radiation from the proposed multi-metallic resonators based arrays by taking into account both the scattered magnetic and incident electromagnetic fields. The effective contribution of the far-field scattering of the magnetic field (H_{scat}) can be described as [9, 10],

$$H_{scat} = \frac{k^2}{Z_0 4\pi\varepsilon_0}\Big[\big(\big[(\mathbf{n}\times\mathbf{m_c})\times\mathbf{n}+ik\mathbf{n}\times\mathbf{T_c}\times\mathbf{n}\big]\big)\Big]\times\mathbf{n} \qquad (8.1)$$

where k is the wave vector, Z_0 is the impedance of the medium, ε_0 is the permittivity of the vacuum, $\mathbf{n}$ is a unit vector in the direction of the incident THz beam, and finally, $\mathbf{m_c}$ and $\mathbf{T_c}$ are the magnetic and toroidal dipole moments, respectively, which are defined as [11],

$$\mathbf{m_c} = \frac{1}{2c}\int(\mathbf{r}\times\mathbf{J})d^3\mathbf{r}$$
$$\mathbf{T_c} = \frac{1}{10c}\int\big[(\mathbf{r.J})\mathbf{r}-2r^2\mathbf{J}\big]d^3\mathbf{r} \qquad (8.2)$$

where $\mathbf{J}$ is the induced current density over the entire volume of the area and c is the speed of the light in vacuum. The effect of the offset gaps (D_g) between the Fe curved and Ti central blocks on the electromagnetic response was first analysed to investigate the strong dependence of the magnetic response to the variation of geometrical parameters, as summarized in Figs. 8.3c(i)-8.3e(i). It will help us to understand the controlling mechanism for the position and sharpness of the induced magnetoplasmonic resonances by varying the offset gap. For D_g=3 μm, a sharp magnetic dipole mode minimum is observed at ~0.23 THz (indicated by $\mathbf{m}$ in Fig. 8.3c) in the experimentally measured normalized transmission amplitude profile. On the other hand, toroidal dipole moment ($\mathbf{T}$) minimum with ultrasharp and distinct linewidth was excited at ~0.203 THz as seen in Fig. 8.3c. In this case, the magnetic fields created in the curved Fe resonators and the close-loop magnetic dipole at the offset gap region cumulatively contribute to the formation of the required head-to-tail configuration for the toroidal resonance mode through the classical modes' suppression as reported elsewhere [11-14]. It poses a serious challenge to excite this peculiar and

ultrasharp toroidal resonance mode by employing conventional planar structures. The proposed plasmonic metasurface unit cell enhances the induced toroidal mode due to the introduction of Fe in the curved section with the central Ti block, instead of using Ti all over. The strong electric and weak magnetic responses of the central Ti block help to prevent destructive interference of the strong magnetic moments supported by the curved magnetic resonators and the dipole moments supported by the central resonator. As a result, formation of a closed-loop head-to-tail magnetic moment configuration would be possible around the central part of the unit cell. Furthermore, the presence of the HR Si substrate below the multi-metallic unit cell resonator increases the asymmetry of the entire metasurface. With the increase in the offset gap to 4 μm and 5 μm, we observed linewidth broadening and suppression of the toroidal mode, which dramatically reduced the sharpness of Q -factor of both the magnetic and toroidal resonance modes as seen in Fig. 8.3d(i) and 8.3e(i). Figures 8.3c(ii)-8.3e(ii) summarize the SEM images of the samples with the offset gap variation. Here, we can see that our numerical simulation results (see 8.3c(iii)-8.3e(iii)) are in pretty good agreement with the experimental results, which also validate our simulation methods. We also calculated the corresponding experimental Q-factors as high as $Q_{exp}^{m} = 14$ and $Q_{exp}^{T} = 18$ for the magnetic and toroidal modes, respectively [7, 8, 15, 16].

In order to confirm a resonance mode to be toroidal type, we need to investigate the magnetic field profiles along with surface current distribution. Simulated localized magnetic fields in the plasmonic metasurface as shown in figures 8.4a and 8.4b exhibit the intense magnetic field confinement at the centre of the proposed metasurface for the

toroidal resonance and at the edges in circular fashion for the magnetic resonance mode, respectively. In addition, we used the cross-sectional monitors for the magnetic field (H-field) excitation across the plasmonic metasurface at both toroidal and magnetic resonant moments as illustrated in Figs. 8.4a(iii) and 8.4b(iii), respectively, which provide a better understanding of the formation of head-to-tail circular magnetic fields at the centre of the resonator. The surface current (**j**) was also simulated for both the resonant modes, which are shown in Fig. 8.4c.
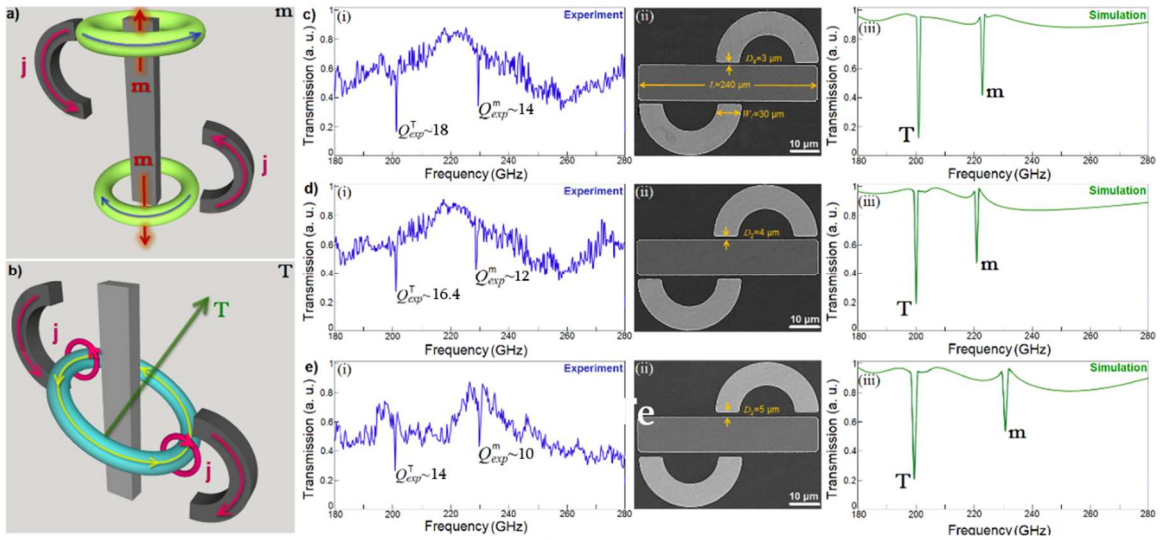
Figure 8.3 | Magnetic and toroidal resonance modes characterization. (a), (b) The 3D schematics of the magnetic (**m**) and toroidal (**T**) resonances, respectively. (c), (d), and (e) The electromagnetic response of the proposed THz plasmonic metasurfaces: (i) Experimentally obtained normalized transmission profiles for the arrays with varying three different offset gaps, (ii) the corresponding SEM images for different offset gaps between resonators, (iii) Numerically simulated transmission spectra for those three different offset gaps.

Next, we investigated the effect of the geometrical variations in the magnetic curved resonators on the excited plasmonic response of the metasurface. To this end, by keeping the width of the central block fixed at $W_2=40$ μm, we changed the widths of the

curved Fe resonators to $W_I=25\,\mu m$ with the radii fixed to $R=50\,\mu m$. Figure 8.5 summarizes both the simulation and experimental results for this geometry settings at three different offset gaps. With the reducing width of the Fe components, strength of the magnetic dipole moment (**m**) decays dramatically as expected and does not radiate as strongly as it did in the previous cases with larger width. Therefore, a significant decay in toroidal mode was observed due to slightly dominant behaviour of the excited classical electric dipolar and multipolar moments.
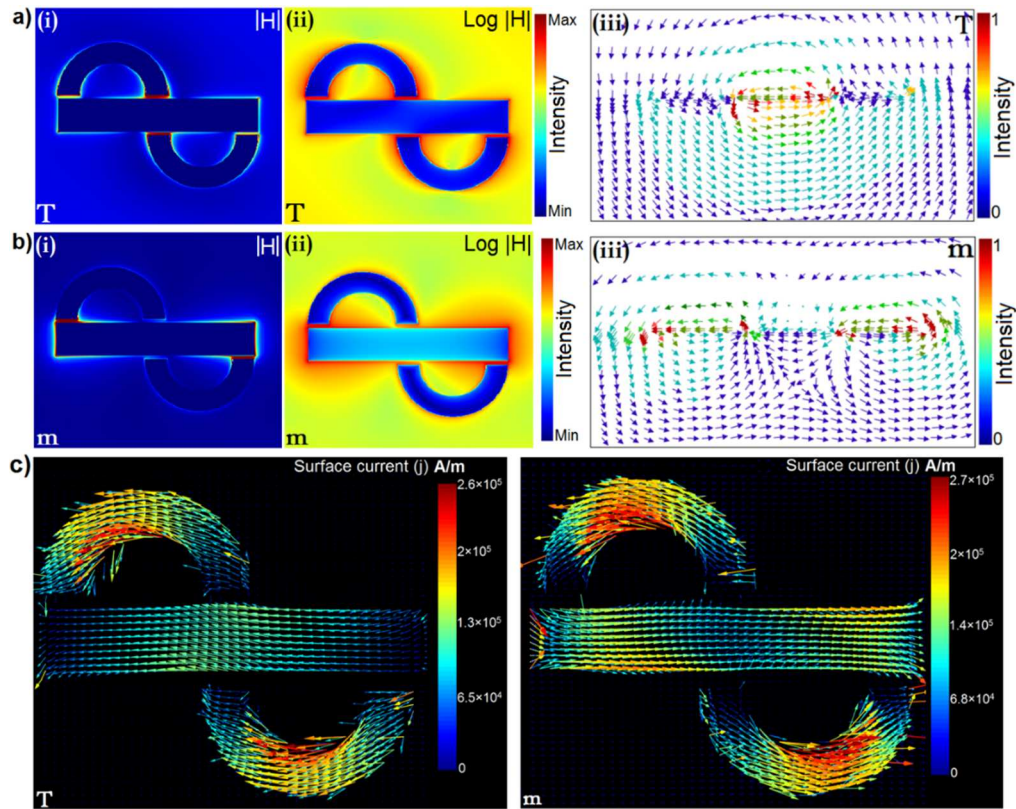
Figure 8.4 | Numerical cross-examination for magnetic and toroidal resonances. The electromagnetic field of the proposed structure at (a) toroidal and (b) magnetic resonance modes. Simulated local |H|-field (A/m) for the toroidal and magnetic resonance modes highlighting the confinement and excitation regions in (i) linear and (ii) logarithmic scales. (iii) The cross-sectional vectorial maps for the magnetic field lines for those same resonant modes. (c) Numerically calculated surface currents (j) of the proposed plasmonic structure at resonant modes.
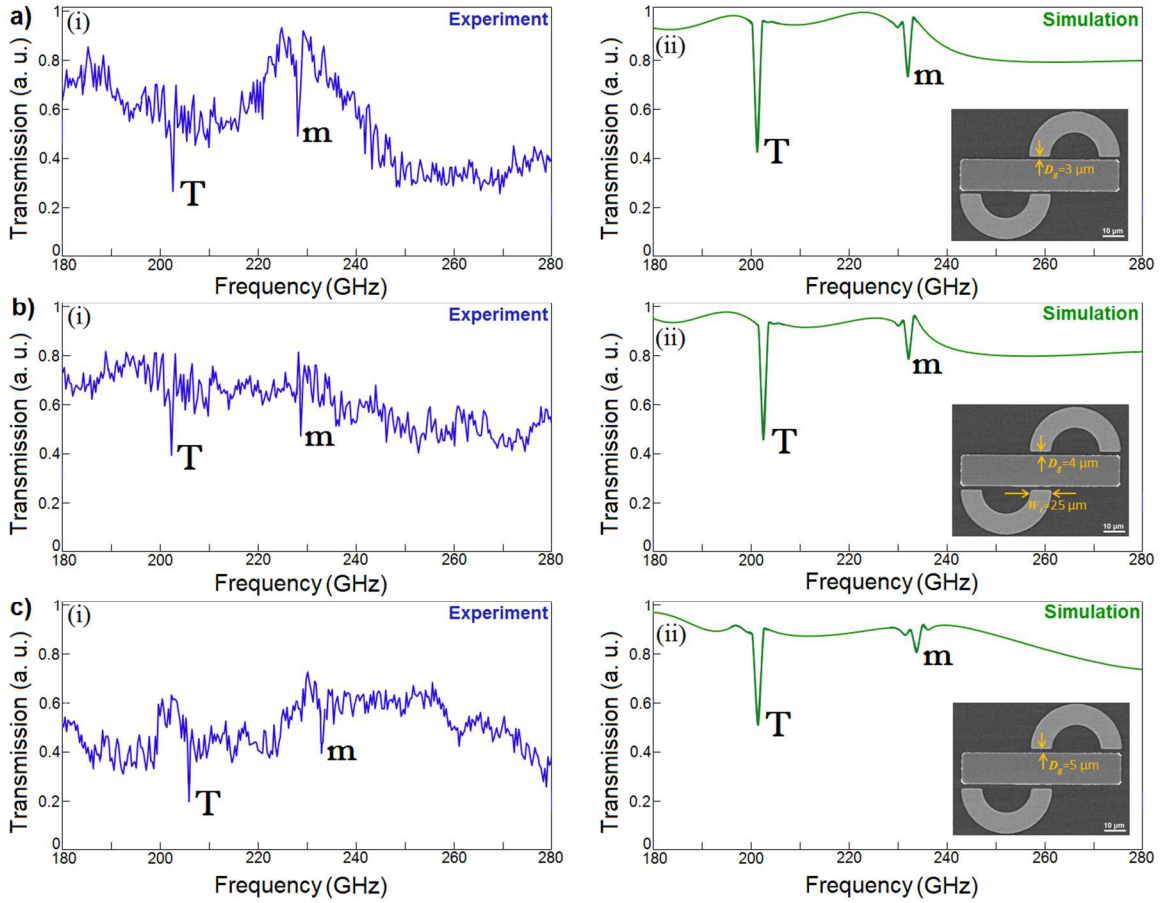
Figure 8.5 | Effect of gap size in toroidal and magnetic resonances in the proposed plasmonic metasurfaces. Normalized transmission profiles of the THz plasmonic system with three different offset gaps obtained (i) experimentally and (ii) numerically for (a) D_g=3 µm, (b) D_g=4 µm, and (c) D_g=5 µm. The insets are the SEM images with the geometrical dimensions.

It should be noted that despite of achieving prevailing response, both electric and magnetic multipolar moments are not still resonant in this frequency due to poor scattering efficiency [17, 18]. After comparing Fig. 8.5a and Fig. 8.3a, the dramatic decay in the corresponding Q-factor of the toroidal mode is obvious. In the same way, the magnetic dipole moment also decays significantly due to the dominant electric and magnetic classical multipolar modes. In this limit, increasing the offset gap distance between the

central and curved resonators gives rise to continuing decay in the Q-factor of both the induced modes (see Figs. 8.5b and 8.5c). For D_g=5 µm, the magnetic dipolar moment is almost disappeared and difficult to identify in the experimental transmission. Also, the minor blue-shift in the positions of both resonant dips is caused by the geometrical dimension variations, which can easily be described by Mie scattering theory [14].

It should be noted that the exquisite properties of the proposed THz plasmonic metasurface is not limited to sustaining ultra-sharp toroidal response. The unique geometry of the multi-metallic resonators allows for highly sensitive polarization dependency to the angle of the incident beam. This feature allows for use of the proposed structure as a THz switch. Using the inherent and exotic anti-symmetry of the plasmonic unit cell, an efficient polarization-dependent plasmonic toroid switch can be realized. By choosing the best response from the previously studied structures with the highest Q-factor, we analyse the behaviour of a sample unit cell under incident THz beam polarization variations. Figure 8.6a shows an artistic schematic of the metasurface and the angle (φ) and direction of the incident magnetic field (H). In Fig 8.6b, we plotted the experimentally measured normalized transmission spectra for a unit cell with the following geometrical parameters: D_g=3 µm, with L=240 µm, R=50 µm, W_1=30 µm, and W_2=40 µm, to achieve the highest possible Q-factor. In principle, for the incident magnetic beam in the longitudinal polarization limit (φ=90°) parallel to the central block (H∥), the same toroidal dipolar dip is induced with high-Q around 0.2 THz and the beam transmissivity is extremely low. Rotating the angle of the polarization to φ=45°, we observed a drastic decay in the toroidal resonant mode dip. Eventually, for φ=0°, where the incident magnetic component entirely

transverse (H⊥) to the central block, the toroidal dip is eliminated and the plasmonic metasurface acts as a transparent media at this frequency. As a result, the toroidal resonance characteristics disappeared. To understand the physics behind the disappearance of the toroidal mode, we should note the direction of the incident electric field component (E∥) as well. For $\varphi=0°$, due to the antisymmetric geometry of the plasmonic unit cell, the incident electric field component becomes parallel (E∥) to the central block and offset gaps. In this regime, the electric field becomes dominant and the required head-to-tail magnetic moment closed-loop cannot be formed around the central block of the micro-structure. Interestingly, however, a distinct magnetic dipolar moment around ~0.23 THz remains due to excitation of the dipolar magnetic resonances by the magnetic peripheral curves *via* transverse incident magnetic beam. One should note that the *Q*-factor of the induced magnetic dipolar moment in this regime is poorer than the ones in the previous regimes. Moreover, the transmission spectra (for the toroidal response) as a function of the magnetic component of the incident beam angle (φ) is plotted in Fig. 8.6c. Such a strong dependence of toroidal minimum can be exploited for fast and efficient on/off routing [19-25] and filtering purposes [26, 27]. As a key parameter, we also computed the corresponding modulation-depth (MD) for the proposed metasurface as a function of microstructure's geometries, as shown in Fig. 8.6d. Here, the best MD was determined as ~96% for a resonator with the gap size of 3 μm and curved resonator width of 30 μm. The plotted diagram shows the strong dependency of the toroidal dipolar mode and subsequently MD on both geometrical and polarization. Ultimately, to verify this claim, we plotted the transmission spectra vs polarization angle in polar plane for the analysed unit cell in Fig.

8.6e. The obtained experimental and numerical data confirms the strong dependency of the transmission characteristics of the beam, especially to its angle of polarization direction.
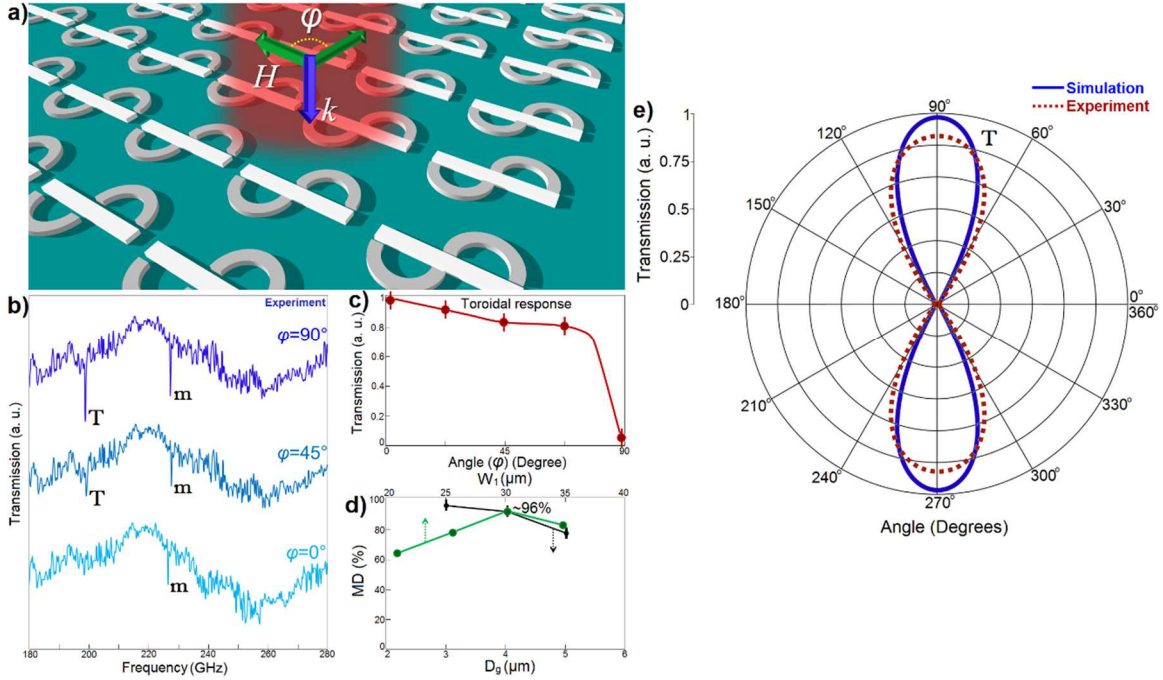
Figure 8.6 | Experimental results for the proposed THz switch. (a) A perspective schematic for a metasurface consisting of arrays of compositional plasmonic metasurface unit cells. (b) Experimentally measured normalized transmission amplitude for both toroidal and magnetic responses of the plasmonic unit cell under different magnetic polarization angles $0° \leq \varphi \leq 90°$. (c) Toroidal response of the unit cell as a function of incident beam's component angle. (d) The MD percentage as a function of both W_1 and D_g, showing the highest value around ~96%. (e) The polar plot for both experimentally and numerically obtained transmission spectra for the toroidal resonant mode.

8.2   References

1. Savinov, V., Fedotov, V. A., & Zheludev, N. I. (2014). Toroidal dipolar excitation and macroscopic electromagnetic properties of metamaterials. Physical Review B, 89(20), 205112.

2. Sinha, R., Karabiyik, M., Al-Amin, C., Vabbina, P.K., Güney, D.Ö. and Pala, N. (2015). Tunable room temperature THz sources based on nonlinear mixing in a hybrid optical and THz micro-ring resonator. Scientific reports, 5.

3. Sinha, R., Karabiyik, M., Ahmadivand, A., Al-Amin, C., Vabbina, P.K., Shur, M. and Pala, N. (2016). Tunable, Room Temperature CMOS-Compatible THz Emitters Based on Nonlinear Mixing in Microdisk Resonators. Journal of Infrared, Millimeter, and Terahertz Waves, 37(3), pp.230-242.

4. Ordal, M. A., Bell, R. J., Alexander, R. W., Newquist, L. A., & Querry, M. R. (1988). Optical properties of Al, Fe, Ti, Ta, W, and Mo at submillimeter wavelengths. Applied optics, 27(6), 1203-1209.

5. Ordal, M. A., Bell, R. J., Alexander, R. W., Newquist, L. A., & Querry, M. R. (1988). Optical properties of Al, Fe, Ti, Ta, W, and Mo at submillimeter wavelengths. Applied optics, 27(6), 1203-1209.

6. Palik, E. D. (Ed.). (1997). Handbook of Optical Constants of Solids, Five-Volume Set: Handbook of Thermo-Optic Coefficients of Optical Materials with Applications. Academic Press.

7. Gupta, M., Savinov, V., Xu, N., Cong, L., Dayal, G., Wang, S., Zhang, W., Zheludev, N.I., & Singh, R. (2016). Sharp Toroidal Resonances in Planar Terahertz Metasurfaces. Advanced Materials, 28(37), 8206-8211.

8. Gupta, M., & Singh, R. (2016). Toroidal versus Fano Resonances in High Q planar THz Metamaterials. Advanced Optical Materials, 4(12), 2119-2125.

9. Wang, J., Fan, C., He, J., Ding, P., Liang, E., & Xue, Q. (2013). Double Fano resonances due to interplay of electric and magnetic plasmon modes in planar plasmonic structure with high sensing sensitivity. Optics express, 21(2), 2236-2244.

10. Jackson, J. D., & Fox, R. F. (1999). Classical electrodynamics. American Journal of Physics, 67(9), 841-842.

11. Papasimakis, N., Fedotov, V. A., Savinov, V., Raybould, T. A., & Zheludev, N. I. (2016). Electromagnetic toroidal excitations in matter and free space. Nature materials, 15(3), 263-271.

12. Kaelberer, T., Fedotov, V. A., Papasimakis, N., Tsai, D. P., & Zheludev, N. I. (2010). Toroidal dipolar response in a metamaterial. Science, 330(6010), 1510-1512.

13. Afanasiev, G. N., & Dubovik, V. M. (1992). Electromagnetic properties of a toroidal solenoid. Journal of Physics A: Mathematical and General, 25(18), 4869.

14. Newton, R. G. (1982). Scattering theory of waves and particles Springer-Verlag. New York.

15. Zhu, W. M., Liu, A. Q., Zhang, X. M., Tsai, D. P., Bourouina, T., Teng, J. H., Zhang, X.H., Guo, H.C., Tanoto, H., Mei, T., & Lo, G. Q. (2011). Switchable magnetic

metamaterials using micromachining processes. Advanced Materials, 23(15), 1792-1796.

16. Meng, F. Y., Wu, Q., Erni, D., Wu, K., & Lee, J. C. (2012). Polarization-independent metamaterial analog of electromagnetically induced transparency for a refractive-index-based sensor. IEEE transactions on microwave theory and techniques, 60(10), 3013-3022.

17. Zayats, A. V., & Maier, S. (Eds.). (2013). Active plasmonics and tuneable plasmonic metamaterials (Vol. 8). John Wiley & Sons.

18. Lindquist, N. C., Nagpal, P., McPeak, K. M., Norris, D. J., & Oh, S. H. (2012). Engineering metallic nanostructures for plasmonics and nanophotonics. Reports on Progress in Physics, 75(3), 036501.

19. Zijlstra, P., Paulo, P. M., & Orrit, M. (2012). Optical detection of single non-absorbing molecules using the surface plasmon resonance of a gold nanorod. Nature nanotechnology, 7(6), 379-382.

20. Anker, J. N., Hall, W. P., Lyandres, O., Shah, N. C., Zhao, J., & Van Duyne, R. P. (2008). Biosensing with plasmonic nanosensors. Nature materials, 7(6), 442-453.

21. Dondapati, S. K., Sau, T. K., Hrelescu, C., Klar, T. A., Stefani, F. D., & Feldmann, J. (2010). Label-free biosensing based on single gold nanostars as plasmonic transducers. Acs Nano, 4(11), 6318-6322.

22. Wang, N., Hashemi, M. R., & Jarrahi, M. (2013). Plasmonic photoconductive detectors for enhanced terahertz detection sensitivity. Optics express, 21(14), 17221-17227.

23. Menikh, A., MacColl, R., Mannella, C. A., & Zhang, X. C. (2002). Terahertz biosensing technology: Frontiers and progress. ChemPhysChem, 3(8), 655-658.

24. Park, S. J., Hong, J. T., Choi, S. J., Kim, H. S., Park, W. K., Han, S. T., ... & Ahn, Y. H. (2014). Detection of microorganisms using terahertz metamaterials. Scientific reports, 4, 4988.

25. Fan, Y., Wei, Z., Li, H., Chen, H., & Soukoulis, C. M. (2013). Low-loss and high-Q planar metamaterial with toroidal moment. Physical Review B, 87(11), 115417.

26. Zhang, H., Guo, P., Chen, P., Chang, S., & Yuan, J. (2009). Liquid-crystal-filled photonic crystal for terahertz switch and filter. JOSA B, 26(1), 101-106.

27. Zhang, X., Tan, R., Zheng, Z., Li, X., Zhang, Z., Sun, J., ... & Qin, H. (2013). Terahertz filters based on frequency selective surfaces for high-speed terahertz switch. Journal of Applied Physics, 113(1), 014504.

CHAPTER 9

Conclusions and Future Direction

9.1 **Conclusions**

In this dissertation, we have presented novel approaches to achieve enhanced difference

frequency generation (DFG) across the whole spectral range (0.5-10 THz) of THz

radiation. Each of the proposed THz emitters has the advantages of wide range tunability,

compactness, room temperature operation, fast modulation and the possibility for

monolithic integration, which are the most sought after properties in the new generation

THz sources. First, we investigated THz radiation in a hybrid optical and THz micro-ring

resonators system. For the first time, we were able to satisfy the DFG phase matching

condition for the above-mentioned THz range in one single device geometry by employing

a modal phase matching technique and using two separately designed resonators capable

of oscillating at input optical waves of shorter wavelengths and generated THz waves of

longer wavelengths. In comparison to microring resonators, microdisk resonators with the

same dimensions are expected to provide higher quality factors with smaller radiation

losses due to the absence of inner cylindrical boundaries. Therefore, we investigated

another potential THz emitter by using microdisk resonators. Due to the fact that micro-

ring or micro-disk resonators are resonated at certain frequencies over a frequency range

of interest, the difference between the two consecutive resonant frequencies, namely free

spectral range imposes a limiting factor of minimum tunability resolution in the designed

THz emitters, which demanded further research to design THz emitters with continuously

tunability across the THz range of interest.

Further, we explored numerous coupled plasmonic nanostructures to create extremely large localized fields with plasmonic resonance mode, because it is possible to enhance inherently weak DFG process by employing the highly intensified input fields. Here, we proposed a novel antenna geometry – the dimer rod-tapered antenna (DRTA), where we created a hot-spot in the nanogap between the dimer arms with a huge intensity enhancement of 4.1×10^5 at resonant frequency. Then, we investigated DFG operation in the antenna geometry by incorporating a nonlinear nanodot in the hot-spot of the antenna and achieved continuously tunable enhanced THz radiation across 0.5-10 THz range. We have also proposed and investigated in detail spherical core-shell plasmonic nanostructures for continuously tunable DFG THz radiation in the same range. Finally, we investigated and designed another THz emitter by coupling aluminum grating resonators to a thin film of nonlinear layer.

In addition, we designed a multi-metallic resonators providing an ultrasharp toroidal response at THz frequency, then fabricated and experimentally demonstrated an efficient polarization dependent plasmonic toroid switch operating at THz frequency.

9.2   Future Direction

Seeing the strong need for advanced THz devices to bring THz technology into life, we will continue pursuing research opportunities to investigate the tunable THz sources and to integrate them with compact THz detectors to create on-chip THz spectrometer systems.

9.2.1 Demonstrating Biosensing Capabilities by Integrating Microfluidic Channel with the Proposed THz Emitters

Ultra-compact, label-free, non-invasive, safe, fast detection technique with high sensitivity and selectivity, simplicity of sample preparation steps are the most demanding features in any kind of sensing devices. THz absorption spectroscopy has emerged as a successful method to noninvasively identify minute amounts of biomolecules or biochemical substances [1-3]. Certain volatile organic compounds also exhibit absorption signatures in THz region, which makes them potential candidates as biomarkers for certain diseases in THz absorption spectroscopy [4]. Acetaldehyde is considered tracer for lung cancer, alcoholism and liver related diseases; isopropyl alcohol is a tracer for lung cancer; acetone is a tracer for dietary fat losses, congestive heart failures, diabetes and lung cancer; methanol is a biomarker for nervous system disorder; and ethanol is a tracer for the production of gut bacteria [5-7]. Again, it has been reported that polyomavirus capsid and virus-like particles show dramatically different and distinctive absorption spectrum compared to capsomeres in THz range [8]. Hence, it demands for further investigation into the potential possibility of finding THz spectral signatures of other viruses with the use of THz spectroscopy. Here, we propose to develop an ultra-compact lab-on-a-chip THz spectrometer by integrating our proposed THz emitters with microfluidic channel and CMOS compatible THz detector, where microfluidic channel will be employed as an absorption cell for different biomolecules, biochemical substances, volatile organic compounds and viruses or virus-like structures.
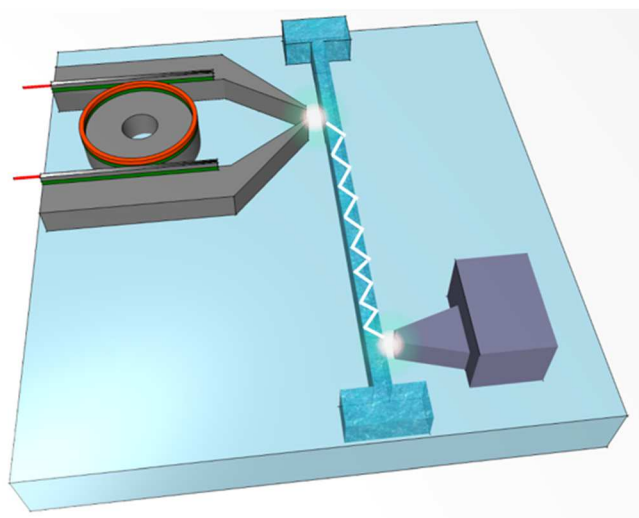
Figure 9.1 | Proposed ultra-compact Lab-on-a-chip THz spectrometer. The proposed THz emitters can be monolithically integrated to THz detector coupled with a microfluidic channel for point-of-care testing.

9.3   References

1. Menikh, A., MacColl, R., Mannella, C. A., & Zhang, X. C. (2002). Terahertz biosensing technology: Frontiers and progress. ChemPhysChem, 3(8), 655-658.

2. Bolivar, P. H., Brucherseifer, M., Nagel, M., Kurz, H., Bosserhoff, A., & Büttner, R. (2002). Label-free probing of genes by time-domain terahertz sensing. Physics in Medicine and Biology, 47(21), 3815.

3. Lu, J. Y., Chen, L. J., Kao, T. F., Chang, H. H., Chen, H. W., Liu, A. S., Chyi, J.I., & Sun, C. K. (2006). Terahertz microchip for illicit drug detection. IEEE photonics technology letters, 18(21), 2254-2256.

4. Neumaier, P. X., Schmalz, K., Borngräber, J., Wylde, R., & Hübers, H. W. (2015). Terahertz gas-phase spectroscopy: chemometrics for security and medical applications. Analyst, 140(1), 213-222.

5. Wang, C., & Sahay, P. (2009). Breath analysis using laser spectroscopic techniques: breath biomarkers, spectral fingerprints, and detection limits. Sensors, 9(10), 8230-8262.

6. Konvalina, G., & Haick, H. (2013). Sensors for breath testing: from nanomaterials to comprehensive disease detection. Accounts of chemical research, 47(1), 66-76.

7. Hakim, M., Broza, Y. Y., Barash, O., Peled, N., Phillips, M., Amann, A., & Haick, H. (2012). Volatile organic compounds of lung cancer and possible biochemical pathways. Chemical reviews, 112(11), 5949-5966.

8. Falconer, R. J., & Markelz, A. G. (2012). Terahertz spectroscopic analysis of peptides and proteins. Journal of Infrared, Millimeter, and Terahertz Waves, 33(10), 973-988.

VITA

RAJU SINHA

2004 - 2009	B. Sc., Electrical and Electronic Engineering Bangladesh University of Engineering and Technology Dhaka, Bangladesh
2009 - 2012	M. Sc., Electrical and Electronic Engineering Bangladesh University of Engineering and Technology Dhaka, Bangladesh
2012 - 2017	Doctoral Candidate (PhD) Florida International University Miami, Florida, USA

PUBLICATIONS AND PRESENTATIONS

1. Sinha, R., Karabiyik, M., Al-Amin, C., Vabbina, P. K., Güney, D. Ö., & Pala, N. (2015). Tunable Room Temperature THz Sources Based on Nonlinear Mixing in a Hybrid Optical and THz Micro-Ring Resonator. Scientific Reports, 5, 9422.

2. Sinha, R., Karabiyik, M., Ahmadivand, A., Al-Amin, C., Vabbina, P. K., Shur, M., & Pala, N. (2016). Tunable, Room Temperature CMOS-Compatible THz Emitters Based on Nonlinear Mixing in Microdisk Resonators. Journal of Infrared, Millimeter, and Terahertz Waves, 37(3), 230-242.

3. Kaushik, A., N.-Moshaie, R., Sinha, R., Bhardwaj, V., Atluri, V., Jayant, R. D., Yndart, A., Kateb, B., Pala, N., & Nair, M. (2017). Investigation of ac-magnetic Field Stimulated Nanoelectroporation of Magneto-electric Nano-drug-carrier inside CNS Cells," Scientific Reports 7, 45663.

4. Ahmadivand, A., Gerislioglu, B., Sinha, R., Karabiyik, M., & Pala, N. (2017). Optical Switching Using Transition from Dipolar to Charge Transfer Plasmon Modes in $Ge_2Sb_2Te_5$ Bridged Metallodielectric Dimers. Scientific Reports, 7, 42807.

5. Ahmadivand, A., Sinha, R., & Pala, N. (2017). Magnetic fano resonances in all-dielectric nanocomplexes under cylindrical vector beams excitation. Optics & Laser Technology, 90, 65-70.

6. Ahmadivand, A., Sinha, R., Karabiyik, M., Vabbina, P. K., Gerislioglu, B., Kaya, S., & Pala, N. (2017). Tunable THz wave absorption by graphene-assisted plasmonic metasurfaces based on metallic split ring resonators. Journal of Nanoparticle Research, 19(1), 3.

7. Ahmadivand, A., Sinha, R., Gerislioglu, B., Karabiyik, M., Pala, N., & Shur, M. (2016). Transition from capacitive coupling to direct charge transfer in asymmetric terahertz plasmonic assemblies. Optics Letters, 41(22), 5333-5336.

8. Ahmadivand, A., Sinha, R., Vabbina, P. K., Karabiyik, M., Kaya, S., & Pala, N. (2016). Hot electron generation by aluminum oligomers in plasmonic ultraviolet photodetectors. Optics express, 24(12), 13665-13678.

9. Ahmadivand, A., Sinha, R., & Pala, N. (2016). Resonance coupling in plasmonic nanomatryoshka homo-and heterodimers. AIP Advances, 6(6), 065102.

10. Karabiyik, M., Ahmadivand, A., Sinha, R., Al-Amin, C., Vabbina, P. K., Kaya, S., Rupper, G., Rudin, S., Shur, M. & Pala, N. (2016). Plasmonic properties of asymmetric dual grating gate plasmonic crystals. Physica Status Solidi (B), 253(4), 671-675.

11. Ahmadivand, A., Sinha, R., Kaya, S., & Pala, N. (2016). Rhodium plasmonics for deep-ultraviolet bio-chemical sensing. Plasmonics, 11(3), 839-849.

12. Ahmadivand, A., Sinha, R., Kaya, S., & Pala, N. (2016). A molecular plasmonic Fano-router: Using hotspots in a single-stone ring-like structure. Optics Communications, 367, 123-129.

13. Ahmadivand, A., Sinha, R., & Pala, N. (2015). Hybridized plasmon resonant modes in molecular metallodielectric quad-triangles nanoantenna. Optics Communications, *355*, 103-108.

14. Vabbina, P., Choudhary, N., Chowdhury, A.A., Sinha, R., Karabiyik, M., Das, S., Choi, W. and Pala, N. (2015). Highly sensitive wide bandwidth photodetector based on internal photoemission in CVD grown p-type MoS2/graphene Schottky junction. ACS applied materials & interfaces, 7(28), 15206-15213.

15. Sinha, R., Vabbina, P. K., Ahmadivand, A., Karabiyik, M., Gerislioglu, B., and Pala, N. (October, 2016). Ultraviolet LED based Compact and Fast Cortisol Detector with Ultra High Sensitivity. Proceedings of IEEE SENSORS, Orlando, FL, USA.

16. Sinha, R., Karabiyik, M., Al-Amin, C., Vabbina, P. K. and Pala, N. (2014). Nonlinear optical resonators for tunable THz emission. Proceedings of SPIE Vol. 8985, 898505.

17. Sinha, R., Karabiyik, M., Al-Amin, C., Vabbina, P. K., Shur, M., and Pala, N. (2014). Microdisk resonators for difference frequency generation in THz range. Proceedings of SPIE Vol. 9102, 910208.

18. Ahmadivand, A., Sinha, R., and Pala, N. (2015). Graphene plasmonics: multiple sharp Fano resonances in silver split concentric nanoring/disk resonator dimers on a metasurface. Proceedings of SPIE Vol. 9547, 954713.

19. Karabiyik, M., Sinha, R., Al-Amin, C., and Pala, N. (2014). Dispersion studies in THz plasmonic devices with cavities. Proceedings of SPIE Vol. 9102, 91020K.